IntechOpen

Small Angle Scattering and Diffraction

Edited by Margareth K. K. D. Franco and Fabiano Yokaichiya

SMALL ANGLE SCATTERING AND DIFFRACTION

Edited by **Margareth K. K. D. Franco**
and **Fabiano Yokaichiya**

Small Angle Scattering and Diffraction
http://dx.doi.org/10.5772/intechopen.71473
Edited by Margareth K. K. D. Franco and Fabiano Yokaichiya

Contributors

Greeshma Gadikota, Eugen Anitas, Azat Mukhiddinuly Slyamov, Cristiano Luis Pinto Oliveira, Cassio Alves, Baobao Chang, Konrad Schneider, Patil Nilesh, Gert Heinrich, Ines Kuehnert, Oskar Beer

Notice

Statements and opinions expressed in the chapters are these of the individual contributors and not necessarily those of the editors or publisher. No responsibility is accepted for the accuracy of information contained in the published chapters. The publisher assumes no responsibility for any damage or injury to persons or property arising out of the use of any materials, instructions, methods or ideas contained in the book.

First published in London, United Kingdom, 2018 by IntechOpen
eBook (PDF) Published by IntechOpen, 2019
IntechOpen is the global imprint of INTECHOPEN LIMITED, registered in England and Wales, registration number: 11086078, The Shard, 25th floor, 32 London Bridge Street
London, SE19SG – United Kingdom
Printed in Croatia

British Library Cataloguing-in-Publication Data
A catalogue record for this book is available from the British Library

Additional hard and PDF copies can be obtained from orders@intechopen.com

Small Angle Scattering and Diffraction
Edited by Margareth K. K. D. Franco and Fabiano Yokaichiya

p. cm.

Print ISBN 978-1-78923-246-2

Online ISBN 978-1-78923-247-9

eBook (PDF) ISBN 978-1-83881-581-3

Meet the editors

A researcher at the Nuclear and Energy Research Institute, Department of Radioactive Rejects in Brazil, Margareth K.K.D. Franco received her BSc degree in Chemical Engineering from São Paulo University (USP) in 1982; MSc degree in Chemical Engineering from the University of Campinas, commonly called Unicamp, in 1987; and PhD degree in Electrical Engineering from the University of Campinas, using the thesis entitled "Deposition and characterization of semiconductor diamond films," in 1996. Specialization in Scientific Journalism in 2005. She published papers in local and international peer-reviewed journals in the fields of materials, biochemistry, pharmacology, x-ray diffraction, and small-angle scattering. She has worked for the Brazilian Synchrotron Light Laboratory, x-ray powder diffraction beamline, dedicated to meeting the needs of researchers from several countries, providing technical and scientific support. She sustains collaborations with researchers from Germany and Australia to study green cement, composites with cement, and irradiated cement. Researches with drug delivery systems focus on characterization through small-angle x-ray scattering and small-angle neutron scattering.

Researcher and instrument scientist for two-axis diffractometer (E4) and for flat-cone diffractometer (E2) at Helmholtz-Zentrum Berlin für Materialien und Energie (HZB), Germany, Dr. Fabiano Yokaichiya graduated as an electronic engineer at the Federal University of Parana (UFPR), Brazil, in 1995, and obtained his PhD degree in Physics where he studied strong correlated systems using synchrotron radiation facilities at the University of Campinas (Unicamp), Brazil, in 2003. From 2005 to 2010, he worked as a postdoctoral researcher in several laboratories like Laboratoire Louis Néel in Grenoble, France (2005); Brookhaven National Laboratory, USA (2006); and Helmholtz-Zentrum Berlin, Germany (2007–2010). From 2010 to 2013, he worked at LNLS as a beamline scientist responsible for the x-ray powder diffraction (XPD) beamline. Nowadays, his main projects are concerned with magnetic materials, drug delivery systems, and cement/concrete systems.

Contents

Preface

Technological development and innovation development are increasing challenges that involve well-planned public policies in partnership with the private industrial sector. Enabling this development implies stimulating the concomitant development of increasingly sophisticated characterization techniques. This is particularly noteworthy with regard to the use of sources such as x-rays and neutrons in characterization techniques. The use of these techniques has become more frequent due to its potentiality and particularities. It is possibly observed that industries apply more and more efficient characterization techniques that allow them not only to improve the quality of their products but also to predict their durability.

The large number of characterization techniques available is intriguing, but we observe that many publications using tools such as diffraction and small-angle scattering using x-ray and neutron as a probe of investigation do not exploit these techniques to their fullest extent. It is important to emphasize that the recent advances in scattering techniques allow to map the structure and the microstructure of architected and natural materials in spatial scale. The techniques that use the scattering setup can successfully be applied in the fields of basic knowledge like physics, biology, and chemistry, as well as in technological applications such as medicine, pharmacology, and the aeronautic industry.

Emphasizing practical applications and real-world case studies, this book presents the principles of widely used, advanced surface and structural characterization techniques for quality assurance, contamination control, and process improvement.

This book covers the following:

- It explores scientific processes to characterize materials using SAXS and diffraction.
- It presents performance analysis of some materials under specific conditions of use.
- The interdependence between processing, structure, properties, and performance is presented to illustrate the wealth of information.
- It presents the fundamentals of x-ray diffraction principles as well as small-angle x-ray scattering.

The authors of the subsequent chapters chose to omit long derivations and formulations, exposing only the appropriate uses and technical requirements related to characterization techniques. In fact, they emphasize useful basic principles and modern technology applications used to characterize engineering materials, helping readers understand the micro- and nanoscale properties. This book will serve as a valuable reference for researchers and engineers involved in characterization and also as an introduction to the field for advanced undergraduate and graduate students.

Although the subject of x-ray scattering is extremely wide, we synthesized the book into five chapters that outline the application of SAXS and diffraction techniques.

In Chapter 1, "Calculation of Small-Angle Scattering Patterns," the authors present an overview of current available simulation/modeling methods for small-angle scattering (SAS) for systems composed of oriented or for random-oriented particles. The use of the finite element method as well as a newly developed method for calculating scattering intensity for oriented particles is presented as illustrative example. We highlight that the authors show that small-angle scattering (SAS) experiments can be applied to nano-scaled systems, allowing the investigation of the constituent's overall shape, size, internal structure, and arrangement.

In Chapter 2, "X-Ray Diffraction Analysis of Structural Changes Induced by Overrolling," the aim is to propose a new method of x-ray diffraction analysis to evaluate structural changes in rolling element-bearing components. Applied to the basics of residual stress measurement by x-ray diffraction, the authors aim to perform microstructural analysis on bearing components after rig testing and after use in the field, focusing on the aeroengine industry. The results shown in this chapter are mostly derived from rolling element-bearing applications in aeroengines. The authors show how an estimation of a rolling contact fatigue life can be derived from microstructural analysis besides showing that near-surface-induced residual stresses can improve rolling contact fatigue life. Nevertheless, they also demonstrated that the basic results from rig testing can be transferred to use in the field.

In Chapter 3, "Cavitation Behavior of Semicrystalline Polymers during Uniaxial Stretching Studied by Synchrotron Small-Angle X-Ray Scattering," the authors show that small-angle x-ray scattering (SAXS) can be used as a powerful method to in situ monitor the evolution of voids with high time and spatial resolution. Recent reports about the cavitation behavior of semicrystalline polymers studied by SAXS are also reviewed in this chapter. In addition to presenting an introduction to theoretical background related to the SAXS technique, they show some exemplary results about the cavitation behavior of microinjection-molded isotactic polypropylene, studied by synchrotron SAXS measurements.

Hazardous waste, for which there is no definitive disposal solution, is generated in diverse activities such as fundamental and applied research, medicine, industry, energy, etc. Burned fuels from nuclear research reactors, sealed radioactive sources used in cancer treatment and discarded at the end of their useful life, and lees and incrustation containing natural radiative substances extracted from oil platforms are other examples of waste that need to be properly treated. One of the greatest challenges facing our generation is the sustainable storage of environmental waste. The immobilization of these wastes is necessary to comply with the regulations of the nuclear area and to comply with the acceptance criteria for rejects in repositories, which require that the wastes are in solid form in a durable and resistant monolithic matrix. Convinced to ensure the environmentally benign storage of these by-products in a solid form, it is essential to understand the chemical and morphological features of the materials in which these by-products are immobilized.

In Chapter 4, "Multiscale X-Ray Scattering for Probing Chemomorphological Coupling in Pore-to-Field and Process Scale Energy and Environmental Applications," the authors show the chemical and morphological features of the materials in which these by-products are immobilized. The authors show application of the x-ray scattering techniques to investigate systems able to store harmful wastes like nuclear elements and CO2, in order to protect the

environment. The authors use two examples to discuss about multiscale x-ray scattering, which encompasses ultrasmall-, small-, and wide-angle x-ray scattering (USAXS/SAXS/WAXS). The first example involves determination of the changes in the porosity and the structure of beidellite, and the second example illustrates the changes in the nanoscale porosity of heat-treated serpentine after reacting with CO2 to form magnesium carbonate.

In Chapter 5, "Small-Angle Scattering Analysis of Fractals Generated by Additive Cellular Automata," structural analysis of fractals generated using one-dimensional additive cellular automata (ACA) is presented. The authors view additive cellular automata as discrete dynamical system, in which the set of possible configurations of ACA forms a fractal set. The aim of this study is to show how the scattering data from ACA can provide information about the overall size of the system, the number of total units, the number of rows, the size of the basic fractal units, the scaling factor, and the fractal dimension. They provide some useful relations between structural parameters of ACA that can be obtained experimentally from small-angle scattering (SAS). This chapter will show how to extract structural information and fractal properties of ACA from SAS data.

In light of this, the purpose of this book is to show the great applicability of scattering characterization techniques. The topics covered are current and of interest to the entire scientific community. We believe that this work will contribute to all those who need to characterize their materials.

Margareth K.K.D. Franco
Nuclear and Energy Research Institute
Cidade Universitária
São Paulo (SP), Brazil

Fabiano Yokaichiya
Institut Quantenphänomene in neuen Materialien (EM-IQM)
Helmholtz-Zentrum Berlin für Materialien und Energie GmbH
Berlin, Germany

Section 1

Calculation of Small-Angle Scattering Patterns

Chapter 1

Calculation of Small-Angle Scattering Patterns

Cássio Alves and Cristiano Luis Pinto Oliveira

Additional information is available at the end of the chapter

http://dx.doi.org/10.5772/intechopen.74345

Abstract

Small-angle scattering (SAS) experiments applied to nano-scaled systems allow the investigation of the constituents' overall shape, size, internal structure and arrangement. A standard scattering experiment requires a relatively simple setup and is often applied to investigate a system of particles. In these cases, the measured scattering intensity represents an average over a large number of particles illuminated by the incoming beam. The calculation and modeling of the scattering intensity can be performed by the use of analytical/semi-analytical expressions or by the use of numerical methods. In this book chapter, an overview of current available simulation/modeling methods for SAS will be shown either for systems composed of oriented or for randomly oriented particles. Examples demonstrating the use of the finite element method are presented as well as a newly developed method for calculating scattering intensity for oriented particles.

Keywords: small-angle scattering, nanoparticles, finite element method, oriented particles, simulation, numerical methods

1. Introduction

The investigation of internal structure of system at nanoscale permits the comprehension and correlation of its microstructure to its macro properties. Theoretical and experimental methods are widely used to predict and characterize the properties of these systems [1]. Density functional theory (DFT), molecular dynamics (MD) simulations, and Monte Carlo (MC) simulations are just few examples of theoretical methods used for these investigations [2, 3]. However, all these theoretical methods have always to be checked and confirmed by the use of experimental results, in a large number of available experimental methods. Imaging techniques, when applicable, are very useful since they can provide a direct indication of the shape and size of the investigated system. Electron microscopy (EM) methods like transmission

electron microscopy (TEM) and scanning electron microscopy (SEM) give important information on the structures in high resolution [4–6]. However, these methods demand the use of special experimental conditions like measurements in vacuum and the use of coating agents. Therefore, the obtained results can be affected by the experimental technique itself [7]. Scattering/diffraction methods, on the other hand, can be used for systems directly in solution or in the amorphous matrix, with minimum interaction of the radiation with the matter [7, 8]. These methods, namely, small-angle scattering (SAS) either with neutrons (SANS) or X-rays (SAXS), static light scattering (SAS), etc., can provide useful information about the structure of the investigated system. However, scattering methods give information in the Fourier space (reciprocal space/scattering space) which can difficult its interpretation and modeling [8–10].

In this book chapter, a review about the calculation of scattering patterns from system composed of particles will be presented. First, an overall discussion about the basic scattering theory and the inverse scattering problem is shown. Later, several analysis and modeling methods are described and discussed. Finally, state-of-the-art methods with advanced applications are shown, demonstrating the use of possibility of simulating scattering patterns for oriented particles.

2. Overall aspects of small-angle scattering

There are several approaches for describing the interaction of electromagnetic radiation with matter. In this chapter, the scattering of an incident beam of radiation by a scattering potential will be assumed [7, 11–14]. A schematic view of the scattering process is shown in **Figure 1**.

The potential is assumed to be weak (first Born approximation), and therefore the scattering is considered to be elastic; it is also assumed that the radiation does not destroy the internal structures. The target is considered to be sufficiently thin in order to disregard multiple scattering events. In this description a plane monochromatic wave (far-field approximation) is scattered by a finite potential field $V\left(\vec{r}\right)$, and the wave function that expresses this phenomenon is a superposition of the transmitted plane wave e^{ikz} and scattered wave [7, 12–14].

$$\psi\left(\vec{r}\right) \sim \mathrm{e}^{\mathrm{ikz}} + \mathrm{A}_k \frac{e^{\mathrm{ikz}}}{r} \tag{1}$$

If the scattering potential is weak, the function $V\left(\vec{r}\right)$ is equal to the scattering length distribution function $\rho\left(\vec{r}\right)$, which is directly related to the particle shape. This information is contained in the scattering amplitude A_k, as shown below [7, 12–14]:

$$A_k\left(\vec{q}\right) = f\left(\vec{q}\right) A_0\left(\vec{q}\right) \tag{2}$$

where $\vec{q} = \vec{k_s} - \vec{k_i}$ is the momentum transfer vector, with modulus $q = \frac{4\pi}{\lambda}\sin\theta$ (λ is the radiation wavelength and 2θ the scattering angle), A_0 is an amplitude scattered by one electron

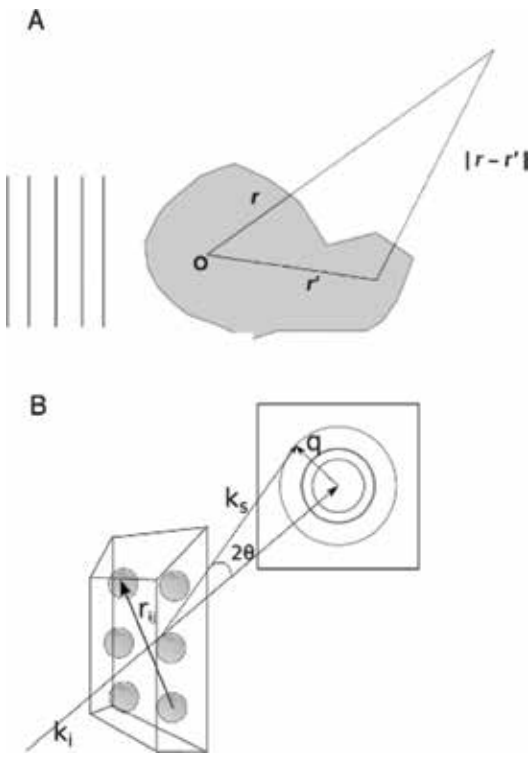

Figure 1. (A) Representation of the small-angle scattering of radiation by a potential. (B) Representation of scattering vector, angle of scattering, and pattern diffraction. Figure adapted from [15], reproduced with permission of the International Union of Crystallography.

(or atom), and the particle form factor $f\left(\vec{q}\right)$ is the Fourier transformation of the function $\rho\left(\vec{r}\right)$ [7, 12–14],

$$f\left(\vec{q}\right) = \int_V \rho\left(\vec{r}'\right) e^{-i\vec{q}\,\vec{r}'} d\vec{r}' \tag{3}$$

For the cases of particles immersed in a solvent or in a matrix, the important quantity is the scattering length contrast between the particles and the medium. The scattering length density of the matrix is assumed to be constant, and therefore the scattering length contrast is given by $\Delta\rho\left(\vec{r}\right) = \rho\left(\vec{r}\right) - \rho_{\text{Solvent}}$. Therefore, the scattering form factor is rewritten as [7, 12–14].

$$f\left(\vec{q}\right) = \int_V \Delta\rho\left(\vec{r}\right) e^{-i\vec{q}\,\vec{r}} d\,\vec{r} \tag{4}$$

The scattering intensity $I\left(\vec{q}\right)$ by an object is the product by scattering amplitude and its respective complex conjugate,

$$I\left(\vec{q}\right) = \mathrm{A}\left(\vec{q}\right) \cdot A\left(\vec{q}\right)^{*} = \left(A\left(\vec{q}\right)\right)^{2} = \int_V \int_V \rho\left(\vec{r}\right)\rho\left(\vec{r}'\right) e^{-i\vec{q}\left(\vec{r}-\vec{r}'\right)} d\vec{r} d\vec{r}' \tag{5}$$

Or, by using the self-correlation function [7, 12–14],

$$\gamma\left(\vec{r}\right) = \int_V \rho\left(\vec{r}\right)\rho\left(\vec{r}' - \vec{r}\right) d\vec{r}' \tag{6}$$

the scattering intensity can be rewritten,

$$I\left(\vec{q}\right) = \int_V \gamma\left(\vec{r}\right) e^{-i\vec{q}\,\vec{r}} d\,\vec{r} \tag{7}$$

If there is no preferential orientation in the system, it is necessary to perform averages over the particle orientation. In Eq. (7) this average gives rise to the calculation of the average correlation function $\gamma(r)$ or the pair distances distribution function $p(r) = r^2\gamma(r)$, which is widely used in SAS analysis [7, 12–14].

An interesting approach is to consider that the particle, or system, is composed by n scatters with scattering length contrast $\Delta\rho_j\left(\vec{r}\right)$. Each scatter will contribute with the scattering amplitude $f_j\left(\vec{q}\right)$ (Eq. (4)), and the resulting scattering amplitude is the composition of the scattering amplitudes and its phase factors,

$$A\left(\vec{q}\right) = \sum\nolimits_l^n f_j\left(\vec{q}\right) e^{i\vec{q}\,\vec{r}} \tag{8}$$

Therefore, the total scattering intensity from the group of n scatters at relative positions $\left(\vec{r}_j - \vec{r}_l\right)$ is given by [7, 12–14].

$$I\left(\vec{q}\right) = \sum_j^n \sum_l^n f_j\left(\vec{q}\right) f_l\left(\vec{q}\right) e^{-i\vec{q}\left(\vec{r}_j - \vec{r}_l\right)} \tag{9}$$

It is interesting to mention that Eq. (9) can represent a single particle composed by n subunits or a system composed of particles dispersed in a matrix. Both situations are described by this equation, and several simulation methods are based on it.

By assuming no preferential orientation, from Eq. (9), one obtains the resulting average scattering intensity,

$$\left\langle I\left(\vec{q}\right)\right\rangle = \sum_{\mathrm{j}=1}^{n} \left\langle \left(f_j\left(\vec{q}\right)\right)^2 \right\rangle + 2\left\langle \sum_{j\neq \mathrm{l}=1}^{n} \sum^{n} f_j\left(\vec{q}\right) f_l\left(\vec{q}\right) e^{-i\vec{q}\left(\vec{r}_j - \vec{r}_l\right)} \right\rangle \tag{10}$$

For a system composed of particles at very low concentration, the interference term (second part of Eq. (10)) goes to zero, and the resulting average scattering intensity is [7, 12–14].

$$\left\langle I\left(\vec{q}\right)\right\rangle = \sum_{j=1}^{n}\left\langle\left(f_j\left(\vec{q}\right)\right)^2\right\rangle = \mathrm{n}\left\langle\left(f\left(\vec{q}\right)\right)^2\right\rangle = \mathrm{n}\left\langle(f(0))^2\right\rangle P(q) = \mathrm{n}I_1(q) \tag{11}$$

where $P(q) = \left(f\left(\vec{q}\right)\right)^2 \Big/ (f(0))^2$ is the so-called averaged normalized form factor of the particle. Eq. (11) is very important because it demonstrates that the scattering intensity from a system of particles at very low concentration is proportional to the scattering of a single particle.

If the system is concentrated, the second term in Eq. (10) cannot be neglected. Depending on the system characteristics, several approximations can be performed. It is beyond this chapter to consider all possible approaches for the calculation of this interference term on concentrated systems; good reviews can be found in the literature [14, 16–22]. A usual approach is to decouple the particle shape and interparticle interactions. In this way, the particle form factor $P\left(\vec{q}\right)$ and system structure factor $S\left(\vec{q}\right)$ are introduced:

$$I\left(\vec{q}\right) = \mathrm{n}\mathrm{I}_0 P\left(\vec{q}\right) S\left(\vec{q}\right) \tag{12}$$

In a typical scattering experiment, after interacting with the sample, the scattered radiation is detected, generally, in a two-dimensional detector. In this case, the obtained image is, depending on sample, isotropic or anisotropic, and these patterns are related to the particle shape and size and possible interparticle interactions. The collected scattering intensity is a direct representation of the data in reciprocal space. Therefore, the analysis of SAXS experiment consists in the interpretation of this data in order to retrieve structural information in real space. Even though the real space is three-dimensional, the collected scattering data are two-dimensional (projection on a specific plane) or one-dimensional (particles randomly oriented or a specific $\vec{q}$ direction). Several modeling methods will be discussed for the calculation of scattering intensities from oriented and randomly oriented particles dispersed in a homogeneous matrix. Examples of these methods are the use of analytical and semi-analytical expressions, cube and sphere method, spherical harmonics, optimized Debye formula to systems oriented and randomly oriented, and fast Fourier transformation [12, 14, 23, 24].

3. Modeling methods for SAS data

After the scattering data is collected, it is necessary to perform several procedures to have the scattering intensity ready to be analyzed. The data treatment of the scattering data includes normalization of the intensity, background subtraction, and normalization to absolute scale among several steps, which depends on the specific characteristics of the experimental setup. The overall data treatment process and necessary procedure for proper reduction of the scattering data are described in many articles and books in the literature and will not be presented here [7, 12, 14, 15, 23–29]. In this chapter we will focus on methods for calculation of the SAS intensity, either for oriented or randomly oriented particles.

Form factor amplitude	
Sphere	(13)
$f_s(q, R) = \frac{3[\sin(qR) - qR\cos(qR)]}{(qR)^3}$	
R is the radius of the sphere.	
Spherical shell	(14)
$f_{ss}(q, R) = \frac{V(R_{out}) f_s(q, R_{out}) - V(R_{in}) f_s(q, R_{in})}{V(R_{out}) - V(R_{in})}$	
R_{in} and R_{out} are the inner and outer radius of the shell and V is spherical volume.	
Tri-axial ellipsoid	(15)
$f_{er}(q, R) = f_s(q, R(R_1, R_2, R_3))$	
$R(R_1, R_2, R_3) = \left[\left(R_1^2 \sin^2\beta + R_2^2 \cos^2\beta\right) \sin^2 + R_3^2 \cos^2\alpha\right]$	(16)
R_1, R_2 and R_3 are the semi-axes of the ellipsoid.	
Cylinder	(17)
$f_c(q, R) = \frac{2J_1(qR\sin\alpha)}{qR\sin\alpha} \frac{\sin[(qL\cos\alpha)/2]}{(qL\cos\alpha)/2}$	
R is the radius, L is the length of the cylinder and $J_1(x)$ is the first-order Bessel function of the first kind.	
Rectangular prism	(18)
$f_p(q, R) = \frac{\sin(qa\sin\alpha \ \cos\beta)}{qa\sin\alpha\cos\beta} \frac{\sin(qb\sin\alpha \ \sin\beta)}{qb \ \sin\alpha\sin\beta} \frac{\sin(qc\cos\alpha)}{qc\cos\alpha}$	
a, b and c are the edge lengths.	

Table 1. Analytical and semi-analytical expressions for simple shapes.

The calculated intensity can be compared with experimental scattering data, and the model parameters can be optimized in order to improve the agreement between the theoretical and experimental data. The χ^2 (chi-square) test is widely used for scattering experiments because the basic assumption of this test, Gaussian distribution of uncertainties around a certain value, is fulfilled in SAS data. In this test the sum of squares of the differences between experimental and theoretical intensities is divided by the variance on each point, as shown below [7, 17, 30]:

$$\chi^2 = \sum_{i=1}^{N} \frac{\left[I_{\exp}(q_i) - I_{simu}(q_i)\right]^2}{\sigma^2(q_i)} \tag{19}$$

If the χ^2 (chi-square) test is normalized by the difference between the number of experimental data points and the number of independent parameters, a good fitting is obtained when the normalized χ^2 approaches 1. This means that the differences between experimental and theoretical data are of the order of standard deviations.

3.1. Analytical and semi-analytical methods

For the cases where the particle has a simple shape, it is possible to have analytical or semi-analytical expressions for the scattering intensity. There are a large number of examples in the literature [30], and some examples are shown in **Table 1**.

The use of the analytical and semi-analytical equations has the advantage of calculating the scattering intensities with a good precision, low computational cost, and very low number of model parameters. If the particles are randomly oriented, it is necessary to perform angular averages on the equations shown in **Table 1**. Also, if the system is diluted but has polydispersity in size, it is possible to calculate the resulting average scattering intensity by the use of appropriate equations, which are described in the literature [30].

The calculation of the scattering intensity is reasonably fast and can be performed with high precision. However, analytical or semi-analytical expressions are only available for simple shapes [13, 14, 16, 30]. There are several programs available in the literature with a large database of equations for modeling scattering data as the SASfit program [31], among many others. In the webpage **smallangle.org**, there is an updated list of available programs.

3.2. Cube method

Fedorov et al. [32–34] and Ninio et al. [35] proposed the so-called cube method, where the models of macromolecules in solution are surrounded by the solvent (or by the matrix where the particles are immersed), and the cube method permits a correct calculation of the volume inaccessible to the solvent. The theoretical intensity is given by

$$I\left(\vec{q}\right) = \left(f\left(\vec{q}\right) - \phi\left(\vec{q}\right)\right)^2 \tag{20}$$

where $f\left(\vec{q}\right)$ is the scattering amplitude of the macromolecule in vacuum and $\phi\left(\vec{q}\right)$ has the same volume of the molecule but with homogeneous electron density ρ_0 [32, 33]. The calculation of the scattering amplitude of a protein macromolecule with known atomic coordinates can be done with the equation,

$$f\left(\vec{q}\right) = \sum_k f_k(q) e^{i\vec{q}\vec{r_k}} \tag{21}$$

where $f_k(q)$ is the scattering factor of the kth atom and $\vec{r_k}$ is its coordinate. The determination of $\phi_k\left(\vec{q}\right)$, the scattering amplitude of the homogeneous substance filling the macromolecule and its excluded volume, is not trivial, and several authors proposed solutions for it [21, 32, 33, 35, 36].

The idea is to put the macromolecule coordinates in a cubic grid composed of small cubes with edges of 0.5–1.5 Å. The calculated intensity depends on a specific $\vec{q}$ direction. In order to perform random orientation over direction Z, one can take N directions, in reciprocal space, on an sphere of radius q, so the average scattering intensity is given by [32, 33]

$$I(q) = \frac{1}{N}\sum_{j=1}^{N} I\left(\vec{q}\right) \tag{22}$$

Virtanen and collaborators presented in 2011 an adaptation of the cube method [37, 38], using a procedure, known as HyPred. Basically, these authors were inspired in cube method, to

simulate scattering intensities, and also in molecular dynamics (MD) simulations, to find the hydration layer of a protein. In this procedure, with atomic resolution precision, the nonuniform solvent density around a protein is calculated [38]. With this information one can calculate both small- and wide-angle X-ray scattering (SAXS/WAXS) intensities. In 2014, Nguyen and collaborators presented another adaptation of the cube method [39], using RISM (reference interaction site model) theory. In this application the cube method is used to calculate the contribution from the solvent at amplitude scattering, and in 2016 Nguyen and collaborators [40] proposed a procedure to extract information about water and ion distributions from analysis of SAXS experiments. This method allows to compute the solvent distribution around the solute allowing to calculate scattering intensities at small- and wide-angle X-ray (SAXS/WAXS) and with less computational time than MD [39, 40]. One example [39] of these applications, using RISM-SAXS and HyPred, is shown in **Figure 2** for lysozyme and shows a good agreement with experimental data to both applications. The results from other applications were also shown just for comparison. There is a good agreement between the experimental data and the simulation performed by HyPred and RISM. CRYSOL obtained a good fit with the experiment up to 1.5 $Å^{-1}$. The program CRYSOL [41] has been used as standard program for such calculations and uses the multipole expansion to calculate scattering intensities; this approach will be discussed at Section 3.4. The web server FoXS is based on the Debye formula, and this formula will be discussed in the next section. The web server program AXES calculates the scattering amplitudes of the surface of solvent using a sum of the six elementary scattering functions averaged [42]. The web server AquaSAXS [43] computes SAXS/WAXS profile of a given structure, and PDB or PQR file is necessary to perform the calculation.

The HyPred method is very useful for the determination of excluded volumes and contrasts. However, it requires the numeric calculation of the intensities, and if the cubic grid is very small, the computational time for the calculation of intensity is very long. Approaches using spherical harmonics proved to be more efficient and precise for the calculation of scattering intensities for usual investigations of macromolecules in solution [36, 41].

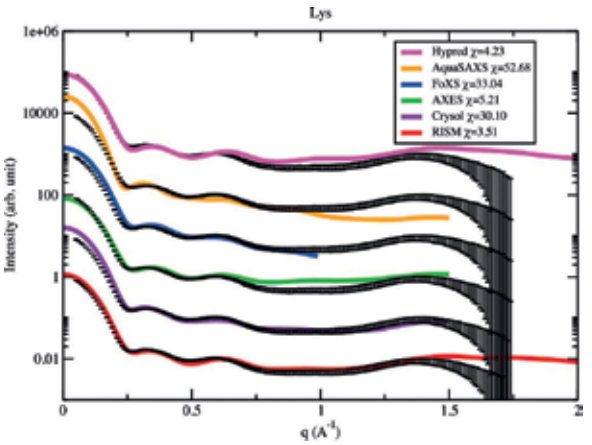

Figure 2. Comparison between other methods for calculation SAXS of lysozyme: CRYSOL, FoXS, AXES, AquaSAXS, and HyPred. Figure reprinted (adapted) from [39], with the permission of AIP publishing.

3.3. Sphere method and Debye formula

Considering a system composed of n identical scatters, randomly oriented, it is possible to rewrite Eq. (10) as

$$\frac{\left\langle I\left(\vec{q}\right)\right\rangle}{I_0} = \left\langle \left(f\left(\vec{q}\right)\right)^2 \right\rangle \left(\left\langle \sum_{\mathrm{j}=1}^{n} \sum_{\mathrm{l}=1}^{n} e^{-i\vec{q}\left(\vec{r}_j - \vec{r}_l\right)} \right\rangle \right) = \left\langle \left(f\left(\vec{q}\right)\right)^2 \right\rangle \left(\mathrm{n} + 2 \sum_{j \neq \mathrm{l}=1}^{n} \sum^{n} e^{-i\vec{q}\left(\vec{r}_j - \vec{r}_l\right)} \right) \tag{23}$$

and calculating the average over all possible orientations,

$$\left\langle e^{-i\vec{q}\left(\vec{r}_j - \vec{r}_l\right)} \right\rangle_{\Omega} = \frac{\sin\left(q\left(\vec{r}_{\mathrm{jl}}\right)\right)}{q\left(\vec{r}_{\mathrm{jl}}\right)} \tag{24}$$

it is possible to obtain the Debye equation [12, 44],

$$\frac{I\left(\vec{q}\right)}{I_0} = \left(f\left(\vec{q}\right)\right)^2 \left(\mathrm{n} + 2 \sum_{j \neq \mathrm{l}=1}^{n} \sum^{n} \frac{\sin\left(\mathrm{qr}_{\mathrm{jl}}\right)}{\mathrm{qr}_{\mathrm{jl}}} \right) \tag{25}$$

where $f\left(\vec{q}\right)$ is the scattering amplitude of a sphere (Eq. (13)).

The Debye equation is very useful because it is possible to compose the volume of the particle by a sum of small spherical volumes. This modeling method, also known as finite element (FE) method, allows the description of the particle shape by the use of small subunits.

The main advantage of this method is that one can easily model very complex objects. However, it has the disadvantage that the calculation is proportional to n^2, where n is the number of the small objects used in the model. The subunit size defines the precision of the method: the maximum q value that can be calculated without the influence of the subunits' form factor is limited to $q \leq \pi / r_s$ ($\mathrm{r_s}$ is radius of spherical subunits) [14]. Therefore the precision of the method increases with the number of subunits used to represent the particle.

Oliveira and collaborators [45, 46] used this kind of procedure to show the first analysis of nanocage structures using scattering radiation techniques. The authors were interested in discovering the influence in the stability and yield to build experimental DNA octahedron nanocages in solutions, using double and single DNA strands [45]. Then, to perform the modeling and compare with experimental data, the double DNA helix models are positioned in the edge, in octahedron geometry, that was truncated by single DNA strands that perform linkers between the helices. Altogether, there are 12 double-stranded B-DNA helices with 18 base pairs each (positioned in the edges) and 24 single-stranded (making truncation procedure). The stability and yield of nanocages were tested varying the length of single strands, with three, four, five, six, or seven nucleotides (to build the linker).

The SAXS models are built using bead atoms, representing DNA in the edge and in linkers of the cages. These DNA models are rigid, and each bead atom is spherical, representing a nucleotide positioned in atom of C2* (PDB format [47]). The scattering intensities were simulated using Debye equation, Eq. (25). The results are shown in **Figure 3**, where the simulated theoretical intensity was adjusted to each experimental SAXS data, for the five kinds of nanocage. From this analysis it was possible to obtain the relations between the cage size and the linker size and also the presence of high-order agglomerates (dimers and trimers of cages).

Even with the increase of performance of the new computer processors, the use of the Debye equation is limited to few dozens of subunits, since it involves a double sum. In the next sections, some procedures to speed up the calculation decreasing the computational costs will be shown.

3.4. Spherical harmonics and multipole expansion

In the late 1960s, Harrison [48] and later Stuhrmann and Svergun [36, 49] proposed an alternative procedure to compute scattering intensities for particles. The main idea is to express the scattering length distribution function distribution $\rho\left(\vec{r}\right)$ as a series of spherical harmonics [14], which describes an angular envelope function $F(\omega)$,

$$\rho\left(\vec{r}\right) = \begin{cases} 1, 0 \le r \le F(\omega) \\ 0, \quad r \le F(\omega) \end{cases} \tag{26}$$

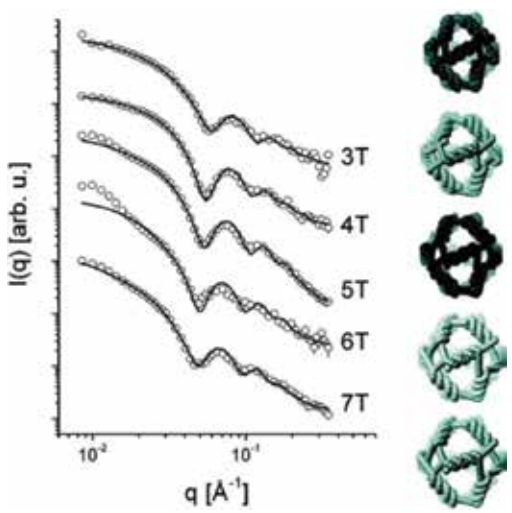

Figure 3. Fitting of the experimental data with the truncated octahedron model. Left: Fits of the experimental data for the samples with different thymidine linker lengths using the geometrical model. The data sets were shifted for clarity. Right: Resulting three-dimensional structures obtained from the modeling of the experimental data. Figure reprinted (adapted) with permission from [45]. Copyright (2018) American Chemical Society.

The envelope function $F(\omega)$ is parameterized using multipole expansion

$$F(\omega) = F_L(\omega) = \sum_{r=0}^{L} \sum_{m=-l}^{l} f_{lm} Y_{lm}(\omega) \tag{27}$$

where $Y_{lm}(\omega) = Y(\theta, \omega)$ are spherical harmonics and the multipole [14] coefficients f_{lm} are complex numbers,

$$f_{lm} = \int_{\omega} F(\omega) Y^*_{lm}(\omega) d\omega. \tag{28}$$

The scattering amplitude $A\left(\vec{q}\right)$ is given by,

$$A\left(\vec{q}\right) = \sum_{r=0}^{L} \sum_{m=-l}^{l} A_{lm}(q) Y_{lm}(\omega). \tag{29}$$

The spatial resolution of the shape representation (Eq. (27)) is defined by the truncation value L. Thus the particle shape is parameterized by $(L+1)^2$ members. Also, the accuracy of its representation increases with L [14, 36, 50].

The shape scattering intensity is expressed as

$$I(q) = 2\pi^2 \sum_{r=0}^{L} \sum_{m=-l}^{l} |A_{lm}(q)|^2 \tag{30}$$

where the partial amplitudes A_{lm} are represented by the power series,

$$A_{lm}(q) = (iq)^l \left(\frac{2}{\pi}\right)^{\frac{1}{2}} \sum_{p=0}^{p_{max}} \left[(-1)^p f_{lm}^{(l+2p+3)} \{2^p p!(l+2p+3)[2(l+p)+1]!!\}^{-1} q^{2p}\right] \tag{31}$$

The use of spherical harmonics permits the description of low-resolution shapes with a relatively low number of parameters, and it was the first approach capable to obtain the particle shape directly from the scattering intensity, without any a priori information. This is the first of the so-called ab initio modeling methods for SAS data analysis. This method was implemented in a program, namely, by SASHA [50], and provides the angular envelope function that gives the best fit of the scattering data. This application is a good option in determination of low-resolution structure without internal cavities and without sharp edges or corners, limited to smooth shapes.

One example of application is shown in **Figure 4**. In this work, Arndt and collaborators investigated extracellular proteins [51]. By using SAXS investigations, in particular the spherical harmonics approach (program SASHA), it was possible to obtain low-resolution models for the protein *Biomphalaria glabrata* in pH 7 and pH 5.

The description of particle shape using the envelope function $F(\omega)$ was a major step for the calculation of the scattering from macromolecules in solution [41]. Given the atomic coordinates for the macromolecule, it is possible to calculate the scattering intensity and excluded

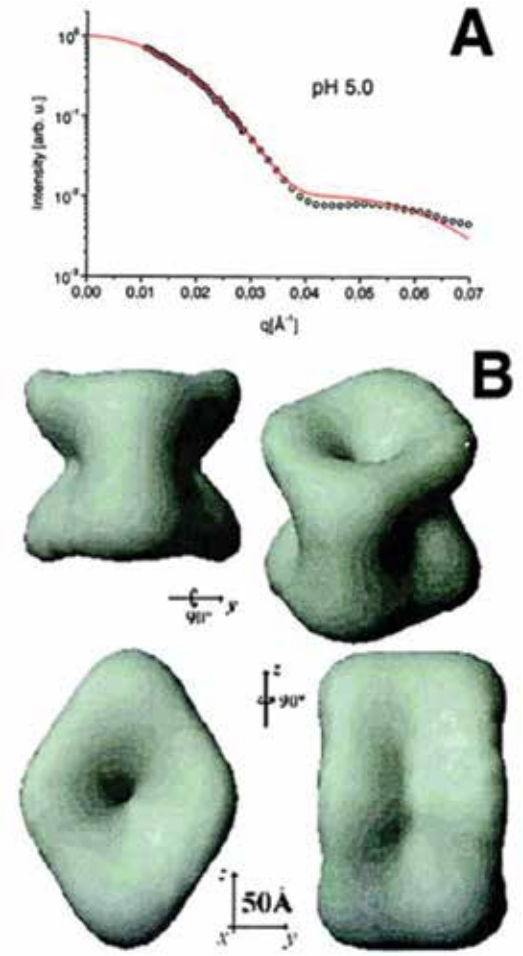

Figure 4. External envelope of the hemoglobin from *B. glabrata* calculated using the multipolar expansion method. (A) Fitting of the low-angle part of the scattering curve (qmax~ 0.07 $Å^{-1}$) by the multipolar expansion method for the hemoglobin at pH 5. (B) Solid surface views of the hemoglobin at pH 5. Figure adapted and reproduced from [51], with permission of the John Wiley & Sons, Inc.

volume for the macromolecule. This was implemented in the program CRYSOL and readily demonstrates the presence of a hydration shell around macromolecules in solution. The use of spherical harmonics permits a very fast calculation of the scattering intensity and opened new research lines and opportunities for the use of SAS data.

In the late 1990s, Svergun's group proposed a set of tools combining the use of spherical harmonics to calculate scattering amplitudes and variation of the Debye equation. In the program called DAMMIN [52], a search space filled with spherical beads is created, and by the use of a heuristic optimization based on Monte Carlo approach (simulated annealing, SA [53]), a subset of this set of spheres is selected in order to provide the best fitting of the scattering data. The expression used for the calculation of the scattering intensity is [52]

$$I(q) = 2\pi^2 \sum_{r=0}^{\infty} \sum_{m=-l}^{l} \left\{ \sum_{k=1}^{K} \left[\Delta\rho_k A_{lm}^{(k)}(q) \right]^2 + 2 \sum_{n>k} \Delta_k \rho_k A_{lm}^{(k)}(q) \Delta\rho_n \left[A_{lm}^{(n)}(q) \right]^* \right\} \tag{32}$$

The use of spherical harmonics speeds up the calculation process, which is the main drawback of the original Debye equation (Eq. (25)).

Other ab initio methods using the dummy atom approach were proposed by many other authors but using optimized implementations of the Debye equation (see the next section). Chacon [54, 55] proposed ab initio methods using genetic algorithm procedures for the model optimization. A modified procedure was proposed by Doniach and collaborators [56] changing the genetic algorithm by the so-called "Give'n'Take" algorithm. Due to its functionality and special features (inclusion of symmetry constraints, multiple curve fitting, etc.), the program DAMMIN is the most used and cited in the literature.

Further implementations performed for the use of ab initio methods applied to the study of macromolecules in solution took advantage of the known atomic resolution information for proteins, available in the protein data bank (https://www.wwpdb.org/) [47], and composes the ATSAS program suite [17, 41, 57–69]. Several good reviews can be found in the literature for this subject [14, 17, 36, 50, 60, 65, 67–69].

3.5. Optimized Debye equation

The Debye equation assumes that the subunits are identical and the arrangement of the subunits defines the particle shape. As mentioned before, the double sum involved in the calculation limits the number of subunits since the computational time increases with $O(n^2)$. In order to decrease the computational time, Glatter proposed the use of histograms of distances inside the particle [70]. With this procedure the double sum, Eq. (25), is converted in a single sum [70, 71],

$$\frac{\left\langle I\left(\vec{q}\right)\right\rangle}{I_0} = |f(q)|^2 \left[n + 2 \sum_{k=1}^{nbins} h(r_k) \frac{\mathbf{sin}\,(qr_k)}{qr_k} \right] \tag{33}$$

by the use of the histogram of distance between the subunits $h(r_k)$ that compose the model. In this new equation, optimized Debye equation, the construction of the histogram still involves a double sum, but it is performed only once. All the further calculations are done in a single sum, over the histogram bins. If the subunits in the model are randomly distributed, the intensity calculation can be again optimized, dividing the histogram into blocks. So, the computational time cost decreases to $O[n/num_{blocks}]$, where num_{blocks} is the number of blocks [8, 72, 73].

In **Figure 5A** the comparison between analytical equations, **Table 1**, and the same models built with the FE method and the intensities calculated with the optimized Debye equation is illustrated. The very good agreement between the theoretical analytical intensities and the calculated intensities with the optimized Debye equation demonstrates the precision of the method for its use in calculating complex shapes.

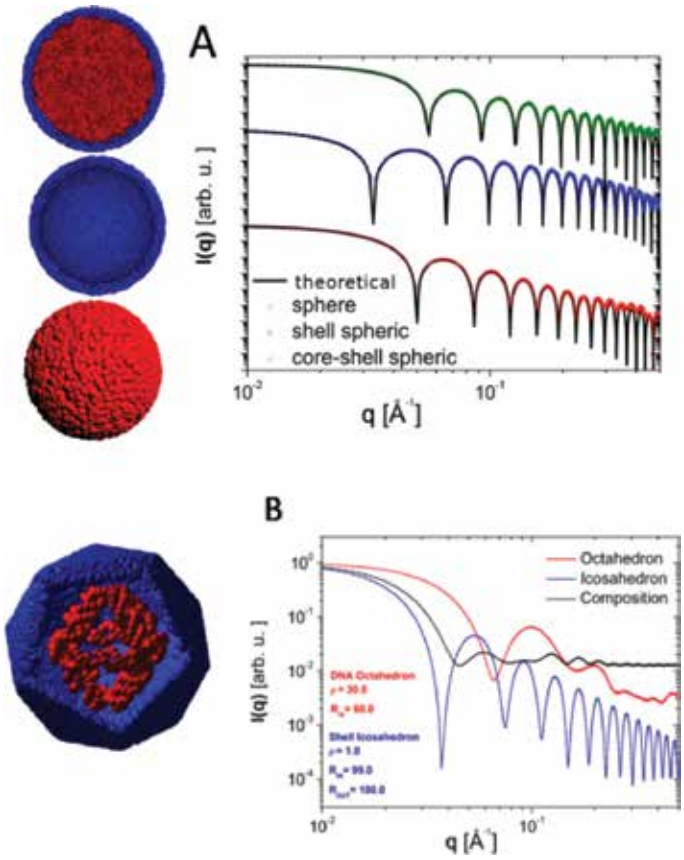

Figure 5. Computation of test examples for simple and composition models. (A) (left) Models assumed. (right) The calculation for solid spheres, spherical shells, and spherical core-shell structures, compared with theoretical expressions. (B) Composition of a shell-like structure with a DNA cage in its interior. (left) Models assumed. (right) Calculated scattering intensities. The assumed sizes and relative electron densities for each object are given on the figure. Figure adapted from [8], reproduced with permission of the International Union of Crystallography.

In **Figure 5B** two models were built using FE method. The red (internal) model is a DNA cage. The DNA molecule was modeled using coarse-grained approach, so each nucleotide corresponds to one spherical subunit place in positions of C2*. The blue model is an icosahedral shell-like structure. The composed model is an icosahedral shell-like with a DNA cage in its interior. The calculation of the scattering intensity was performed using the optimized Debye equation in a slightly different implementation in order to include different contrasts and demonstrate the potential use of this approach. In the figure of the original article is possible see that the histogram approach also permits an easy computation of affine polydispersities [8, 73].

3.6. Fast Fourier transformation

Schmidt-Rohr [74] proposed the use of a direct method, based on the use of Fourier transform (FT) of a three-dimensional model, to calculate the intensity scattering. Basically, the

three-dimensional model is defined, a priori, on a cubic discrete lattice of dimension Na, with N^3 points spaced by a value a and with a scattering density $\rho_{latt}\left(\vec{x}\right)$. So, using the 3D discrete (fast) FT (FFT), it is possible to find the scattering amplitude [74],

$$A\left(\vec{q}\right) = \left|DFT\left[\rho_{latt}\left(\vec{x}\right)\right]\right| \tag{34}$$

To obtain the intensity for a subunit, one can use the equation below,

$$\boldsymbol{I}\left(\vec{q}\right) = \left|\boldsymbol{DFT}\left[\boldsymbol{\rho}_{latt}\left(\vec{x}\right)\right]\right|^2 \left\{\frac{\prod_{m=1}^{3} \sin\left(\frac{q_m a}{2}\right)}{\frac{q_m a}{2}}\right\}^2 \tag{35}$$

where m is the number of the dimensions. The orientation averaging is performed in the final stage, where the sum of the intensity correspondents to each small (discrete) subunit of the lattice is realized (using a procedure developed by author called "channel sharing") followed by a normalization procedure by q^2. This procedure has a low computational cost of $O(N.lnN)$, and, according to this author, the FFT could be applied to obtain two-dimensional diffraction patterns [74, 75].

For a system of identical particles, the total intensity is represented by the convolution of the spatial points of the particles' center of mass $\sum_n \boldsymbol{\delta}\left(\vec{x} - \vec{x}_n\right)$ together with the density distribution of one particle $\boldsymbol{\rho}\left(\vec{x}\right)$ [74],

$$I\left(\vec{q}\right) = \left|FT\left[\sum_n \delta\left(\vec{x} - \vec{x}_n\right)\right]\right|^2 \left|FT\left[\rho\left(\vec{x}\right)\right]\right|^2 = S\left(\vec{q}\right)P\left(\vec{q}\right) \tag{36}$$

Schmidt-Rohr and Chen [74, 76] showed an application of this method to quantitatively simulate small-angle scattering data of hydrated Nafion and were capable to explain the "ionomer peak" visualized in SAXS patterns has been related to the randomly packed water channels internal to cylindrical inverted micelles. These results demonstrated the good transport properties of hydrated Nafion and have given details about its internal structure like diameters of water channels, cluster sizes, the shape of channels, and crystallinity levels [76].

An advantage of this method is the order of computational cost, O(NlogN), but on the other hand, it does not present the good results when used to systems where the SAS features are of the order of size of systems. For this kind of systems, Monte Carlo distribution function method (MC-DFM) gives better results [75] (the MC-DFM uses optimized Debye equation, Eq. (33), to simulate scattering intensities). Olds and collaborators [75] compared the efficiency of these two methods and suggest that the use of FFT method is more efficient for dense systems and complex dense-packed particle systems such as high-density polydisperse hard-sphere models. In this last case, systems of dense arrays of monodisperse spheres, the FFT method can be at least three times more efficient. However, for systems of low density such as

extended polymers and dilute systems, FFT is inefficient and is also less useful for systems where it is possible to use the diffuse character of the model and use the atomic coordinates. So, to large model particle systems, dilute particle arrays, polymers, and proteins, the MC-DFM can be a more efficient procedure [75].

3.7. Optimized Debye equation for oriented particles

The FE method can also be used to calculate the scattering intensities for oriented systems or particles. The calculation can be performed by the use of Eq. (9), but the practical application of this formula is limited since it involves a double sum and vectorial arguments, which makes the computational costs very high. Since the particles are oriented, the scattering intensity is anisotropic and therefore is necessary to compute the two-dimensional scattering pattern. A possible approach was proposed in the seminal Guinier-Fournet book [12] and consists in applying the equation below

$$\frac{I\left(\vec{q}\right)}{I_0} = \left[\sum_{i=1}^{n} f_i\left(\vec{q}\right) \cos\left(\vec{q}\ \vec{R}_i^{origin}\right)\right]^2 \tag{37}$$

to calculate the scattered intensities in a specific direction. However, this equation can only be used to centrosymmetric particles, which largely limits its application.

Sjöberg [77] proposed an approach to investigate the effects of interparticle correlations. In this approach the particles or molecules have known form factor, and the correlations can be obtained by the use of single sums, as shown below,

$$\frac{I\left(\vec{q}\right)}{I_0} = \left[\sum_{i=1}^{n} f_i\left(\vec{q}\right) \cos\left(\vec{q}\ \vec{R}_i^{origin}\right)\right]^2 + \left[\sum_{i=1}^{n} f_i\left(\vec{q}\right) \sin\left(\vec{q}\ \vec{R}_i^{origin}\right)\right]^2 \tag{38}$$

One of the main difficulties on simulating anisotropic two-dimensional scattering pattern is the computational time required to perform the calculation. For example, to make a scattering image with side of m = 512 pixels (a total of 262,144 pixels), it is necessary to perform the calculation for each pixel (which defines a specific $\vec{q}$ value) and for each scatter (n scatters). The calculation is impractical for small models (low number of scatters) even in the nowadays computers. These were the main difficulties presented by McAlister and Grady in their first approach to this problem [25, 26].

In order to overcome these limitations, Alves and collaborators [15] recently proposed an innovative procedure to solve this problem. Inspired by the histogram approach used in the optimized Debye equation Eq. (33), it is possible to convert the double sum in Eq. (9) into a single sum over the bins of the histogram. This new equation

$$\frac{I\left(\vec{q}\right)}{I_0} = \left|f\left(\vec{q}\right)\right|^2 \left[n + 2\sum_{k=1}^{n_{bins}^{\vec{q}}} h\left(\hat{q}\cdot\vec{r_{jl}}\right)_k \cos\left[\left(\vec{q}\cdot\vec{r_{jl}}\right)_k\right]\right] \tag{39}$$

http://dx.doi.org/10.5772/intechopen.74345

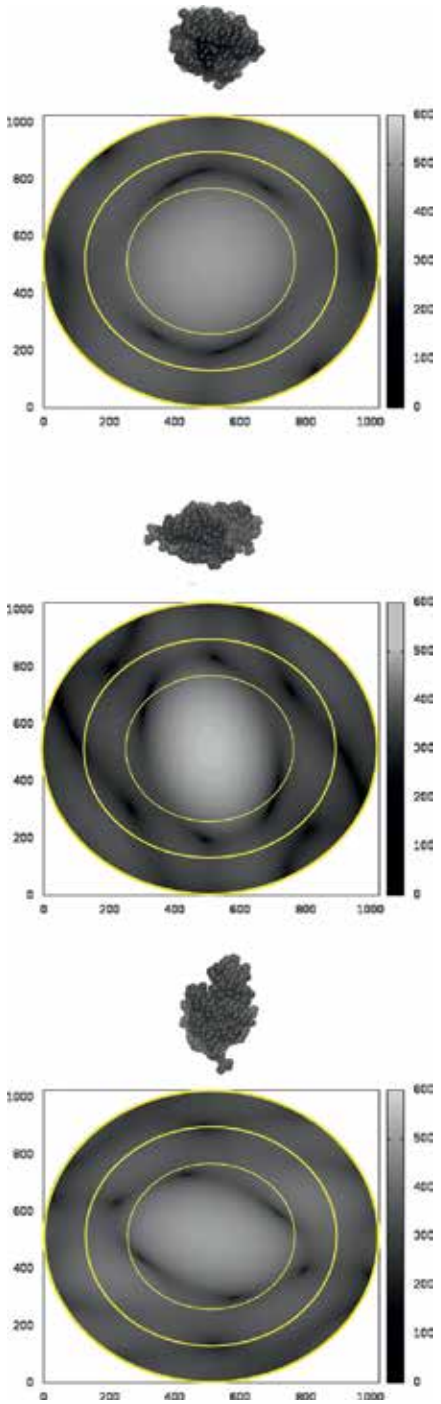

Figure 6. Calculation of 2D scattering patterns for oriented lysozyme (6lyz.pdb). The orientations are indicated in the figure. Figure adapted from [15], reproduced with permission of the International Union of Crystallography.

permits the fast calculation of the scattering intensity in a given $\vec{q}$ direction. $n_{bins\vec{q}}$ is the number of channels of histogram, $\hat{q}$ is a unitary scattering vector, and $\vec{r_{jl}}$ is the distance vector between the subunits composing the model.

The values for the dot product of $\hat{q} \cdot \vec{r_{jl}}$ are used to create the histogram of the projection distances $h\left(\hat{q} \cdot \vec{r_{jl}}\right)_k$, in a specific direction. The construction of the histograms still involves a double sum but is performed only once. Having the histograms, the intensities are easily calculated. One strategy proposed by Alves et al. [15] is to divide the 2D scattering image in angular slices and compute the histograms for each direction. As shown by the authors, the calculation can be further optimized by the use of parallel computing.

The precision of the method is demonstrated by the use of known analytical equations for simple shapes, as the ones shown in **Table 1**. Several examples demonstrating the precision of the method are described in the original article [15]. This new method opens a large number of possibilities for the calculation of scattering intensity for oriented particles.

Recent applications using X-ray free-electron lasers (FEL) are capable to produce intense ultrashort pulses (femtoseconds), in nanometer-sized coherent beams, irradiating particles in solution. Due to the special properties of these experiments, it is possible to irradiate single particles. Since the pulse durations are shorter than the characteristic rotational diffusion time of the particle, the obtained scattering intensity corresponds to particle oriented in a given direction. Therefore, if the system is composed of identical particles, multiple scattering images correspond to the scattering intensities from multiple orientations of the particles.

Several authors propose methods to describe the coherent scattering pattern and recover the three-dimensional structure of the scattering particle, based on the method proposed by Kam [78–80]. The proposed method for calculation of oriented scattering intensities can potentially be used to describe data from FEL experiments. To demonstrate this potentiality, in **Figure 6** the two-dimensional scattering pattern simulated for the protein lysozyme in several orientations is presented. This simulation method can also describe models with variable scattering length contrasts and interparticle interactions (structure factor). Several examples can be found in the original article [15].

4. General conclusions and perspectives

In this chapter a general overview about several procedures to calculate scattering intensifies for system of particles was presented. After a brief description of the general theoretical aspects, several methods for the calculation of scattering intensities were shown, with some typical applications. The main points and limitations of each procedure were discussed.

The analytical calculation of the scattering intensity is restricted to particles with simple geometries. More complicated shapes require the use of simulation methods. The Debye equation provided a first indication in this direction by the use of spherical subunits to build the particle

(finite element description—FE) and calculate the scattering intensity for randomly oriented averaging. Its variation, with the use of cubic subunits, gives the so-called cube method. This approach permitted a better calculation of excluded volumes but requires numerical averaging for account for the random orientation or the particles. The original Debye equation involves a double sum which is very inefficient (high computational costs) and cannot be applied for a large number of subunits. Optimized forms of the Debye equation were proposed by the use of histograms of pair distances, which turn the double sum on the number of particles into a single sum over the histogram bins. In this way, this method could be used for fast calculation of scattering intensities and modeling methods. Another modeling method was the use of spherical harmonics for the calculation of the scattering intensity. With the introduction of the envelope function to describe the particle shape, this method proved to be very powerful for the description of proteins in solution and the description of hydration layers. In the last decades, this approach and its development combined with ab initio methods promoted a revolution on the use of scattering data for the investigation and modeling of macromolecules in solution. Fast Fourier transformation methods have been recently applied to calculate the scattering patterns for known shapes, with very interesting applications. Also, based on the FE method, one can use a special development of the optimized Debye equation to compute scattering intensities for oriented particles. This innovative approach permits the fast calculation of 2D scattering patterns and provides new perspectives for the use and analysis of the small-angle scattering method.

Acknowledgements

CLPO is supported by FAPESP, CNPQ, and INCT-FCx. We acknowledge the Crystallography Journals Online (https://journals.iucr.org/), AIP Publishing LLC, American Chemical Society, and John Wiley & Sons, Inc. for permitting the reproduction of the figures used.

Conflict of interest

The authors declare that they do not have any "conflict of interest."

Author details

Cássio Alves[1] and Cristiano Luis Pinto Oliveira[2*]

*Address all correspondence to: crislpo@if.usp.br

1 Department of Engineering and Sciences, Federal University of Paraná, Palotina, Paraná, Brazil

2 Institute of Physics, University of São Paulo, São Paulo, Brazil

References

[1] Jones RAL. Soft Condensed Matter. Oxford: Oxford University; 2002

[2] Hamley IW. Introduction to Soft Matter : Polymers, Colloids, Amphiphiles and Liquid Crystals. Chichester: John Wiley; 2000

[3] Oroguchi T, Ikeguchi M. MD–SAXS method with nonspherical boundaries. Chemical Physics Letters. 2012;**541**:117-121

[4] Sander B, Golas MM. Visualization of bionanostructures using transmission electron microscopical techniques. Microscopy Research and Technique. 2011;**74**(7):642-663

[5] Henderson R. Overview and future of single particle electron cryomicroscopy. Archives of Biochemistry and Biophysics. 2015;**581**(Suppl C):19-24

[6] Schröder RR. Advances in electron microscopy: A qualitative view of instrumentation development for macromolecular imaging and tomography. Archives of Biochemistry and Biophysics. 2015;**581**:25-38

[7] Oliveira CLP. Investigating macromolecular complexes in solution by small angle X-ray scattering. In: Current Trends in X-Ray Crystallography. Rijeka: InTech; 2011

[8] Alves C, Pedersen JS, Oliveira CLP. Modelling of high-symmetry nanoscale particles by small-angle scattering. Journal of Applied Crystallography. 2014;**47**(1):84-94

[9] Oliveira CLP, Monteiro AM, Neto AMF. Structural modifications and clustering of low-density lipoproteins in solution induced by heating. Brazilian Journal of Physics. 2014; **44**(6):753-764

[10] Oliveira CLP, Santos PR, Monteiro AM, Neto AMF. Effect of oxidation on the structure of human low- and high-density lipoproteins. Biophysical Journal. 2014;**106**(12):2595-2605

[11] Cohen T. Quantum Mechanics. New York: John Wiley & Sons; 1977

[12] Guinier A, Fournet G. Small Angle Scattering of X-Rays. New York: Wiley; 1955

[13] Glatter O, Kratky O. Small-Angle X-Ray Scattering. London: Academic Press; 1982

[14] Feigin LA, Svergun DI. Structure Analysis by Small-Angle X-Ray and Neutron Scattering. New York: Plenum Press; 1987. pp. 25-55

[15] Alves C, Pedersen JS, Oliveira CLP. Calculation of two-dimensional scattering patterns for oriented systems. Journal of Applied Crystallography. 2017;**50**(3):840-850

[16] Pedersen Jan S. Analysis of small-angle scattering data from colloids and polymer solutions: Modeling and least-squares fitting. Advances in Colloid and Interface Science. 1997; **70**:171-210

[17] Mertens HDT, Svergun DI. Structural characterization of proteins and complexes using small-angle X-ray solution scattering. Journal of Structural Biology. 2010;**172**(1):128-141

[18] Petoukhov MV, Svergun DI. Applications of small-angle X-ray scattering to biomacromolecular solutions. The International Journal of Biochemistry & Cell Biology. 2013;**45**(2): 429-437

[19] Putnam CD, Hammel M, Hura GL, Tainer JA. X-ray solution scattering (SAXS) combined with crystallography and computation: Defining accurate macromolecular structures, conformations and assemblies in solution. Quarterly Reviews of Biophysics. 2007;**40**(03)

[20] Li T, Senesi AJ, Lee B. Small angle X-ray scattering for nanoparticle research. Chemical Reviews. 2016;**116**(18):11128-11180

[21] Langridge R, Barnett MP, Mann AF. Calculation of the fourier transform of a helical molecule. Journal of Molecular Biology. 1960;**2**(1):63-64

[22] Langridge R et al. The molecular configuration of deoxyribonucleic acid: II. Molecular models and their fourier transforms. Journal of Molecular Biology. 1960;**2**(1):38-IN12

[23] Porod G. General theory. In: Glatter O, Kratky O, editors. Small-Angle X-Ray Scattering. London: Academic Press; 1982. pp. 17-52

[24] Lindner P, Zemb T, editors. Neutrons, X-Rays and Light - Scattering Methods Applied to Soft Condensed Matter. The Netherlands: Elsevier; 2002

[25] McAlister BC, Grady BP. Simulation of small-angle X-ray scattering from single-particle systems. Journal of Applied Crystallography. 1998;**31**(4):594-599

[26] McAlister BC, Grady BP. The use of Monte-Carlo simulations to calculate small-angle scattering patterns. Macromolecular Symposia. 2002;**190**(1):117-130

[27] Petoukhov MV et al. New developments in the *ATSAS* program package for small-angle scattering data analysis. Journal of Applied Crystallography. 2012;**45**(2):342-350

[28] Fritz-Popovski G. Two-dimensional indirect Fourier transformation for evaluation of small-angle scattering data of oriented samples. Journal of Applied Crystallography. 2013; **46**(5):1447-1454

[29] Fritz-Popovski G. Interpretation of two-dimensional real-space functions obtained from small-angle scattering data of oriented microstructures. Journal of Applied Crystallography. 2015;**48**(1):44-51

[30] Pedersen Jan S. Chapter 16. Modeling of small-angle scattering data. In: Lindner P, Zemb T, editors. Neutrons, X- Rays and Light: Scattering Methods Applied to Soft Condensed Matter. Amsterdam: Elsevier; 2002. pp. 391-420

[31] Kohlbrecher J, Bressler I. Software package SASfit for fitting small-angle scattering curves. 2006. Available: https://kur.web.psi.ch/sans1/SANSSoft/sasfit.html

[32] Fedorov BA, Ptitsyn OB, Voronin LA. X-ray diffuse scattering of globular protein solutions: Consideration of the solvent influence. FEBS Letters. 1972;**28**(2):188-190

[33] Fedorov BA, Ptitsyn OB, Voronin LA. X-ray diffuse scattering by proteins in solution. Consideration of solvent influence. Journal of Applied Crystallography. 1974;**7**(2):181-186

[34] Fedorov BA, Denesyuk AI. Sperm whale myoglobin structure in solution differs from its structure in crystal by a shift of the 'hairpin'Gh. FEBS Letters. 1978;**88**(1):114-117

[35] Ninio J, Luzzati V, Yaniv M. Comparative small-angle X-ray scattering studies on unacylated, acylated and cross-linked *Escherichia coli* transfer RNA. Journal of Molecular Biology. 1972;**71**(2):217-229

[36] Svergun DI, Stuhrmann HB. New developments in direct shape determination from small-angle scattering. 1. Theory and model calculations. Acta Crystallographica, Section A: Foundations of Crystallography. 1991;**47**(6):736-744

[37] Virtanen JJ, Makowski L, Sosnick TR, Freed KF. Modeling the hydration layer around proteins: HyPred. Biophysical Journal. 2010;**99**(5):1611-1619

[38] Virtanen JJ, Makowski L, Sosnick TR, Freed KF. Modeling the hydration layer around proteins: Applications to small- and wide-angle X-ray scattering. Biophysical Journal. 2011;**101**(8):2061-2069

[39] Nguyen HT, Pabit SA, Meisburger SP, Pollack L, Case DA. Accurate small and wide angle x-ray scattering profiles from atomic models of proteins and nucleic acids. The Journal of Chemical Physics. 2014;**141**(22):22D508

[40] Nguyen HT, Pabit SA, Pollack L, Case DA. Extracting water and ion distributions from solution x-ray scattering experiments. The Journal of Chemical Physics. Jun 2016;**144**(21): 214105

[41] Svergun D, Barberato C, Koch MHJ. *CRYSOL* – A program to evaluate X-ray solution scattering of biological macromolecules from atomic coordinates. Journal of Applied Crystallography. 1995;**28**(6):768-773

[42] Grishaev A, Guo L, Irving T, Bax A. Improved fitting of solution X-ray scattering data to macromolecular structures and structural ensembles by explicit water modeling. Journal of the American Chemical Society. 2010;**132**(44):15484-15486

[43] Poitevin F, Orland H, Doniach S, Koehl P, Delarue M. AquaSAXS: A web server for computation and fitting of SAXS profiles with non-uniformally hydrated atomic models. Nucleic Acids Research. 2011;**39**(suppl 2):W184-W189

[44] Debye P. Molecular-weight determination by light scattering. The Journal of Physical Chemistry. 1947;**51**(1), http://pubs.acs.org/doi/pdf/10.1021/j150451a00218-32

[45] Oliveira CLP et al. Structure of nanoscale truncated octahedral DNA cages: Variation of single-stranded linker regions and influence on assembly yields. ACS Nano. 2010;**4**(3):1367-1376

[46] Andersen FF et al. Assembly and structural analysis of a covalently closed nano-scale DNA cage. Nucleic Acids Research. 2008;**36**(4):1113-1119

[47] Berman HM et al. The Protein Data Bank. Nucleic Acids Research. 2000;**28**(1):235-242

[48] Harrison SC. Structure of tomato bushy stunt virus: I. The spherically averaged electron density. Journal of Molecular Biology. 1969;**42**(3):457IN1465-464IN2483

[49] Stuhrmann HB. Interpretation of small-angle scattering functions of dilute solutions and gases. A representation of the structures related to a one-particle scattering function. Acta Crystallogr. Sect. A. 1970;**26**(3):297-306

[50] Svergun DI, Volkov VV, Kozin MB, Stuhrmann HB. New developments in direct shape determination from small-angle scattering. 2. Uniqueness. Acta Crystallographica, Section A: Foundations of Crystallography. 1996;**52**(3):419-426

[51] Arndt MHL, de Oliveira CLP, Régis WCB, Torriani IL, Santoro MM. Small angle x-ray scattering of the hemoglobin from Biomphalaria glabrata. Biopolymers. 2003;**69**(4):470-479

[52] Svergun DI. Restoring low resolution structure of biological macromolecules from solution scattering using simulated annealing. Biophysical Journal. 1999;**76**(6):2879-2886

[53] Kirkpatrick S, Gelatt CD Jr, Vecchi MP. Optimization by simulated annealing. Science. 1983;**220**(4598):671-680

[54] Chacón P, Morán F, Díaz JF, Pantos E, Andreu JM. Low-resolution structures of proteins in solution retrieved from X-ray scattering with a genetic algorithm. Biophysical Journal. 1998;**74**(6):2760-2775

[55] Chacón P, Díaz JF, Morán F, Andreu JM. Reconstruction of protein form with X-ray solution scattering and a genetic algorithm. Journal of Molecular Biology. 2000;**299**(5):1289-1302

[56] Walther D, Cohen FE, Doniach S. Reconstruction of low-resolution three-dimensional density maps from one-dimensional small-angle X-ray solution scattering data for biomolecules. Journal of Applied Crystallography. 2000;**33**(2):350-363

[57] Svergun DI. Determination of the regularization parameter in indirect-transform methods using perceptual criteria. Journal of Applied Crystallography. 1992;**25**(4):495-503

[58] Svergun DI, Petoukhov MV, Koch MH. Determination of domain structure of proteins from X-ray solution scattering. Biophysical Journal. 2001;**80**(6):2946

[59] Konarev PV, Volkov VV, Sokolova AV, Koch MHJ, Svergun DI. PRIMUS: A windows PC-based system for small-angle scattering data analysis. Journal of Applied Crystallography. 2003;**36**(5):1277-1282

[60] Franke D, Svergun DI. DAMMIF, a program for rapid ab-initio shape determination in small-angle scattering. Journal of Applied Crystallography. 2009;**42**(2):342-346

[61] Svergun DI, Richard S, Koch MHJ, Sayers Z, Kuprin S, Zaccai G. Protein hydration in solution: Experimental observation by x-ray and neutron scattering. Proceedings of the National Academy of Sciences. 1998;**95**(5):2267-2272

[62] Konarev PV, Petoukhov MV, Svergun DI. MASSHA – A graphics system for rigid-body modelling of macromolecular complexes against solution scattering data. Journal of Applied Crystallography. 2001;**34**(4):527-532

[63] Volkov VV, Svergun DI. Uniqueness of *ab initio* shape determination in small-angle scattering. Journal of Applied Crystallography. 2003;**36**(3):860-864

[64] Petoukhov MV, Svergun DI. Global rigid body modeling of macromolecular complexes against small-angle scattering data. Biophysical Journal. 2005;**89**(2):1237-1250

[65] Petoukhov MV et al. New developments in the ATSAS program package for small-angle scattering data analysis. Journal of Applied Crystallography. 2012;**45**(2):342-350

[66] Jacques DA, Guss JM, Svergun DI, Trewhella J. Publication guidelines for structural modelling of small-angle scattering data from biomolecules in solution. Acta Crystallographica Section D: Biological Crystallography. 2012;**68**(6):620-626

[67] Trewhella J et al. Report of the wwPDB small-angle scattering task force: Data requirements for biomolecular modeling and the PDB. Structure. 2013;**21**(6):875-881

[68] Kikhney AG, Svergun DI. A practical guide to small angle X-ray scattering (SAXS) of flexible and intrinsically disordered proteins. FEBS Letters. 2015;**589**(19PartA):2570-2577

[69] Franke D et al. ATSAS 2.8: A comprehensive data analysis suite for small-angle scattering from macromolecular solutions. Journal of Applied Crystallography. 2017;**50**(4):1212-1225

[70] Glatter O. X-ray small angle scattering of molecules composed of subunits. Acta Physica Austriaca. 1972;**36**:307-315

[71] Pantos E, Bordas J. Supercomputer simulation of small angle X-ray scattering, electron micrographs and X-ray diffraction patterns of macromolecular structures. Pure and Applied Chemistry. 1994;**66**(1):77-82

[72] Hansen S. Calculation of small-angle scattering profiles using Monte Carlo simulation. Journal of Applied Crystallography. 1990;**23**(4):344-346

[73] Pedersen JS et al. Structure of immune stimulating complex matrices and immune stimulating complexes in suspension determined by small-angle X-ray scattering. Biophysical Journal. 2012;**102**(10):2372-2380

[74] Schmidt-Rohr K. Simulation of small-angle scattering curves by numerical Fourier transformation. Journal of Applied Crystallography. 2007;**40**(1):16-25

[75] Olds DP, Duxbury PM. Efficient algorithms for calculating small-angle scattering from large model structures. Journal of Applied Crystallography. 2014;**47**(3):1077-1086

[76] Schmidt-Rohr K, Chen Q. Parallel cylindrical water nanochannels in Nafion fuel-cell membranes. Nature Materials. 2008;**7**(1):75-83

[77] Sjöberg B. Small-angle scattering from collections of interacting hard ellipsoids of revolution studied by Monte Carlo simulations and other methods of statistical thermodynamics. Journal of Applied Crystallography. 1999;**32**(5):917-923

[78] Kam Z. Determination of macromolecular structure in solution by spatial correlation of scattering fluctuations. Macromolecules. 1977;**10**(5):927-934

[79] Saldin DK et al. Beyond small-angle x-ray scattering: Exploiting angular correlations. Physical Review B. 2010;**81**(17)

[80] Saldin DK et al. Structure of a single particle from scattering by many particles randomly oriented about an axis: Toward structure solution without crystallization? New Journal of Physics;**12**(3):035014, 2010

Section 2

X-Ray Diffraction Analysis

Chapter 2

X-Ray Diffraction Analysis of Structural Changes Induced by Overrolling

Oskar Beer

Additional information is available at the end of the chapter

http://dx.doi.org/10.5772/intechopen.74251

Abstract

A new method of X-ray diffraction analysis to evaluate structural changes in rolling element bearing components is demonstrated. The basics of residual stress measurement by X-ray diffraction based on the $\sin^2\psi$ method are explained. Microstructural analysis is performed on bearing components after rig testing and after use in field. The results shown in this chapter are mostly derived from rolling element bearing applications in aero engines. First it is shown how an estimation of a rolling contact fatigue life can be derived from microstructural analysis. Second it will be shown that surface near induced residual stresses can improve rolling contact fatigue life. Finally it will be demonstrated that basic results from rig testing can be transferred to use in field.

Keywords: X-ray diffraction, structural changes, residual stress, rolling contact fatigue life, stress limit

1. Introduction

X-ray analysis enables the detection of structural changes in materials. By performing this kind of analysis on rolling element bearing components after use structural changes caused by the overrolling process can be analyzed. This analysis enables the possibility to get data for stress limits and to compare rig testing results and field experience. In many cases it is more effective to get such data by X-ray analysis than by statistic evaluation of rig testing. A comparison of data from rig testing with data from field experience is often only possible by X-ray analysis of parts coming from use in field. Several work has already be done in this field [1–5]. The method of analysis presented here also uses data from residual stress analysis, especially the full width at half maximum value, also called peak width for the estimation of life data for

rolling element bearings. The focus of evaluation here is mainly on mainshaft bearing applications in aero engines, therefore the material analyzed is the high speed steel M50. The basics of X-ray analysis of residual stresses are presented, then some information about stresses due to rolling contact is given. Several samples of X-ray analysis performed on parts from rig testing and from use in field show the possibilities of this kind of evaluation.

2. X-ray residual stress analysis

2.1. Principle of measurement

By elastic deformation the distances within the unit cells of a crystallic material become smaller in case of compressive stress or larger in case of tensile stress respectively. **Figure 1** shows schematically the variation of a lattice distance due to tensile stresses. The positions of the atoms are represented by small circles. The distance d′ of the atoms due to the tensile stress σ is larger than the distance d of the unloaded condition. The elongation of the lattice in direction of the stress σ is accompanied by a shortening perpendicular to the direction of σ. The ratio between the elongation in direction of the stress σ and the shortening perpendicular is called Poisson's ratio ν. The elongation due to elastic loading by the tension σ can be calculated by Hook's law with the modulus of elasticity E as characteristic parameter. X-ray diffraction analysis makes possible the determination of variations in interatomic distances and hence enables the calculation of macroscopic stresses.

2.2. Bragg's law

When a beam of X-ray falls on a specimen, the X-ray photons interact with the electrons of the target and scattering occurs. X-ray diffraction analysis is based on the scattering with no energy loss, the scattered radiation will retain the same wavelength as the incident beam. When two or more waves trains propagate at the same location into the same direction, they interfere which is a kind of superposition of one wave upon the other. If wave trains are in phase, they add to another, if they are exactly out of phase, they annihilate each other. **Figure 2** illustrates the geometric condition of reinforcement on a schematic lattice. Scattering points are the atoms of the

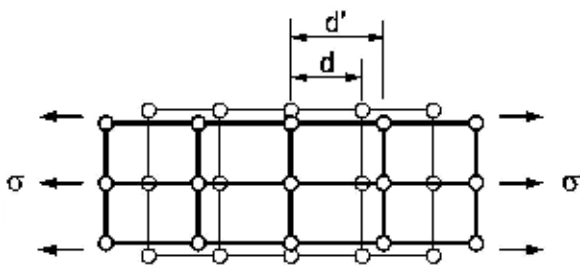

Figure 1. Shift of the unit cell dimensions due to a tensile stress σ. d: lattice plane distance without stress; and d′: lattice plane distance due to the stress σ.

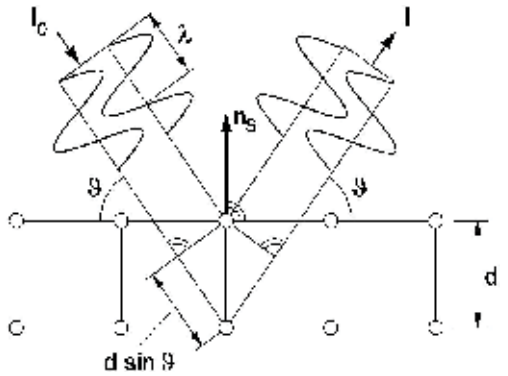

Figure 2. Diffraction of x-radiation at a crystal lattice.

lattice. Reinforcement will occur, when the difference in the path lengths of the two interfering waves is equal to an integer multiple of the wavelength, the equation for this is given in Eq. (1) which is the statement of Bragg's law.

Bragg's law for constructive interference:

$$n\lambda = 2d\sin\vartheta \ (n = 1, 2, 3\ldots) \tag{1}$$

Only if the incident angle ϑ fits to Bragg's law, diffraction maybe observed at the emergent beam at the same angel ϑ.

By known wavelength λ and measured diffraction angle ϑ the lattice plane distance d can be calculated:

$$d = n\lambda/2\sin\vartheta \tag{2}$$

The intensity of the diffracted beam around the Bragg angle ϑ_B is shown schematically in **Figure 3**. The peak can be characterized by the peak position ϑ_B and the peak width. The peak position correlates width the lattice plane distance d and by this with the material stress σ. The peak width correlates with the density of dislocations beside other microstructural properties and therefore it is correlated to a certain extent with the strength of the material.

2.3. The ψ angle

The penetration depth of the X-radiation typically used for diffraction analysis is only a few micrometers in most metals. This means that only the surface near region is used for the measurement. Material stresses act predominately parallel to the surface of a part, especially close to a surface no stress component perpendicular to this surface is possible (due to the balance of forces). The determination of material stresses by a variation of lattice distance d according to **Figure 2** takes place perpendicular to the surface. This means, that lattice planes easy to be measured (parallel to the surface) have no direct correlation to the acting material

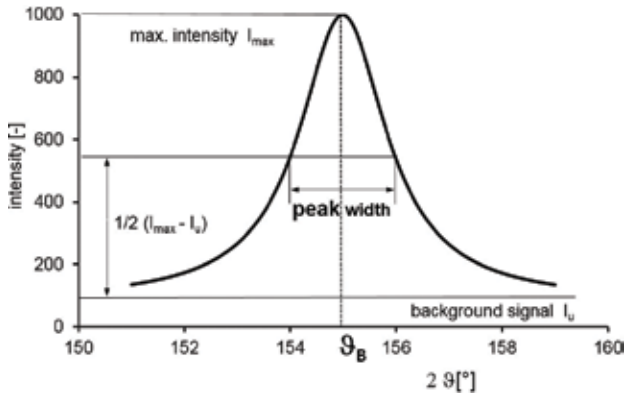

Figure 3. Intensity of the diffracted beam around the Bragg angle ϑ_B (schematic).

stress, diffraction from lattice planes having the highest correlation to the acting stress (perpendicular to the surface) are absorbed and cannot be measured. The way to overcome this problem is a measurement at an inclination angle, called tilt angel ψ to the normal of the plane of the surface. **Figure 4** shows this principle.

A measurement according to **Figure 4** is only possible when in the irradiated area enough lattice planes perpendicular to the adjusted tilt angle ψ are available. Metallic materials, especially construction materials, consist of an arrangement of small crystals, called grains. The orientation of these grains is in many cases randomly distributed (if there is a preferred orientation of the grains due to the manufacturing process, called texture, e.g. due to intensive rolling, the method described here is not applicable at this fashion). **Figure 5** shows schematic grains with different orientation at the surface of a part. The average size of the grains in many construction materials is small compared to the irradiated area (e.g. the average grain size in steels is app. 60–20 μm, the diameter of the irradiated area is typically 1–4 mm), therefore enough grains with an orientation according to the adjusted tilt angle are available and a measurement is possible.

The principle of an experimental setup for performing residual stress measurements is shown in **Figure 6a**, a photograph of the device used for the following investigations is shown in **Figure 6b**. The X-rays used in diffraction analysis are produced by an evacuated tube. The target (anode) is water cooled, the target material for residual stress analysis at steel is typically chromium. The radiation emitted consists of a continuous spectrum, called bremsstrahlung, with some superimposed narrow spikes. One of these spikes, the Kα spike, is used for diffraction analysis, all the other radiation is absorbed by filters (for the use of Eq. (2) a nearly monochromatic X-radiation is necessary). For detection of the irradiated X-rays today mainly position sensitive solid state detectors are used. These detectors allow the analysis of the complete diffracted beam around the Bragg angle.

The direction of the normal and shear stress components measured by ψ-variation is perpendicular to the rotation axis for the ψ-tilts.

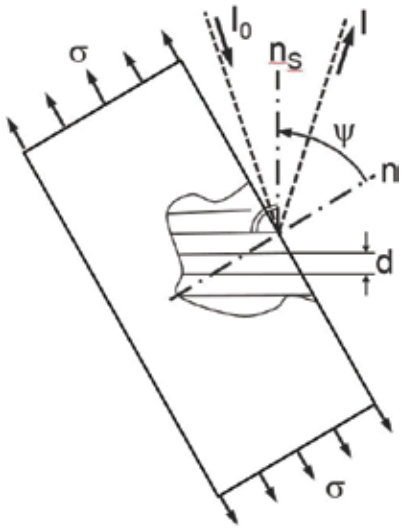

Figure 4. Diffraction at a tilt angle ψ.

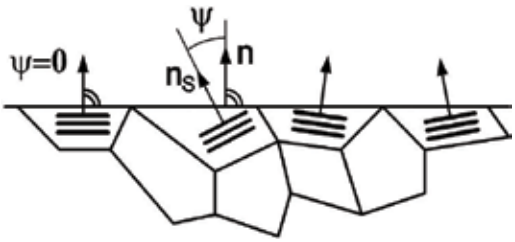

Figure 5. Orientation of grains at the surface (schematic). n: normal to the surface, n_s: normal to the lattice, and ψ: tilt angle.

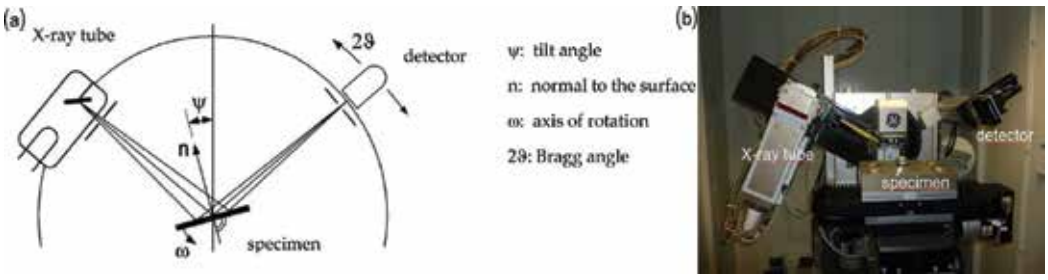

Figure 6. a: Schematic of an X-ray diffractometer, ω mode. b: Photograph of the device used for X-ray stress analysis.

2.4. The $\sin^2\psi$ chart

The following relation applies to describe the dependence of the lattice plane distances from the acting stress [6, 7]:

$$(d\psi - d_0)/d_0 = \tfrac{1}{2} s_2 \left[\sigma \sin^2 \psi + \tau \sin 2\psi\right] + c \tag{3}$$

where $d\psi$ is the lattice plane distances of the planes with a tilt angle ψ in relation to the surface, d_0 is the lattice plane distances of a stress free crystal, s_2 is the X-ray elastic constant, material property to be known, σ is the normal stress acting parallel to the surface, and τ is the shear stress.

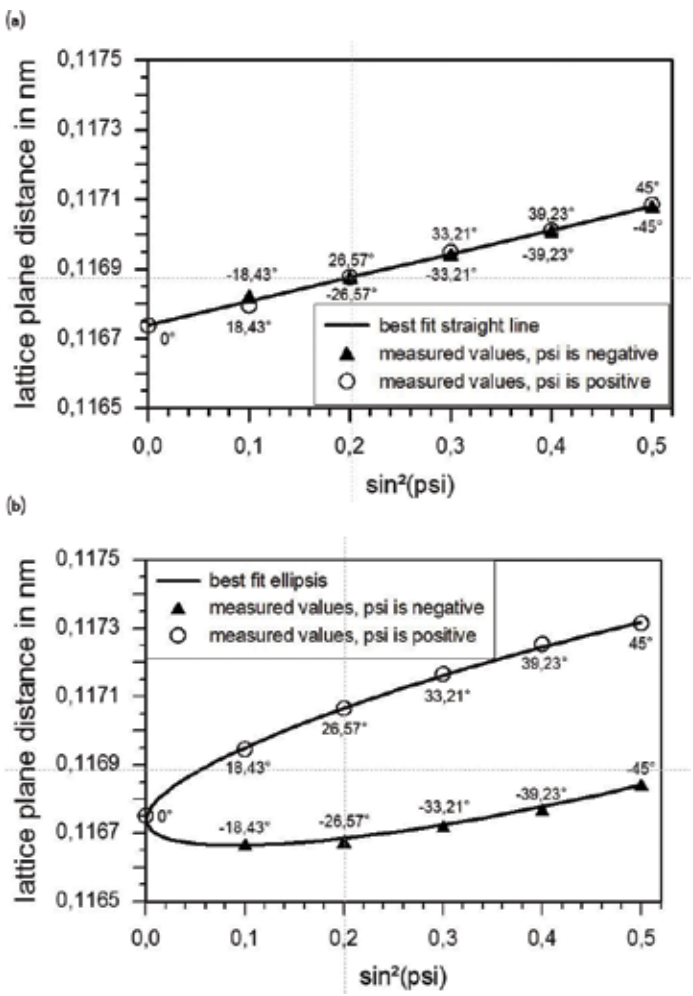

Figure 7. a: Example of a $\sin^2\psi$ chart without shear stress: straight line. b: Example of a $\sin^2\psi$ chart with shear stress: ellipsis.

There are three unknown values in the $\sin^2\psi$ formula (3), σ, τ and c. These values could be determined by the measurements of the lattice plane distances $d\psi$ for three different ψ-angles. For a lower uncertainty in the final values, the measurement of the lattice plane distances $d\psi$ should be performed for more than three ψ-angles. If no shear stress t is present, the $\sin^2\psi$ formula (3) requires a straight line as a result of a plot of $d\psi$ against $\sin^2\psi$. If the shear stress τ is not negligible, the term $\tau \sin 2\psi$ transforms the straight line into an ellipsis. The slope of its big main axis is determined by σ, its width by τ. **Figure 7a** shows a $\sin^2\psi$ chart with no shear stress present, **Figure 7b** shows a $\sin^2\psi$ chart for a steel where shear stress is present.

3. Stresses due to rolling contact

The contact stresses arising from the contact between two elastic solids can be calculated by the Hertzian equations (with some assumptions: pure elastic material, dimensions of the solids are big compared with the contact area, frictionless contact, these assumptions are nearly fulfilled in rolling element bearing applications). In case of microstructural changes, the material behavior in the zone of maximum stress is not purely elastic. Nevertheless the Hertzian analysis can still be used to rationalize the observed damage accumulation. The stress field inside the bodies is characterized by a triaxial stress state, comprising the three principal stress components. In order to express the material stress beneath the contact zone and allow a comparison with the uniaxial yield strength, an equivalent stress can be calculated. The von Mises equivalent stress σ_{vgl} agrees best with many experimental results and is mostly used. An alternative is to calculate the maximum shear stress 2τ according to Tresca, which leads to results nearly the same or equivalent to von Mises equivalent stress (depending on the

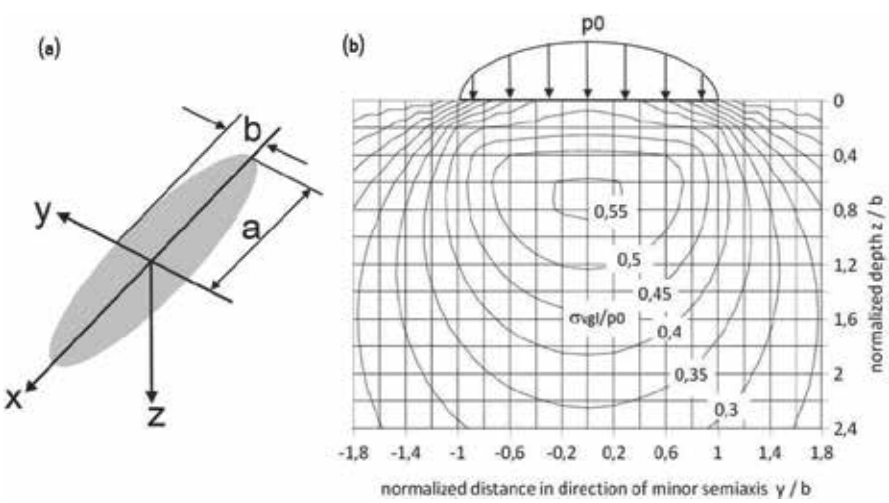

Figure 8. (a) Contact surface typical for a ball bearing, ellipsis, a: major semiaxis, b: minor semiaxis, y direction of overrolling. (b) Contour plot of the von Mises equivalent stress σ_{vgl} under the contact surface along the direction of overrolling (y direction according to **Figure 8a**). The stress is normalized to the Hertzian pressure p0, distances are normalized to the minor semiaxis of the contact ellipse b (a/b = 20).

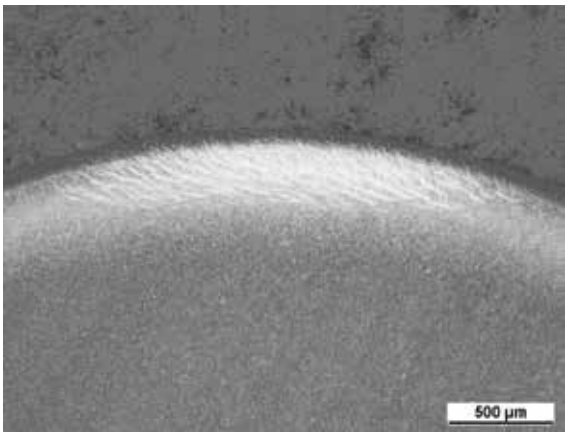

Figure 9. Micrograph showing microstructural changes below the surface of a ball (section perpendicular to the rolling track), after testing for 100 h at a Hertzian pressure of 3000 MPa, many white bands ("white ribbons") are visible in the subsurface zone.

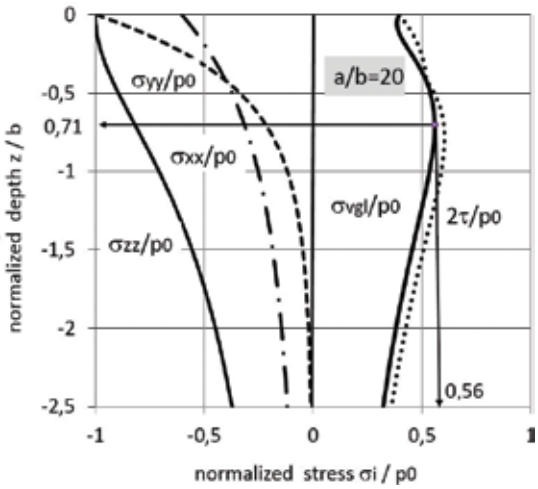

Figure 10. Stress distribution below the raceway surface (away from the axis of contact) for a Hertzian contact (a/b = 20), stress parameters are normalized to the Hertzian pressure p0, the depth coordinate is normalized to the minor semiaxis of the contact ellipse b.

stress components) and is simpler in several applications (in case of a principal state of stress). **Figure 8a** shows a contact area typical for a contact in a ball bearing, **Figure 8b** a contour plot of the von Mises equivalent stress σ_{vgl} under the contact surface. The maximum pressure occurs in the center of the contact surface and is called Hertzian pressure. Below the contact area a complex stress state develops. A micrograph taken in the subsurface zone of a bearing ring after intensive overrolling shows microstructural changes, "white ribbons" in about the depth of the maximum equivalent stress, see **Figure 9**. **Figure 10** shows the course of the three principal stress components along the axis of contact (z-axis) and the von Mises equivalent stress together with the max. shear stress (Tresca) for an elongated contact ellipse [2].

Away from the axis of contact the principal axes of the stress at a given position are not longer aligned with the sample coordinate system.

4. Analysis of bearing components

4.1. Details of the performed analysis

All analysis of the investigated components was done by position dispersive, monochromatic X-ray diffraction using a conventional diffractometer operated in iso-inclination. More sophisticated methods like the use of a synchrotron as X-ray source or the application of neutron diffraction was not necessary to achieve the pursued goals. The X-ray diffraction analysis was performed according to common standards (EN 13925, EN15305), Cr-Kα radiation was used, LPA (**L**orenz/**P**olarization/**A**bsorption)-correction was applied. The stress component parallel to the surface in direction of overrolling was measured. Depth profiles of residual stress and peak width were measured by a successive local electro chemical removal of surface layers. This procedure is necessary because the penetration depth of the Cr-Kα radiation in steel is only a few micrometers and a mechanical removal of material would create additional residual stresses. No correction of the stress redistribution due to the material removal was applied.

Comprehensive work in this field has already be done [1–5], here the evaluation is based more on the peak width and the analyzed material is the high speed steel M50.

4.2. Bearing steel M50

M50 is a high speed steel which exhibits high hardness and high compressive strength also at elevated temperatures. The chemical composition is (weight-percent):

$$0.85\,\%\,\mathrm{C}/4.1\,\%\,\mathrm{Cr}/4.2\,\%\,\mathrm{Mo}/1\,\%\,\mathrm{V}.$$

M50 is widely used for aeroengine bearings (VIMVAR quality corresponding to AMS 6491). The heat treating comprises an austenitizing at a temperature of approximately 1100°C, quenching in salt or in pressurized nitrogen gas and tempered several times at temperature of around 540°C. The resulting hardness is typically in the range of 61–64 HRC, the content of retained austenite is usually below 3%.

4.3. Experimental setup

The test rig used for performing overrolling tests is the so called "single ball test rig". The principle of this test rig is shown in **Figure 11**. The test component is a ball which rolls between two rings having curved races. One ring is driven by a motor, the load is applied by a hydraulic system. The ball is fixed by a retainer such that the overrolling of the ball occurs along in one rolling track. The lubrication of the contact zone is done by oil jets, the inlet temperature is approximately 140°C in order to be comparable to an application in an aeroengine, more details about rig testing can be found in [2].

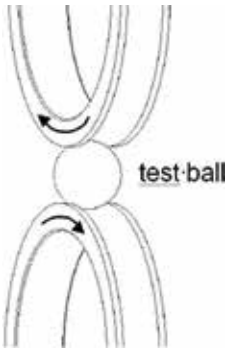

Figure 11. Schematic of the single ball test rig, ball diameter is app. 20–40 mm, speed of the rings is typically 7500 min^{-1}, race diameter of the rings is 175 mm.

The procedure to get structural changes is to run the single ball test rig with several balls for a fixed time (before visible failure) at different levels of pressure. Afterwards an X-ray based evaluation is performed on these balls. **Figure 12** shows calculated profiles of von Mises equivalent stress under the contact surface of a ball in the single ball test rig.

4.4. Evaluation results

4.4.1. Estimation of rolling contact fatigue life

Single ball rig tests were performed at different contact pressures. **Figure 13a** and **b** shows depth profiles of measured residual stress and peak width (see also **Figure 3**) after 100 h test run at Hertzian pressures of 1900 and 3000 MPa, respectively. The difference in peak width before and after testing, called "integral change in peak width," can be used to obtain an estimate of the endurance limit, see also [2, 3]. **Figure 14** shows the principle of the evaluation of the integral change in peak width. By plotting the so evaluated integral change in peak width

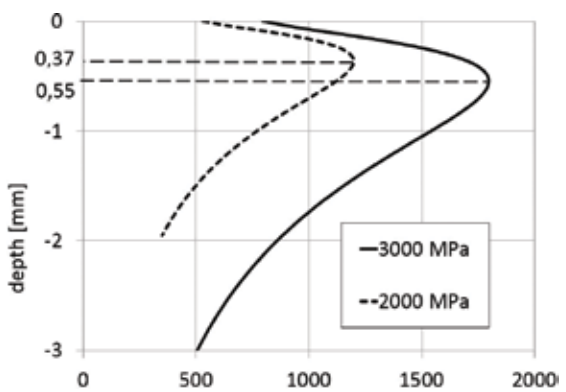

Figure 12. Calculated von Mises equivalent stress below the raceway for a ball (diameter 41 mm) in the single ball test rig at two different levels of Hertzian pressure.

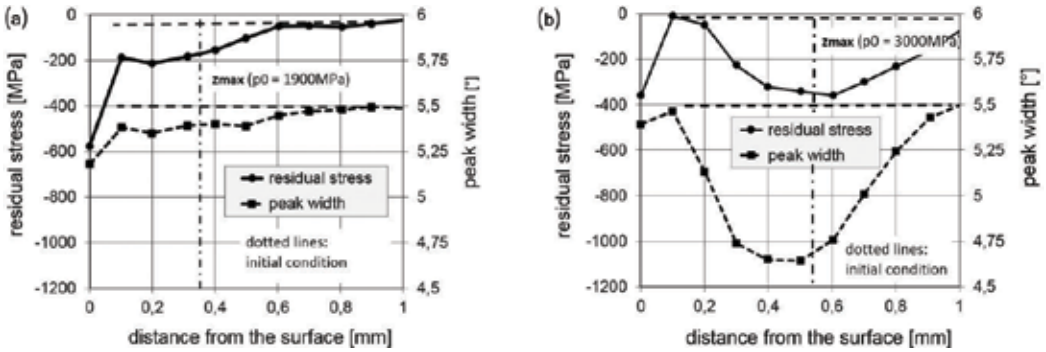

Figure 13. Measured distribution of residual stress (solid line) and peak width (dotted line) below the raceway surface in M50 balls after 100 h test in single ball test rig at a Hertzian pressure of (a) 1900 MPa and (b) 3000 MPa respectively, at an oil temperature of 140°C, zmax: calculated depth of maximum von Mises equivalent stress.

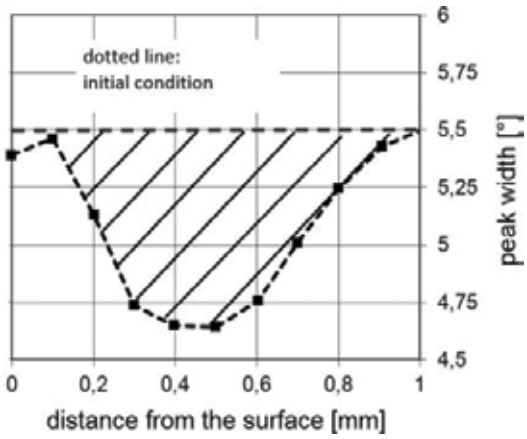

Figure 14. Distribution of peak width according to **Figure 13b**. Hatched area: integral change in peak width.

versus the applied maximum Hertzian contact pressures and fitting a straight line through these data points, an endurance limit in terms of an allowed maximum contact pressure (below which no fatigue damage will be accumulated) can be determined by extrapolation to zero peak width change. This procedure is shown in **Figure 15**. The estimated value for the endurance limit S0 of app. 1800 MPa according to **Figure 15** agrees well with experience from comprehensive testing and field experience.

4.4.2. Influence of residual compressive stresses

Residual stresses caused by heat treating (e.g. case hardening, nitriding) or mechanical induced residual stresses mostly act in directions parallel to the surface (in x- and y-direction according to the set of axis used here, see also **Figure 8a**). Residual stresses in the material will be superimposed on the stresses induced by the contact between the rolling element and the raceway surface and may then influence the equivalent stress [2, 3, 8, 9]. As residual stresses

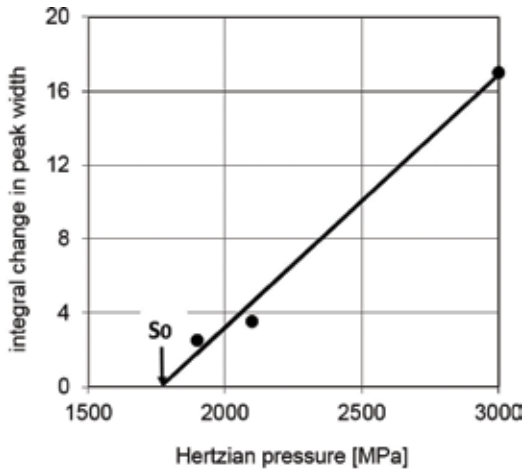

Figure 15. Estimation of an endurance limit S0 in terms of an allowed maximum contact pressure (oil temperature 140°C), y-axis arbitrary units.

typically act predominately in x- and y-direction, a shift of the principal stresses in x- and y-direction occurs whereas the principal stress in z-direction is less influenced. Compressive residual stresses (in a certain range) typically result in a reduction of the equivalent stress level. **Figure 16** shows the influence of compressive residual stresses on the von Mises equivalent stress in case of an axisymmetric contact (ball-ball).

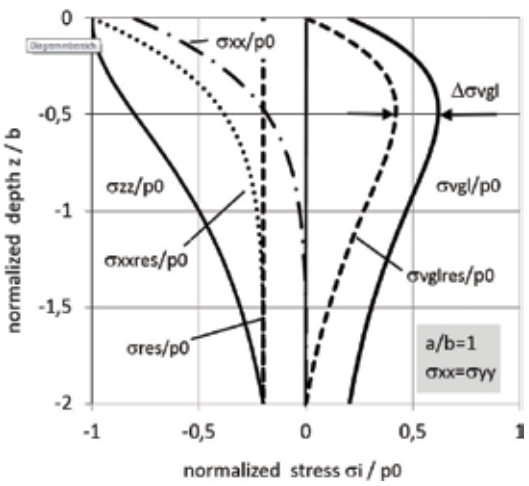

Figure 16. Stress distribution below the raceway surface for a Hertzian point contact (a/b = 1, $\sigma_{xx} = \sigma_{yy}$) without (solid curves) and with (dashed curves) compressive residual stress (the residual stress profile σ_{res} is here simplified as a constant compressive). The von Mises equivalent stress without consideration of residual stress (solid line) and with consideration of residual stress (dashed line), resulting in a reduction in the equivalent stress $\Delta\sigma_{vgl}$. The stress parameters are normalized to the Hertzian pressure p0, the depth coordinate is normalized to the radius of the contact surface.

By performing the single ball test procedure with balls which were tumbled (also called scoured in case of an intensive tumbling) after heat treating to induce compressive residual stresses the beneficial influence of compressive residual stresses on the overrolling performance can be shown. **Figure 17** shows residual stress and peak width distributions of tumbled balls after testing at two different contact pressure levels. **Figure 18** shows the evaluation of the endurance limit for both tumbled and not tumbled balls. As can be seen, the evaluated endurance limit of the tumbled balls is significantly higher.

The evaluation of several balls exposed to rolling contact fatigue in rig testing showed the following results:

- There seems to exist a stress (or maximum contact pressure) limit for the development of structural changes.
- Compressive residual stresses can raise the stress limit for the development of structural changes.

In rig testing the test conditions are well known and typically are maintained constant during the whole test run. In field use the operating conditions (load, temperature, etc.) are mostly not constant and not fully known. An evaluation of bearings after field use by X-ray methods offers the possibility to compare the test results with results from use in the field.

4.5. Field experience

Unlike as many rig tests, the load during a flight cycle is not constant. Maximum load typically occurs during take-off, while during normal flight conditions the load generally is lower. Also, different and variable temperatures and vibrations occur during the different parts of the flight cycle. Therefore, structural changes after field use are the result of a more or less periodic and complex load history. Since the full load history of an aero engine bearing as well

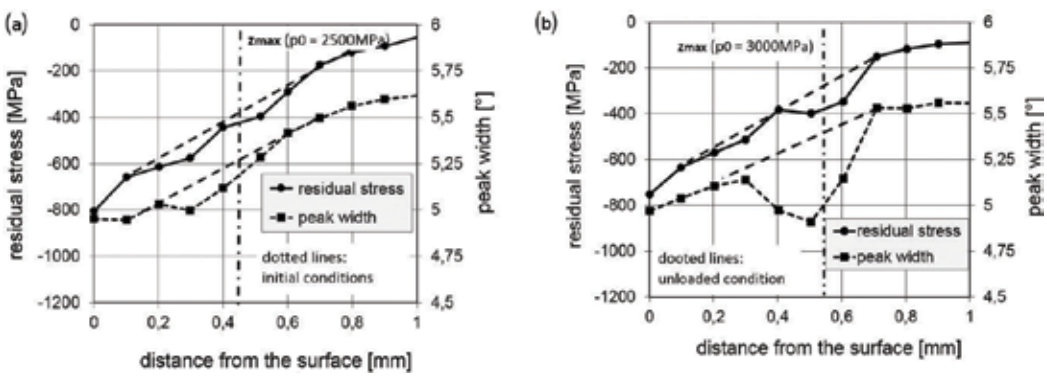

Figure 17. Measured distribution of residual stress and peak width below the raceway surface in tumbled M50 balls after 100 h test in the single ball test rig at the Hertzian pressure: (a) 2500 MPa and (b) 3000 MPa respectively, at an oil temperature of 140°C, z_{max}: calculated depth of maximum equivalent stress.

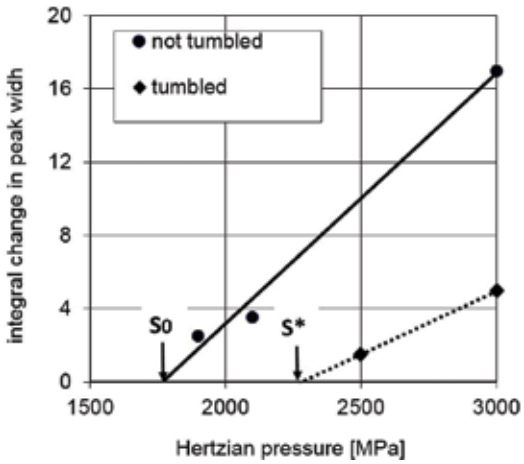

Figure 18. Estimated endurance limits in terms of allowed maximum contact pressure (below which no fatigue damage will be accumulated). S* of tumbled and S_0 of not tumbled M50 balls (oil in temp. 140°C), y axis arbitrary units.

as its temperature, vibration level etc. are not fully known, a direct comparison between rig test results and evaluation results from use in the field is not fully possible. However, based on the techniques discussed here, general experiences from laboratory testing can still, as will be shown, successfully transferred to field applications, see also [2].

The following evaluation results are taken from bearing parts after considerably time in field use. Two measures are handled for the characterization of the duration in field use:

TSN: Time Since New [h]

CSN: Cycles Since New.

4.5.1. Limit stress for structural changes

In order to check whether a stress limit for microstructural changes exists for field use, an inner ring of an used roller bearing was investigated. The stress acting in the subsurface zone of roller bearings are generally lower than for ball bearings, therefore even after long time in field use, no structural changes are expected. **Figure 19** shows measured distribution of residual stress and peak width for the inner ring of a roller bearing from a V2500 aero engine after TSN 37,380 h. This bearing did not show any indication of spalling or wear. The X-ray evaluation shows no indication of any structural changes. Although the stress history is not fully known in detail, the absence of any indication of structural changes suggests, that also in field use for a long time, a limit stress for structural changes may exist.

4.5.2. Influence of residual stress

A possibility of investigation the influence of residual stresses on the formation of structural changes in field use was given in case of a ball bearing of a GE90 aero engine with a TSN of 20,492 h. The rings and the balls were made from M50, while the balls were additionally tumbled to induce compressive residual stresses. This bearing showed slight indications of

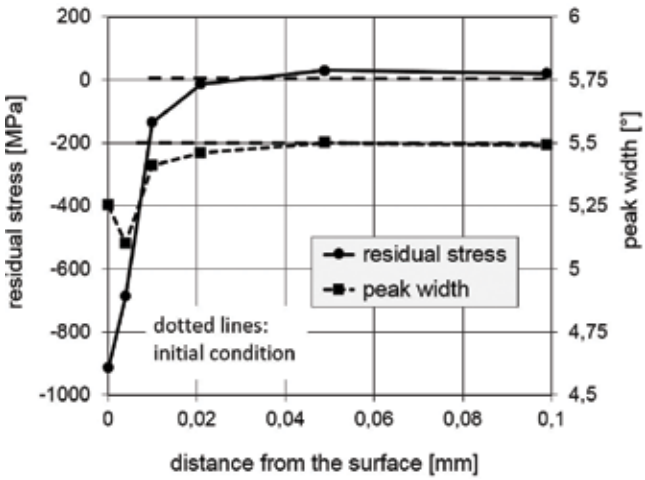

Figure 19. Measured distribution of residual stress and peak width below the raceway surface in a roller bearing inner ring, TSN 37,380 h, there are no indications of structural changes (only the typical peaks close to the surface due to hard machining), the Hertzian pressure is assumed to be at most 1200 MPa.

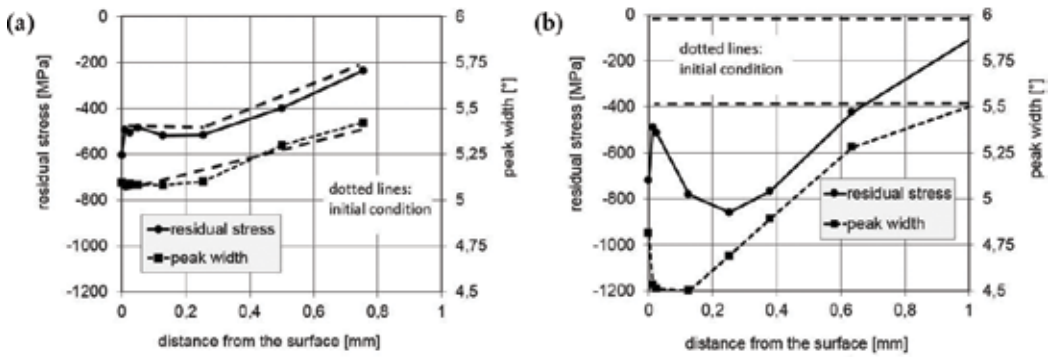

Figure 20. Measured distribution of residual stress and peak with from components of a GE90 aero engine, TSN 20,492 h (a) below the surface in a ball (tumbled) showing no indication of structural changes and (b) below the raceway surface in an inner ring, showing marked difference between the initial condition and the condition after use in field, suggesting considerably microstructural changes. Hertzian pressure assumed to be maximum 2000 MPa.

spalling on all components and was therefore taken out of service. **Figure 20** shows the measured distribution of residual stress and peak width versus the depth below the raceways, for a ball and an inner ring, respectively.

5. Conclusions

The microstructural evaluation of bearing components after rig testing shows that induced surface-near compressive residual stresses can improve the rolling contact fatigue life. It is further possible to derive approximate values for the endurance limit using X-ray based

microstructural analysis. A comparison of microstructural evaluation results on components taken from engine bearings after use in the field with results from parts after rig testing shows, that basic causes and effects are similar in both cases. These results therefore provide a confirmation that results from rig testing can be used for bearing design also in demanding applications.

Acknowledgements

The author acknowledges the technical support of Dr. Böhmer.

Author details

Oskar Beer

Address all correspondence to: oskar.beer@schaeffler.com

FAG Aerospace GmbH and Co. KG, Schweinfurt, Germany

References

[1] Voskamp AP. Material response to rolling contact loading. ASME Journal of Tribology. 1985;**107**(3):359-367

[2] Beer O. Structural changes induced by rolling contact fatigue – Results from rig testing and field experience. HTM Journal of Heat Treatment and Materials. 2017;**72**(4):205-214

[3] Beer O, Fella J. Untersuchung struktureller Veränderungen durch Überrollbeanspruchung mittels röntgenografischer Methoden. HTM Journal of Heat Treatment and Materials. 2015;**70**(3):142-149

[4] Böhmer HJ, Hirsch Th. Der Einsatz von Eigenspannungsmessungen zur Bewertung des Wälzermüdungsverhaltens von Werkstoffen. In: Bauteilversagen durch Mikrodefekte, DVM-Bericht 518; 1998. pp. 27-47

[5] Gegner J, Nierlich W. Comparison of microstructural changes and X-ray diffraction peak width decrease during rolling contact fatigue in martensitic microstructures. In: Advances in Rolling Contact Fatigue Strength Testing and Related Substitute Technologies, STP 1548 Int. Conshohocken, PA, USA; 2012. pp. 303-328

[6] Noyan IC, Cohen JB. Residual Stress Measurement by Diffraction and Interpretation. Berlin: Springer; 1987

[7] Böhmer, internal communication

[8] Hill DA, Ashelby DW. The influence of residual stresses on contact load bearing capacity. Wear. 1982;**75**(2):221-240

[9] Broszeit E, Adelmann J, Zwirlein O. Einfluß von Eigenspannungen auf die Werkstoffanstrengung in wälzbeanspruchten Bauteilen. Materialwissenschaft und Werkstofftechnik. 1985;**16**(1):19-24

Section 3

Cavitation Behavior of Semi-Crystalline Polymers

Chapter 3

Cavitation Behavior of Semi-Crystalline Polymers during Uniaxial Stretching Studied by Synchrotron Small-Angle X-Ray Scattering

Baobao Chang, Konrad Schneider,
Ines Kuehnert and Gert Heinrich

Additional information is available at the end of the chapter

http://dx.doi.org/10.5772/intechopen.74224

Abstract

Cavitation appears in many semi-crystalline polymers when they are subjected to uniaxial stretching above their glass transition temperatures. Generally, the formation of voids is influenced by the morphology of semi-crystalline polymers, including their lamellae thickness, lamellae orientation, as well as the arrangement of the amorphous phase. Upon stretching, the size of the voids changes as a function of the local strain. Synchrotron small-angle X-ray scattering (SAXS) can be used as a powerful method to *in-situ* monitor the evolution of voids with high time and spatial resolution. In this chapter, recent reports about the cavitation behavior of semi-crystalline polymers studied by SAXS are reviewed. Afterwards, the theoretical background related to the SAXS technique is introduced. Lastly, some exemplary results about the cavitation behavior of microinjection-molded isotactic-polypropylene, studied by synchrotron SAXS measurements, are presented.

Keywords: cavitation, synchrotron, small-angle X-ray scattering, semi-crystalline polymer, stretching

1. Introduction

1.1. Cavitation behavior of semi-crystalline polymers

Cavitation behavior has been found in many semi-crystalline polymers, including isotactic-polypropylene (iPP) [1, 2], polyethylene (PE) [3, 4], poly(1-butene) (P1B) [5], and so on, when these polymers are stretched above their glass transition temperature. Stress whitening can be

regarded as the scattering of visible light by voids detected by naked eye. As the size of the voids exceeds 0.5 μm, most of the visible light shed on the sample will be scattered, transforming the sample from a transparent one to an opaque one. In the pioneering work of Peterlin [6] randomly distributed cracks were found in the neck region of PP specimen. In addition, the formation of small cracks was reported to arise earlier than macroscopic stress whitening [7, 8].

Cavitation behavior can be influenced by many factors, which can be divided into two groups. One of them is attributed to experimental factors such as stretching temperature and stretching speed. Generally, a lower stretching temperature or a larger stretching speed favors voids formation. Another group is attributed to the microstructure of polymers, for instance the crystal form, the thickness of lamellae, as well as the state of the amorphous phase. By polymer processing, various microstructures and morphologies can be created in the product depending on the individual processing conditions they used [9–11]. Therefore, understanding the influence of microstructure on the void formation will be helpful for the establishment of a structure-properties relationship.

1.2. Role of crystal form

iPP is a kind of polymorphic polymer owning four crystal forms: monoclinic α-iPP, hexagonal β-iPP, triclinic γ-iPP, and smectic form [12]. By applying shear flow or adding special nucleating agents, the crystal form of iPP could be adjusted. Aboulfaraj et al. [13] found that under tensile deformation, α-iPP spherulites exhibited a brittle failure. The cavitation appeared at boundaries of spherulites or at their equatorial regions perpendicular to the tensile direction. However, no cavitation could be observed in the sample comprising β-iPP spherulites. The β-iPP spherulites were deformed plastically up to large deformation. Chu [14] prepared iPP films containing more than 90% β-iPP. These samples crystallized under either isothermal or nonisothermal conditions. The porosity of the stretched films, which is caused by the existence of voids, increased with the drawing ratio. The voids observed by scanning electron microscopy (SEM) were elongated along the stretching direction and confined by the fibrillary structures. The formation of numerous voids was proposed to be caused by the volume contraction of the film. β-iPP belongs to a metastable phase, so a β-α phase transformation was induced during deformation. The density of α-iPP is higher than that of β-iPP. Therefore, a volume contraction can led to a formation of voids in the sample. The more pronounced stress whitening behavior in β-iPP rich iPP samples was also confirmed by Pawlak [2].

1.3. Role of lamellae arrangement

In α-iPP, the lamellae are arranged in a unique "cross-hatched" structure, where daughter lamellae grow 80° inclined to the mother lamellae [15]. Nitta et al. [16] observed that cavitation appears earlier if there were more tangential lamellae in a single spherulite. Otherwise, Pawlak found that the reduction of tangential daughter lamellae would advance the formation of voids [17].

1.4. Role of crystallinity

By annealing, Na et al. prepared PP samples with crystallinity ranging from 48 to 56%. The cavitation behavior of the sample was investigated by measuring the volume increase. The results show that in annealed samples, the cavitation behavior was significantly intensified due to the increased stress concentration sites [18]. Boger et al. [19] examined the cavitation behavior of metallocene PP with crystallinity ranging from 0 to 62%. For the sample with crystallinity higher than 36%, the scattering signal originated from a fibrillary structure showed up on the SAXS pattern as the elongation ratio is larger than 3. In case of β-iPP, Bai et al. [20] found that annealing could advance the appearance of cavitation.

1.5. Role of the thickness of lamellae

Generally, thinner lamellae would prevent the formation of voids. The reason responsible for that was proposed by Seguela et al. [21]: a thinner lamella bears larger tie chain density, which transfers the load to lamellae in a better way and leads to the plastic deformation of lamellae instead to cavitation in the amorphous phase.

1.6. Role of lamellae orientation

The cavitation behavior of oriented β-iPP was investigated by Bao et al. [22]. The samples were cut from extruded sheets, and the deformation direction was parallel to the orientation of β-iPP lamellae. Their results proved that at temperatures lower than 110°C, the orientation of β-iPP remains almost unchanged during deformation, and void forms before fragmentation and reorientation of β-iPP. As the deformation temperature risen to 130 and 140°C, β-iPP reorients gradually upon stretching, and the size of voids decreases because at high stretching temperature less β crystal fragmentation takes place.

1.7. Role of the state of amorphous phase

Pawlak and Galeski [23] compared the cavitation behavior of PP with similar crystallinity and crystal thickness but different molecular masses of 400 and 250 kg/mol. They found that the samples having lower molecular weight showed stronger cavitation as a result of reduced number of entanglements in the amorphous phase. Rozanski and Galeski extracted the additives in the amorphous phase by critical CO_2 and also by a mixture of nonsolvents. They found that purified PP exhibited more intense cavitation than pristine PP [24]. The intensified cavitation process in the purified samples was caused by the change in free volume by eliminating low molecular weight fractions and soluble additives in the amorphous phase, indicating that the nucleation of voids is not heterogeneous. In their later work, they proved that only partial filling of the free volume pores of the amorphous phase with low molecular weight modifier leads to a decrease of intensity or complete elimination of the cavitation phenomenon. [25]

2. Synchrotron X-ray scattering

2.1. X-ray and its sources

X-ray, a kind of electromagnetic radiation (see **Figure 1**), is also named as Röntgen radiation, after Wilhelm Röntgen, who discovered X-rays in 1895 [26]. Since that time, X-rays have been employed in the field of materials science as a nondestructive analytical technique. Traditionally, X-rays are produced by X-ray tubes. In X-ray tubes, the electrons emitted from cathode wire are accelerated by an electric voltage before they hit the target. The wavelength of X-rays produced by X-ray tubes depends on the target material. For instance, the characteristic wavelength of the X-ray produced is 1.54 Å by Cu target and 1.79 Å by Co target.

The main disadvantages of X-ray tubes are its low energy, broad focus (around 2 × 12 mm), and long exposure time (around 60 s) [27]. In the mid-1970s, the limitation of X-ray tube was overcome by the establishment of the synchrotron radiation, where electrons orbiting in a magnetic field loose energy continually in the form of electromagnetic radiation. The first synchrotron light source was the Stanford Synchrotron Radiation Laboratory (SSRL) build in 1977 [28]. Nowadays, a few synchrotron radiations have been set up all over the world, and the synchrotron radiation has been developed into the third generation, to name a few, European Synchrotron Radiation Facility (ESRF) in France [3], Deutsches Elektronen-Synchrotron (DESY) in Germany (see **Figure 2**) [29], Shanghai Synchrotron Radiation Facility (SSRF) [30] in China, and so on. At PETRA III of DESY, the size of the X-ray beam could reach a few micrometers and the exposure time could be milliseconds. The high spatial and temporal resolution of synchrotron X-ray source enables to perform *in-situ* X-ray scattering measurements combining, for example, thermal/mechanical environment.

As X-rays interact with an object, they can be absorbed or scattered. For the scattering of X-rays by a single free electron, assuming elastic scattering the wavelength of the scattered wave is the same with that of the incident one. The relation between the scattered wave $\boldsymbol{E_2}$ and incident wave $\boldsymbol{E_1}$ is given as follows:

$$\boldsymbol{E_2} = \boldsymbol{E_1}\frac{{e_0}^2}{m_0 c^2 r}\exp\left(-i\boldsymbol{q}r\right) \tag{1}$$

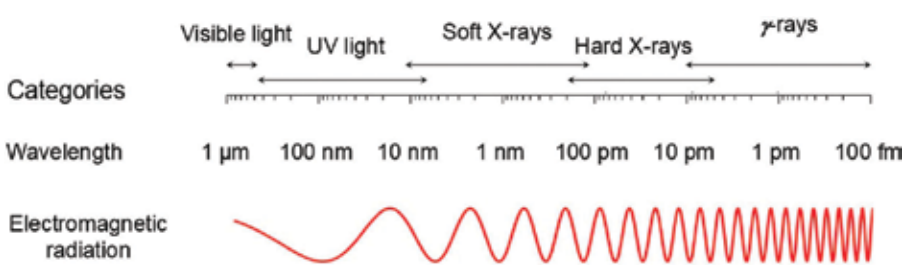

Figure 1. Categories of electromagnetic radiation.

Figure 2. PETRA III, the third generation of synchrotron light source at DESY Germany [31].

where $\frac{e_0{}^2}{m_0c^2} = 3.54 \times 10^{-4}$ Å [32]. $\boldsymbol{r}$ is the position of the electron and $\boldsymbol{q}$ is the scattering vector, the magnitude of the scattering vector is

$$q = \frac{4\pi}{\lambda} sin\theta \tag{2}$$

θ is the scattering angle. In addition to $\boldsymbol{q}$, another scattering vector $\boldsymbol{s}$ is used in the field of scattering,

$$\boldsymbol{q} = 2\pi \boldsymbol{s} \tag{3}$$

The interference of all the scattered X-ray waves gives the final scattering signal. The efficiency of the scattering process could be described by the differential scattering cross-section ($d\sigma/d\Omega$) [32], which is given by

$$\left(\frac{d\sigma}{d\Omega}\right) = \frac{I_m}{\Phi_0 \Delta\Omega} = \frac{|\boldsymbol{E_2}|^2}{|\boldsymbol{E_1}|^2} R^2 \tag{4}$$

Φ_0 defines the strength of the incident beam, I_m is measured scattering intensity, that is, the number of scattered photons recorded per second by the detector, $\Delta\Omega$ is the solid angle, and the distance between the object and the detector is R.

Depending on the distance between the object and the detector, the scattering experiments can be divided into four subareas, which are wide-angle X-ray scattering (WAXS) containing the classical X-ray diffraction, middle angle X-ray scattering (MAXS) covering the characteristic scattering of liquid-crystalline structure and rigid-rod polymers, small-angle X-ray scattering (SAXS) comprising the typical nanostructure in semi-crystalline polymers and thermoplastic elastomers, and ultra-small-angle X-ray scattering (USAXS) extending the detection range to micrometer scale [27]. Considering the scope of this chapter, SAXS will be emphasized especially. SAXS comprises the scattering angle range $2\theta < 2^{\circ}$. With the help of SAXS, structures with the size of 1–500 nm can be detected, covering the size of lamellae and small voids.

2.2. Small-angle X-ray scattering

In SAXS measurement, X-rays detect the difference in electron density $\Delta\rho$, and the scattering intensity (I_m) is

$$I_m(\boldsymbol{s}) = \Delta\rho^2 V_p^2 |\mathcal{F}(\boldsymbol{s})|^2 \tag{5}$$

$\mathcal{F}(\boldsymbol{s})$ is the form factor and V_p is the volume fraction of particles (for instance, the lamella in semi-crystalline polymers, the voids during deformation, and "shish" structure during shear induced crystallization). R_g is the radius of gyration of the particle. In the extremely small scattering angle range, $sR_g \to 0$,

$$\mathcal{F}(s) \approx 1 - \frac{s^2 R_g^2}{10} \tag{6}$$

The detailed deduction of Eq. (6) can be found elsewhere [33]. The initial intensity decay is approximated by Guinier approximation

$$I_m(s) \approx \Delta\rho^2 V_p^2 \left[1 - \frac{s^2 R_g^2}{10}\right]^2 \approx \Delta\rho^2 V_p^2 \left[1 - \frac{s^2 R_g^2}{5}\right] \approx I_m(0)\exp\left(-4\pi^2 R_g^2 s^2\right) \tag{7}$$

The absolute scattering intensity Q which is independent of the shape of the scatters,

$$Q = \iiint_{s\to 0}^{s\to\infty} I(\boldsymbol{s}) d\boldsymbol{s} \propto \Delta\rho^2 V_p (1 - V_p) \tag{8}$$

The pattern of SAXS measurement depends on the microstructure of the material. For the material with the periodically stacked structure (lamellae in semi-crystalline polymers) inside, the pattern exhibits a homogeneous ring or "two-spots" depending on the orientation of lamellae. The long period L_p, which comprise a layer of crystalline phase and a layer of amorphous phase in the two-phase model, can be evaluated by Bragg's law,

$$L_p = {}^{2\pi}/_{q_{max}} \tag{9}$$

q_{max} represents the position of the scattering ring or spots on the pattern in the reciprocal space. For a material with an oriented elongated structure, for instance an extended chain structure (shishs induced by flow) as well as voids, a streak scattering will show up in the pattern. Considering a perfect orientation of the elongated structures, Ruland [34] described the integral breadth $B_{obs}(s_{12})$ of the elongated structure, measured as a function of s_{12}, as follows:

$$B_{obs}(s_{12}) = \int_{-\infty}^{\infty} I(s_{12}, s_3) ds_3 / I(s_{12}, 0) \tag{10}$$

The average length $\langle L \rangle$ of the elongated structure is the inverse of the integral breath:

$$B_{obs}(s_{12}) = \frac{1}{\langle L \rangle} \tag{11}$$

If misorientation has to be taken into account, the orientation distribution of the streak $g(\varphi)$ must be considered, then the apparent azimuthal integral breadth becomes

$$B_{obs}(s_{12}) = \frac{1}{I(s,\pi/2)}\int_{-\pi/2}^{\pi/2} I(s,\varphi)d\varphi \tag{12}$$

which depends on the width of the peak in the azimuthal direction. The evolution of B_{obs} as a function of s follows Eq. (13),

$$B_{obs}^2(s) = \frac{B_p^2}{s^2} + \frac{1}{s^2\langle L\rangle^2} + B_g^2, \tag{13}$$

if a Gaussian can describe the orientation distribution. B_p describes the inevitable instrumental broadening and B_g is the true integral breadth of the orientation distribution. If a Lorentzian fits the orientation distribution [27], one obtains

$$B_{ops} = \frac{B_p}{s} + \frac{1}{\langle L\rangle} + sB_g \tag{14}$$

3. *In-situ* synchrotron SAXS investigation about the cavitation behavior of microinjection-molded iPP

3.1. Microinjection molding

Microinjection molding is one of the most efficient methods for the large-scale production of thermoplastic polymer microparts. Depending on the area of interest, the definition of microparts comprises three categories [35]:

- parts processing a weight in the range of few milligrams,
- parts processing features where dimensions are in the micrometer range,
- parts exhibiting dimensional tolerances in the micrometer range but without dimensional limit.

In common injection molding, because of the flow and thermal field gradient, a "skin-core" structure can be found. In the skin layer, lamellae are oriented along the flow direction because of flow-induced crystallization. In the core layer, randomly distributed lamellae could be found due to the weak flow field. As to microinjection molding, the flow field in the cavity is quite strong due to the small cavity size especially for the first two cases. Therefore, a larger fraction of the skin layer is formed compared to common injection molding part [36], which means that a larger fraction of oriented structures exists in the microinjection-molded sample compared to the macroinjection-molded one.

In this chapter, the cavitation behavior of microinjection-molded iPP will be reported, studied by synchrotron SAXS, which serves as an exemplary result for the understanding of the topic in this chapter.

3.2. Experimental part

3.2.1. Materials and sample preparation

iPP used in this study was manufactured by Borealis (Linz, Austria) with the trademark of HD120MO. The weight average and number average molecular weights are 365 kg/mol and 67.6 kg/mol, and the melt flow index is 8 g/10 min (at 230°C and 2.16 kg). NJS (trade mark NJ-StarTR NU100), which is one kind of β-iPP nucleating agent, was kindly provided by Rika International Limited (Oldham, UK). NJS with a weight content of 0.3% was mixed with iPP granules by a twin screw extruder. Then the materials were microinjection molded with the following parameters: the barrel temperature is 280°C, the mold temperature is 25°C, and the injection molding speed is 25 cm^3/s.

3.2.2. In-situ *synchrotron X-ray scattering*

In-situ synchrotron SAXS measurements were carried out at the MiNaXS beamline at Deutsches Elektronen Synchrotron (DESY), Hamburg, Germany. The wavelength of the X-ray was 0.106917 nm. An exposure time of 0.1 s and a time interval for the individual measurements of 0.15 s were used to realize the high time resolution without burning the specimens by X-ray in the meantime. The patterns were recorded by a Pilatus 1 M detector (981 × 1043 pixels, pixel size 172 × 172 μm^2) with a detector distance of 4961 mm. Pattern preprocessing including masking and reconstruction of blind areas was performed by self-written subroutines on PV-Wave from Visual Numerics.

The uniaxial stretching was performed on a custom-made miniature tensile machine, as has been described elsewhere, for example, in Ref [37]. During measurements, to keep the X-ray beam at a fixed position on the specimen, both grips were moved simultaneously in opposite directions. The cross-head speed was 0.02 mm/s, and the stretching temperature was 75°C. The displacement during stretching was captured by a camera with a frame rate of 1 Hz. **Figure 3** presents a schematic and a photograph of the experiment. The schematic can be also found in Ref. [38]. Hencky strain [39] was used to measure the local strain where the X-ray beam passed the specimen,

$$\varepsilon_H = ln\frac{\Delta L + L_0}{L_0} \tag{15}$$

L_0 and ΔL are the initial length and displacement of the grid pattern painted on the specimen during stretching.

The true stress σ can be estimated by

$$\sigma = \frac{F}{A_0}\frac{\Delta L + L_0}{L_0} \tag{16}$$

F is the load, and A_0 is the initial cross-sectional area.

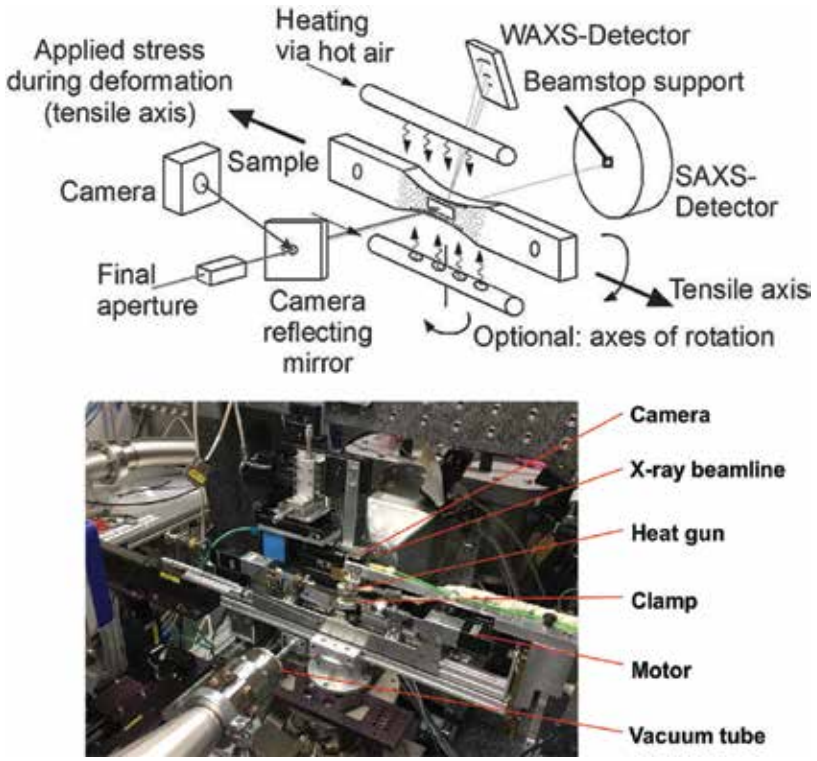

Figure 3. A schematic and a photograph of the experiment. The schematic can be also found in Ref. [38].

4. Results and discussion

4.1. Microstructure of the microinjection-molded iPP before stretching

The 2D-SAXS and 2D wide-angle X-ray scattering (WAXS) patterns of the microinjection-molded sample are given in **Figure 4**. In the 2D-SAXS pattern, two scattering spots can be found on the meridian, indicating the orientation of lamellae as a result of shear induced crystallization during the injection molding process. In the 2D-WAXS pattern, from inner to the outer side, a few reflexes could be observed, which are the (110), (300), (040), (130), and (041)/(111)/(−131) crystalline reflexes. Among these reflexes, (300) and (041) belong to β-iPP and the others are originated from α-iPP. The intensity of the reflexes is focused at a specified angle with respect to the flow direction. The azimuthal angle deviation is decided by the lattice plane. The intensity of (110) reflex could be found both on the equator and in the meridian. This is caused by the unique "cross-hatched" structure of α-iPP. In the "cross-hatched" structure, daughter lamellae grow on the mother lamellae with an angle of 80° [15]. Mother lamellae grow directly on the shear-induced nuclei, resulting in the orientation of mother lamellae in the flow direction. Consequently, the daughter lamellae are 80° inclined to the flow direction.

4.2. Representative 2D-SAXS patterns during stretching

The true stress-Hencky strain curves of pure iPP and iPP/NJS composites stretched at room temperature are provided in **Figure 5**. Obviously, the composite shows a higher true stress at the same Hencky strain. The higher true stress is caused by the nucleation effect of NJS on iPP. Although the crystallinity of pure iPP and iPP/NJS composite is nearly the same, a larger long period of iPP/NJS composite indicates that less imperfect lamellae exist in the nucleated sample.

Some representative 2D-SAXS patterns of pure iPP and iPP/NJS composite during stretching are shown in **Figure 6**. The stretching direction is vertical in **Figure 6**. Without deformation, the scattering on the meridian is spherulite-like for iPP/NJS composite and droplike for pure iPP, indicating a more homogeneous distribution of long periods in the composite. Upon stretching, the amorphous phases constrained by the lamellae are stretched along the loading direction, leading to a slight shift of the scattering position on the pattern [40]. In the center

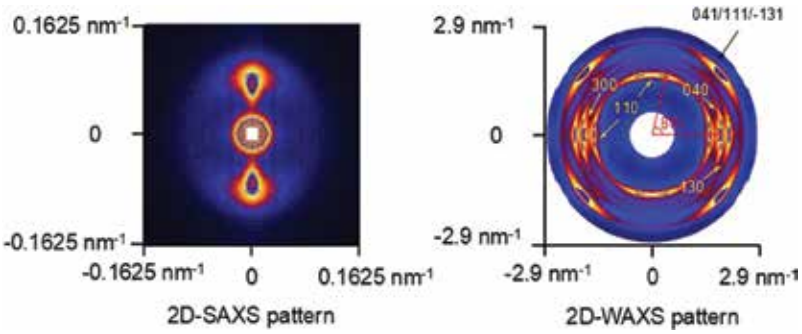

Figure 4. 2D small-angle (SAXS) and wide-angle (WAXS) X-ray scattering pattern of the microinjection-molded sample. The flow direction is vertical.

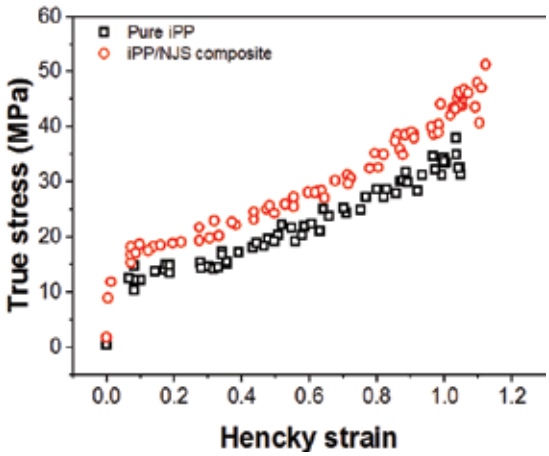

Figure 5. True stress-Hencky strain curves of pure iPP and iPP/NJS composite stretched under room temperature. The crosshead speed is 0.02 mm/s.

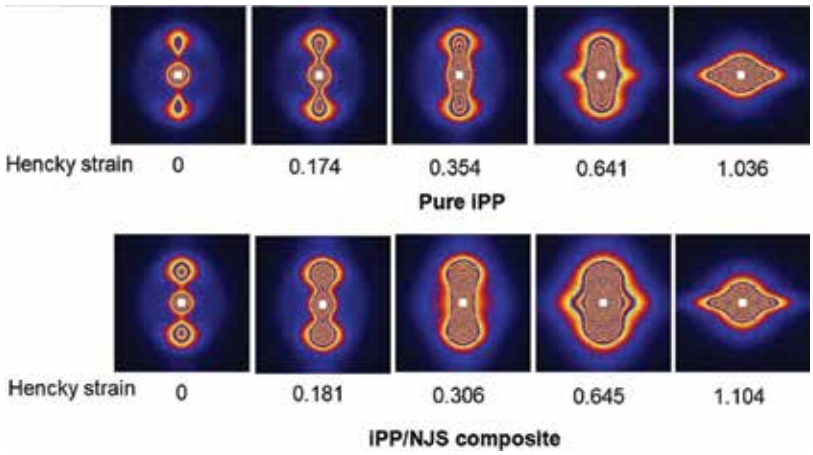

Figure 6. Representative 2D-SAXS of pure iPP and iPP/NJS composite during stretching. The stretching direction is vertical.

region of the pattern, a streak can be found, which is aligned along the meridian. The appearance of the streak is an indication of the void formation [1]. The direction of the streak with respect to the stretching direction suggests that the elongated voids are perpendicular to the streak direction. As the Hencky strain is further enlarged, the scattering of the streak continues to grow in the vertical direction, which is probably caused by the growth of the void. At an even larger strain ($\varepsilon_H = 0.641$), the scattering of lamellae is covered by the scattering of the void. In addition, a streak on the equator shows up indicating the formation of the second group of voids. This group of voids is aligned along the stretching direction. The formation of the second group of voids can be triggered by the first group of voids coalesces [41]. With the further increase of Hencky strain, the scattering grows mainly in the meridian, and the scattering intensity on the equator is narrowed.

4.3. The evolution of the scattering invariant

The scattering invariant (Q) of pure iPP and the iPP/NJS composite as a function of Hencky strain during stretching is given in **Figure 7**. As shown in Eq. (8), Q is proportional to $V_v(1 - V_v)$, where V_v is the volume fraction of the void. As V_v is smaller than 0.5, Q increases with V_v. However, if V_v is higher than 0.5, Q will decrease. In **Figure 7**, one can see that at the beginning, Q keeps unchanged until a Hencky strain of 0.1. As the Hencky strain exceeds 0.1, Q increases gradually indicating the formation of voids. As the Hencky strain is larger than 0.2, Q reaches an plateau for pure iPP, but continues to increase for iPP/NJS composite. The larger Q of the composite at the same strain means that more voids are formed in iPP/NJS composite. When the Hencky strain is larger than 0.6, a drastic drop of Q can be found for iPP/NJS composite. Two possible reasons can be proposed to be responsible for the decrease trend: the first one is that the size of the void exceeds the detection range of SAXS, and the second one is that the volume fraction of the voids is larger than 0.5 as discussed above. The first reason seems to be the dominant one.

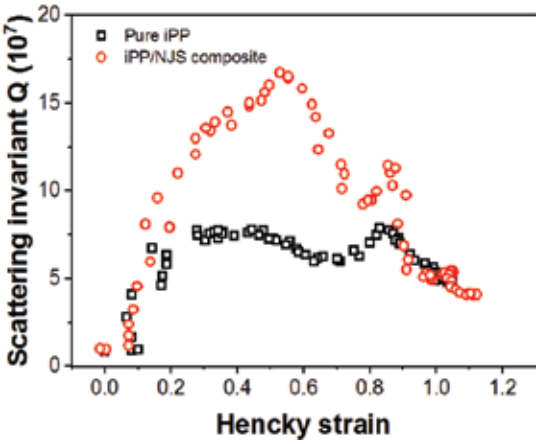

Figure 7. The scattering invariant (Q) of pure iPP and the iPP/NJS composite as a function of Hencky strain during stretching.

4.4. The evolution of the void size

As introduced in the first part, the size of the void can be evaluated by Ruland's streak method, if the shape of the void is regarded as cylindrical [27, 42]. To avoid the burning of the detector during the measurement, the center region of the beam is covered by a beamstop. To get information about the void size, the 2D-SAXS patterns in **Figure 6** are fitted by a sum of two 2D-Gaussian functions

$$I(s) = p_{v0} \exp\left(-p_{v1}s^2 - p_{v2}\cos\left(2\phi\right)s^2\right) + p_{m0} \exp\left(-p_{m1}s^2 - p_{m2}\cos\left(2\phi\right)s^2\right) \tag{17}$$

$$\phi = \arctan\frac{i}{j} \tag{18}$$

i and j define the position of the pixel in the pattern. The voids are described by the first Gaussian curve by parameters p_{v0}, p_{v1}, and p_{v2}. The scattering of the matrix is described by the second Gaussian curve. The fitting process is carried out by a self-written subroutine. A representative application of the fitting procedure is provided in **Figure 8**.

After the center fitting procedure, the void scattering can be extracted. The voids length along the stretching direction (L_h) and the voids length perpendicular to the stretching direction (L_v) can be calculated as

$$L_h = \sqrt{\frac{p_{v1} + p_{v2}}{\pi}} \tag{19}$$

$$L_v = \sqrt{\frac{p_{v1} - p_{v2}}{\pi}} \tag{20}$$

The evolution of the void size is presented in **Figure 9**. As the Hencky strain is smaller than 0.1, no voids can be detected. At Hencky strains beyond 0.1, voids show up as evidenced in

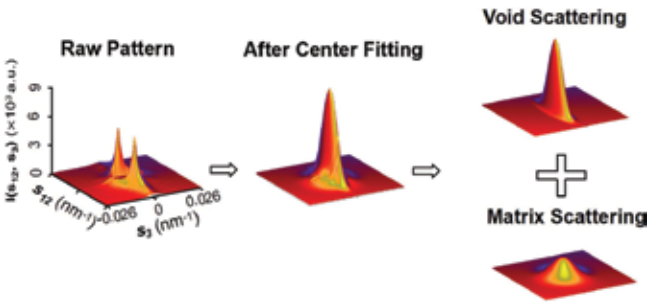

Figure 8. Center fitting and modeling of the 2D-SAXS pattern by the sum of the void scattering and the matrix scattering according to Guinier approximation. The stretching direction is along s_3.

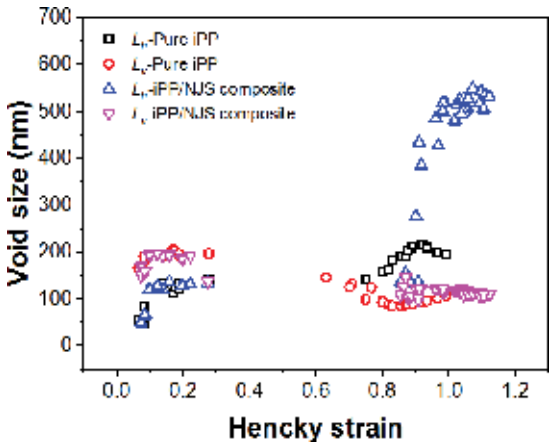

Figure 9. The plots of void length as a function of Hencky strain. L_h is the void size along the stretching direction and L_v is the void size perpendicular to the stretching direction.

Figures 6 and **9**. L_h is around 110 nm and L_v is 200 nm for pure iPP, indicating that the longitude of the void is perpendicular to the stretching direction. In addition, in this Hencky strain range, the void length is similar for pure iPP and iPP/NJS composite. This suggests that at the beginning of void formation, the addition of NJS has a negligible influence on the void size. As the Hencky strain is increased to 0.6, it can be found that L_v decreases gradually and L_h starts to increase, implying that the direction of the void is changed. Finally, the longitude direction of the voids changes from transversal to parallel direction with respect to the stretching direction. The change of the voids direction is caused by coalescence of small voids as well as the affine deformation of the voids. In this Hencky strain range, L_h of iPP/NJS composite reaches 550 nm, finally. This is much larger than that of pure iPP, which is only 200 nm. It should be pointed out that due to the growth as well as the direction change of the voids, no obvious streak signal can be found on the SAXS pattern in the Hencky strain of 0.3–0.6. So the voids size in this strain range is not provided.

5. Conclusions

In this chapter, recent reports about cavitation behavior in iPP during deformation are summarized. The influence of morphological factors including crystal form, crystallinity, lamellae thickness, state of the amorphous phase, and lamellae orientation is emphasized. In addition, the background related to the synchrotron SAXS is introduced. Finally, as exemplary results, the cavitation behavior of microinjection-molded iPP is presented. By center fitting, the blank region on the SAXS pattern is fitted by extrapolation. The size of the void is calculated by an approximation according to Guinier law. The result shows that upon stretching, the longitude of the void is aligned perpendicular to the stretching direction in the early stages of deformation and then transfers to the stretching direction. In the early stages, the addition of NJS has a negligible influence on the void size. The size of the voids is 210 nm perpendicular to the stretching direction and 110 nm along the stretching direction for both pure iPP and the iPP/NJS composites. However, in the late stages, the size of the voids along the stretching direction increases to 550 nm for the iPP/NJS composites. This is much larger than that of pure iPP, which is only 200 nm.

Acknowledgements

Baobao Chang would like to thank the grant by China Scholarship Council (CSC). The authors are grateful to DESY for beamtime within project I20140478. The authors acknowledge Prof. Stribeck at University of Hamburg for helpful discussions about the Ruland' Streak method and Matthieu Fischer (IPF Dresden) for the preparation of microinjection-molded samples.

Conflict of interest

The authors declare no conflict of interest.

Author details

Baobao Chang[1,2]*, Konrad Schneider[1], Ines Kuehnert[1] and Gert Heinrich[1,3]

*Address all correspondence to: chang@ipfdd.de

1 Leibniz-Institut für Polymerforschung Dresden e.V., Dresden, Germany

2 Institut für Werkstoffwissenschaft, Technische Universität Dresden, Dresden, Germany

3 Institut für Textilmaschinen und Textile Hochleistungswerkstofftechnik, Technische Universität Dresden, Dresden, Germany

References

[1] Rozanski A, Galeski A. Controlling cavitation of semi-crystalline polymers during tensile drawing. Macromolecules. 2011;**44**:7273-7287. DOI: 10.1021/ma201090z

[2] Pawlak A. Cavitation during deformation of polymers on the example of polypropylene. Journal of Applied Polymer Science. 2012;**125**:4177-4187. DOI: 10.1002/app.36565

[3] Schneider K, Trabelsi S, Zafeiropoulos NE, Davies R, Riekel C, Stamm M. The study of cavitation in HDPE using time resolved synchrotron X-ray scattering during tensile deformation. Macromolecular Symposia. 2006;**236**:241-248. DOI: 10.1002/masy.200650430

[4] Pawlak A, Galeski A. Cavitation during tensile drawing of annealed high density polyethylene. Polymer. 2010;**51**:5771-5779. DOI: 10.1016/j.polymer.2010.10.003

[5] Wang Y, Jiang Z, Fu L, Lu Y, Men Y. Lamellar thickness and stretching temperature dependency of cavitation in semi-crystalline polymers. PLoS ONE. 2014;**9e**:97234. DOI: 10.1371/journal.pone.0097234

[6] Peterlin A. Plastic deformation of polymers with fibrous structure. Colloid & Polymer Science. 1975;**253**:809-823. DOI: 10.1007/bf01452401

[7] Kambour RP. A review of crazing and fracture in thermoplastics. Journal of Polymer Science: Macromolecular Reviews. 1973:71-154. DOI: 10.1002/pol.1973.230070101

[8] Pawlak A, Galeski A, Rozanski A. Cavitation during deformation of semi-crystalline polymers. Progress in Polymer Science. 2014;**39**:921-958. DOI: 10.1016/j.progpolymsci.2013.10.007

[9] Pantani R, Coccorullo I, Speranza V, Titomanlio G. Modeling of morphology evolution in the injection molding process of thermoplastic polymers. Progress in Polymer Science. 2005;**30**:1185-1222. DOI: 10.1016/j.progpolymsci.2005.09.001

[10] Rhoades AM, Williams JL, Wonderling N, Androsch R, Guo J. Skin/core crystallinity of injection-molded poly (butylene terephthalate) as revealed by microfocus X-ray diffraction and fast scanning chip calorimetry. Journal of Thermal Analysis and Calorimetry. 2017;**127**:939-946. DOI: 10.1007/s10973-016-5793-z

[11] van Erp TB, Govaert LE, GWM P. Mechanical performance of injection-molded poly (propylene): Characterization and modeling. Macromolecular Materials and Engineering. 2013;**29**:8348-8358. DOI: 10.1002/mame.201200116

[12] Krache R, Benavente R, López-Majada JM, Pereña JM, Cerrada ML, Pérez E. Tailoring of the α-, β-, and γ-modification in isotactic polypropene and propene/ethene random copolymers. Macromolecules. 2007;**40**:6871-6878. DOI: 10.1021/ma0710636

[13] Aboulfaraj M, G'Sell C, Ulrich B, Dahoun A. In situ observation of the plastic deformation of polypropylene spherulites under uniaxial tension and simple shear in the scanning electron microscope. Polymer. 1995;**36**:731-742. DOI: 10.1016/0032-3861(95)93102-R

[14] Chu F, Yamaoka T, Ide H, Kimura Y. Microvoid formation process during the plastic deformation of β-form polypropylene. Polymer. 1994;**35**:3442-3448. DOI: 10.1016/0032-3861(94)90906-7

[15] Lotz B, Wittmann JC, Lovinger AJ. Structure and morphology of poly(propylenes): A molecular analysis. Polymer. 1996;**37**:4979-4992. DOI: 10.1016/0032-3861(96)00370-9

[16] Nitta KH, Takayanagi M. Direct observation of the deformation of isolated huge spherulites in isotactic polypropylene. Journal of Materials Science. 2003;**38**:4889-4894. DOI: 10.1023/B:JMSC.0000004410.56145.f1

[17] Pawlak A. Cavitation during tensile deformation of isothermally crystallized polypropylene and high-density polyethylene. Colloid & Polymer Science. 2013;**291**:773-787. DOI: 10.1007/s00396-012-2789-5

[18] Na B, Lv R. Effect of cavitation on the plastic deformation and failure of isotactic polypropylene. Journal of Applied Polymer Science. 2007;**105**:3274-3279. DOI: 10.1002/app.26594

[19] Boger A, Heise B, Troll C, Marti O, Rieger B. Orientation of the alpha- and gamma-modification of elastic polypropylene at uniaxial stretching. European Polymer Journal. 2007;**43**:3573-3586. DOI: 10.1016/j.eurpolymj.2007.05.031

[20] Bai H, Luo F, Zhou T, Deng H, Wang K, Fu Q. New insight on the annealing induced microstructural changes and their roles in the toughening of beta-form polypropylene. Polymer. 2011;**52**:2351-2360. DOI: 10.1016/j.polymer.2011.03.017

[21] Thomas C, Seguela R, Detrez F, Miri V, Vanmansart C. Plastic deformation of spherulitic semi-crystalline polymers: An in situ AFM study of polybutene under tensile drawing. Polymer. 2009;**50**:3714-3723. DOI: 10.1016/j.polymer.2009.06.023

[22] Bao RY, Ding ZT, Liu ZY, Yang W, Xie BH, Yang MB. Deformation-induced structure evolution of oriented β-polypropylene during uniaxial stretching. Polymer. 2013;**54**:1259-1268. DOI: 10.1016/j.polymer.2012.12.050

[23] Pawlak A, Galeski A. Cavitation during tensile deformation of polypropylene. Macromolecules. 2008;**41**:2839-2851. DOI: 10.1021/ma0715122

[24] Rozanski A, Galeski A, Debowska M. Initiation of cavitation of polypropylene during tensile drawing. Macromolecules. 2011;**44**:20-28. DOI: 10.1021/ma1018523

[25] Rozanski A, Galeski A. Modification of amorphous phase of semi-crystalline polymers. Polimery-w. 2012;**57**:433-440. DOI: 10.14314/polimery.2012.433

[26] Wikipedia. https://en.wikipedia.org/wiki/Wilhelm_R%C3%B6ntgen. 2017

[27] Stribeck N. X-ray Scattering of Soft Matter. Berlin: Springer Science & Business Media; 2007

[28] Donald HB, Pascal E, Edgar W. Review of third and next generation synchrotron light sources. Journal of Physics B: Atomic, Molecular and Optical Physics. 2005;**38**:S773-S797. DOI: 10.1088/0953-4075/38/9/022

[29] Buffet A, Rothkirch A, Dohrmann R, Korstgens V, Abul Kashem MM, Perlich J, Herzog G, Schwartzkopf M, Gehrke R, Muller-Buschbaum P, Roth SV. P03, the microfocus and nanofocus X-ray scattering (MiNaXS) beamline of the PETRA III storage ring: The microfocus endstation. Journal of Synchrotron Radiation. 2012;**19**:647-653. DOI: 10.1107/S0909049512016895

[30] Xu H, Zhao Z. Current status and progresses of SSRF project. Nuclear Science and Techniques. 2008;**19**:191-196. DOI: 10.1016/S1001-8042(08)60013-5

[31] PETRA III. DESY homepage. http://petra3.desy.de/

[32] Als-Nielsen J, McMorrow D. X-rays and their interaction with matter. In: Elements of Modern X-ray Physics. New York: John Wiley & Sons, Inc; 2011. pp. 1-28. DOI: 10.1002/9781119998365.ch1

[33] Als-Nielsen J, Mcmorrow D. Elements of modern X-ray physics. New York: John Wiley & Sons; 2011

[34] Thünemann AF, Ruland W. Microvoids in polyacrylonitrile fibers: A small-angle X-ray scattering study. Macromolecules. 2000;**33**:1848-1852. DOI: 10.1021/ma991427x

[35] Whiteside BR, Martyn MT, Coates PD, Allan PS, Hornsby PR, Greenway G. Micromoulding: Process characteristics and product properties. Plastics, Rubber and Composites. 2003;**32**: 231-239. DOI: 10.1179/146580103225002650

[36] Liu F, Guo C, Wu X, Qian X, Liu H, Zhang J. Morphological comparison of isotactic polypropylene parts prepared by micro-injection molding and conventional injection molding. Polymers for Advanced Technologies. 2012;**23**:686-694. DOI: 10.1002/pat.1946

[37] Chang B, Schneider K, Heinrich G. Microstructural evolution of isotactic-polypropylene during creep: An in situ study by synchrotron small-angle X-ray scattering. Macromolecular Materials and Engineering. 2017;**302**:1700152(1–9). DOI: 10.1002/mame.201700152

[38] Schneider K. Investigation of structural changes in semi-crystalline polymers during deformation by synchrotron X-ray scattering. Journal of Polymer Science Part B: Polymer Physics. 2010;**48**:1574-1586. DOI: 10.1002/polb.21971

[39] Hong K, Rastogi A, Strobl G. A model treating tensile deformation of Semicrystalline polymers: Quasi-static stress-strain relationship and viscous stress determined for a sample of polyethylene. Macromolecules. 2004;**37**:10165-10173. DOI: 10.1021/ma049174h

[40] Millot C, Séguéla R, Lame O, Fillot LA, Rochas C, Sotta P. Tensile deformation of bulk polyamide 6 in the Preyield strain range. Micro–macro strain relationships via in situ SAXS and WAXS. Macromolecules. 2017;**50**:1541-1553. DOI: 10.1021/acs.macromol.6b02471

[41] Selles N, Cloetens P, Proudhon H, Morgeneyer TF, Klinkova O, Saintier N, Laiarinandrasana L. Voiding mechanisms in deformed polyamide 6 observed at the nanometric scale. Macromolecules. 2017;**50**:4372-4383. DOI: 10.1021/acs.macromol.7b00727

[42] Perret R, Ruland W. Single and multiple X-ray small-angle scattering of carbon fibres. Journal of Applied Crystallography. 1969;**2**:209-218. DOI: 10.1107/S0021889869006996

Section 4

Multi-Scale X-Ray Scattering

Chapter 4

Multiscale X-Ray Scattering for Probing Chemo-Morphological Coupling in Pore-to-Field and Process Scale Energy and Environmental Applications

Greeshma Gadikota

Additional information is available at the end of the chapter

http://dx.doi.org/10.5772/intechopen.76266

Abstract

One of the greatest challenges of our generation is the sustainable storage of environmentally harmful by-products of energy production processes. High-level nuclear wastes and CO_2 produced from the energy sectors are examples of these by-products. To ensure the environmentally benign storage of these by-products in a solid form, it is essential to understand the chemical and morphological features of the materials in which these by-products are immobilized. With recent advancements in X-ray scattering, it is now possible to map the structure and the microstructure of architected and natural materials across four decades in spatial scale. Multiscale X-ray scattering that encompasses ultrasmall-, small-, and wide-angle X-ray scattering (USAXS/SAXS/WAXS) allows us to probe material features in the spatial ranges of ~5 μm–10 nm, ~100–1 nm, and ~1 nm–0.2 Å, respectively. This connection is illustrated using two specific examples. The first example involves determination of the changes in the porosity and the structure of beidellite, a swelling clay used in the repository design for nuclear waste disposal, on heating to temperatures above 1000°C. The second example illustrates the changes in the nanoscale porosity of heat-treated serpentine after reacting with CO_2 to form magnesium carbonate.

Keywords: X-ray scattering, porous materials, structural and microstructural changes, hierarchical materials, materials for acid gas storage, contaminant removal

1. Introduction

Developing technological solutions for the long-term and sustainable storage of environmentally harmful by-products of energy production processes is one of the critical needs of our society. Examples of these by-products include high-level nuclear wastes and CO_2 produced from the

energy or industrial sectors. A fundamental understanding of the chemo-morphological coupling in materials containing these immobilized environmentally hazardous by-products is essential for predicting the long-term fate of these contaminants. In this context, chemo-morphological coupling refers to the influence of structural changes in materials at the sub-nanoscale on the nano- and mesoscale morphological changes in materials. Understanding chemo-morphological connectivity in materials allows for establishing a fundamental basis for the bulk-scale properties such as the extent of contaminants immobilized in the solid matrix. The recent development of multiscale X-ray scattering techniques presents a non-invasive, reliable, and robust approach for probing the changes in the structure and morphology of materials from the atomic-to-micrometer scales.

Multiscale X-ray scattering encompasses ultrasmall-, small-, and wide-angle X-ray scattering (USAXS/SAXS/WAXS) measurements. USAXS, SAXS, and WAXS measurements provide a spatial resolution in the range of ~5 μm–10 nm, 100–1 nm, and 1 nm–0.2 Å, respectively. The four decades of spatial scale can be probed in a single measurement within a span of 3–4 min. The capability of connecting microstructural and structural changes using *in-operando* measurements during reaction-inducing events is less than 5 years old [1]. This capability is an extension of the application of ex-situ SAXS measurements to determine the microstructural features of porous materials such as coals [2–7], sedimentary rocks [8], and igneous rocks [9–11]. Other studies quantified the porosity in limestone and sandstone using ultra-small and small angle neutron scattering (USANS/SANS) measurements supported by complimentary electron microscopy imaging [12, 13]. With the recent interest in energy recovery from unconventional formations, the non-invasive characterization of the porosity in shales [14–16] and its constituents such as clays [17–19] using USAXS/SAXS has received increased attention.

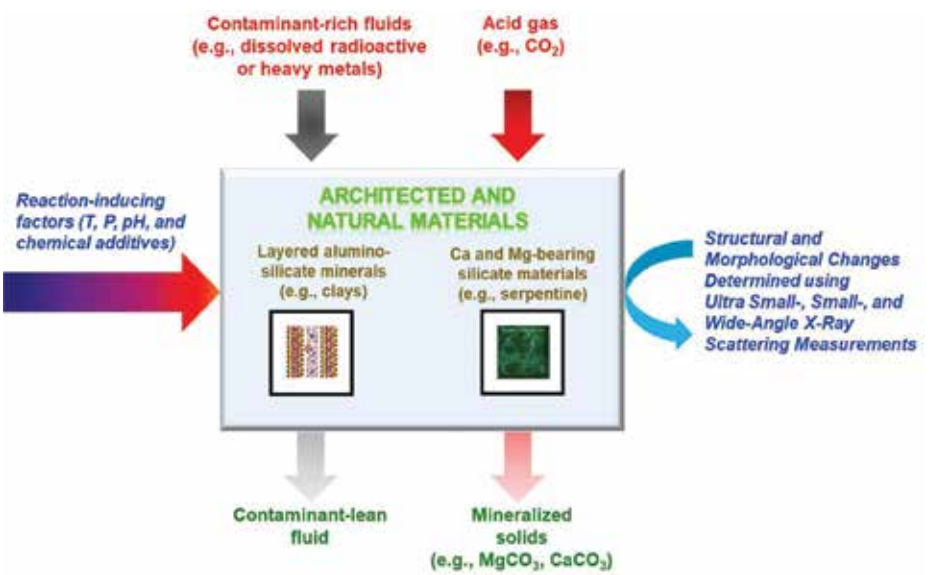

Figure 1. Sustainable energy and environmental applications probed using ultrasmall-, small-, and wide-angle X-ray scattering measurements.

One of the advantages of multiscale X-ray scattering is the ability to probe, *in-operando*, the dynamic changes across the material hierarchy. This approach is illustrated by following the dynamic morphological and structural changes during the heat treatment of beidellite, a swelling clay with a hierarchical material structure. Beidellite, a swelling clay is used in the repository design for nuclear waste disposal and for developing catalytically active materials for clean energy production [20]. Beidellite is the aluminum-rich member of the montmorillonite-beidellite series of minerals [21]. Another example illustrates the reduction in the porosity of heat-treated serpentine on reaction with CO_2 to form magnesium carbonate for the permanent storage of CO_2. These specific examples illustrate the application of multiscale X-ray scattering techniques for probing material transformations at the crystal structural and pore-scale levels for field and process scale applications in energy and environment, as shown in **Figure 1**.

2. Analyses of ultrasmall and small angle scattering data for porous materials

Given the multiscale nature of the applications described in the previous section, powerful techniques such as ultra-small, small, and wide-angle X-ray scattering (USAXS/SAXS/WAXS) are needed to probe the structures of materials across scales. At the angstrom scale, wide angle X-ray scattering (WAXS) provides detailed insights into the internal structure of crystalline materials by modeling the Bragg diffraction peaks. At the nanometer scale, small angle X-ray scattering (SAXS) provides quantitative information regarding the shape and size of the scattering objects including the relative roughness of pore-solid interfaces in porous materials. By combining small angle X-ray scattering (SAXS) with ultra-small angle X-ray scattering (USAXS), it is now possible to quantify the particle and pore sizes across the material hierarchy in architected materials or the fractal morphology in heterogeneous materials from the nanometer to millimeter scale. The key relationships for quantifying the microstructures in materials using small angle scattering are discussed in the following paragraphs.

The measured scattering, $I(\mathbf{Q})$ is related to the spatial distribution of the coherent X-ray or neutron scattering length density, $\rho(\mathbf{r})$ over the sampling volume, V_S using the following expression: [22–24]

$$I(\mathbf{Q}) = \frac{\mathrm{d}\Sigma}{\mathrm{d}\Omega}(\mathbf{Q}) = \frac{1}{V_S}\left|\int_{V_s}\rho(\mathbf{r})\exp(i\mathbf{Q}.\mathbf{r})\,\mathrm{d}^3\,\mathbf{r}\right|^2 \tag{1}$$

Simplification of Eq. (1) by assuming that the isotropic microstructure consists of scattering particles or features of number density, n_P (i.e., volume fraction, $\Phi_V = n_P V_P$) yields Eq. (2) where $|\Delta\rho|^2$, $\gamma_0(r)$, V_P, $F_P^2(Q)$, and $S_P(Q)$ represent the scattering contrast factor, the dimensionless atomic pair correlation function, the individual scattering feature volume, feature form-factor, and the interparticle structure factor, respectively.

$$I(Q) = \frac{\mathrm{d}\Sigma}{\mathrm{d}\Omega}(Q) = n_P\left[\Delta\rho\right]^2 V_P \int_0^\infty 4\pi r^2\,\gamma_0(r)\,\frac{\sin(Qr)}{Qr}\,\mathrm{d}r = n_P\left[\Delta\rho\right]^2 V_P^2\,F_P^2(Q)\,S_P(Q) \tag{2}$$

2.1. Determination of the volume fractions using the scattering invariant

The volume fraction of a given set of scattering features is determined using the scattering invariant. The scattering invariant is obtained by integrating the small angle scattering intensity over all Q [23]. The volume fraction, Φ_v and the scattering invariant are related using the following expression.

$$\text{Scattering invariant} = 2\pi^2 \Phi_V (1-\Phi_V) |\Delta\rho|^2 = \int_0^\infty Q^2 \frac{d\Sigma}{d\Omega}(Q) dQ \tag{3}$$

2.2. Determination of the mean volumes and radius of gyration using the guinier approximation

The mean radius of gyration of narrowly dispersed and uncorrelated scattering features is determined using the Guinier approximation. The following expression relates the scattering intensity, $I(Q)$ to the mean radius of gyration, R_G, particle volume, V_P, the scattering contrast factor, $|\Delta\rho|^2$ and the volume fraction, Φ_v.

$$I(Q) = \frac{d\Sigma}{d\Omega} = \Phi_V |\Delta\rho|^2 V_P \exp\left(-\frac{Q^2 R_G^2}{3}\right) \tag{4}$$

2.3. Determination of the morphology or roughness of solid interfaces from the porod scattering regime

The Porod region is used to probe the local structure at the higher q regimes. In porous materials, the relative roughness or smoothness of the pore-solid interface is quantified using the Porod slope [25]. The Porod slope is determined using the following relationships where $I(Q)$ and n represent the scattering intensity and the slope, respectively:

$$I(Q) = \frac{A}{Q^n} + B \tag{5}$$

$$\log_{10}[I(Q) - B] = \log_{10} A - n \log_{10} Q \tag{6}$$

Scattering from rigid rods provides a Porod slope of 1. Porod slopes between 2 and 3 represent branched systems or networks also known as mass fractals. Porod slopes between 3 and 4 represent rough interfaces with a fractal dimension, D where $n = 6 - D$ and n represents a surface fractal. A smooth surface has a Porod slope of 4. For a smooth surface, the surface area, S_v can be directly related to the scattering intensity, $I(Q)$ and the flat background scattering, bg using the following expression.

$$I(Q) = \frac{2\pi |\Delta\rho|^2 S_v}{Q^4} + bg \tag{7}$$

2.4. Shapes and size distributions

One of the challenges with USAXS and SAXS is the need for microstructural insights prior to the morphological quantification of a material. Information needed *a priori* includes insights

into the polydispersity of the scatterers and shape features such as disks, sheets, laminar structures, cylinders, rods, or capillary pores, core-shell particles [22, 23], and spheres [26, 27]. Once the shape of the features is known, the size distributions can be determined by optimizing the scattering intensity from a predefined set of histogram bin sizes also known as the entropy maximization technique, using a least-squares fitting Fourier Transform method, or fitting a functional form of the size distribution and averaging the scattering over the chosen size distribution function. Homogeneous systems can be fitted using a single functional form. The morphologies of hierarchical materials, on the other hand, are better fitted by binning the scattering intensities corresponding to various sizes. Some of the challenges with this approach include the need for multiple iterations for model convergence and the generation of multiple fitting parameters [28, 29].

3. Brief description of USAXS/SAXS instrumentation

The ability to obtain a wide Q range that spans four decades in spatial resolution from 10^{-4} to 1 $Å^{-1}$ is attributed to the application of Bonse-Hart crystal optics. The flexible geometry, crystal optics independent of the sample apertures, source, and size of the point detector conferred by Bonse Hart crystals allow for the detection of a wide Q range. The constituents of a typical Bonse-Hart USAXS instrument include a pair of collimating crystals, ion chamber, guard slits, analyzer crystals, and a photodiode detector. In order to obtain a monochromatic beam, the pre-monochromated beam is passed through the 2-D slits and a pair of collimating crystals set to the angle satisfying the Bragg condition. The X-rays scattered by the sample are then passed through the analyzer crystals and the intensity is measured by the point detector.

4. Morphological and structural changes in beidellite on heating

4.1. Materials and methods

Beidellite procured from The Source Clay Mineral Repositories (Purdue University, West Lafayette, IN) are ground to a size smaller than 75 μm and compacted into a pellet with a thickness of about 0.5 mm. The pellet is placed in a Linkam TS1500 heating stage (Linkam Scientific Instruments Ltd., Tadworth, UK) in alignment with the synchrotron beamline. The starting and final temperatures of 30°C and 1150°C are set with a temperature ramp rate of 3°C/min. The X-ray scattering measurements are performed at the USAXS instrument at sector 9-ID at the Advanced Photon Source (APS), Argonne National Laboratory, Argonne, IL. Using this instrument, USAXS measurements are combined with pinhole-camera based SAXS measurements and with WAXS measurements. The USAXS, SAXS and WAXS data are represented as a function of the scattering or diffracted intensity, $I(q)$ versus q where $q = (4\pi/\lambda)\sin\theta$ (and $q = (2\pi/d)$ to determine a lattice spacing, d, from an XRD peak in the WAXS data), λ is the X-ray wavelength and θ is half of the scattering or diffracted angle, 2θ. Data collection times for USAXS, SAXS and WAXS are 90, 30, and 30, respectively, for a total of ≈ 3 min, including time for instrument stage motions. The sample configuration within the beam is not changed and the measurements are made within a few minutes of each other. The beam size

settings of (0.8 × 0.8) mm for USAXS and (0.8 × 0.2) mm for SAXS (pinhole SAXS or pin-SAXS) and WAXS are used. The sample-to-detector distances for SAXS and WAXS are set to 547 mm and 181 mm, respectively. The X-ray energy is to 21.0 keV. The total X-ray flux at the sample is ≈10^{13} photon s^{-1}. Silver behenate and NIST standard reference material, SRM 660c (LaB_6) are used for the calibration of q values and sample-to-detector distances. The collected data are reduced and analyzed using the *Irena* [31] and *Nika* [32] software packages written in *IgorPro* (Wavemetrics, Lake Oswego, OR).

4.2. Structural changes in beidellite on heating

One of the interesting structural features in clays is the hierarchical arrangement of the nanosheets and the characteristic interlayer basal distances. The interlayer water confined between the nanosheets contributes to the swelling behavior of these materials. In case of beidellite, a swelling clay, the characteristic interlayer basal spacing decreased from 12.5 to 9.7 Å on heating from 32 to 308°C (**Figure 2**). This reduction in the interlayer basal distance corresponds to the removal of the one layer of interlayer water. A progressive reduction in the intensity of the peak corresponding to the interlayer basal distance of beidellite is also noted on heating to 1150°C. The decreasing peak intensity on heating suggests a reduction in the number of interlayer nanopores on heating. On the structural front, a significant reduction in the intensity of the characteristic beidellite peak that corresponds to q = 4.22 $Å^{-1}$, d = 1.49 Å (h k l: (0 6 0), (3 3 0)) [21] is noted (**Figure 3**). The trend in the reduction of the peak intensity of beidellite on heating is similar to that of Na- and Ca-montmorillonite reported in previous studies [17]. It was interesting to note the onset of significant structural changes in beidellite (**Figure 3**) after a reduction in the interlayer basal distance (**Figure 2**).

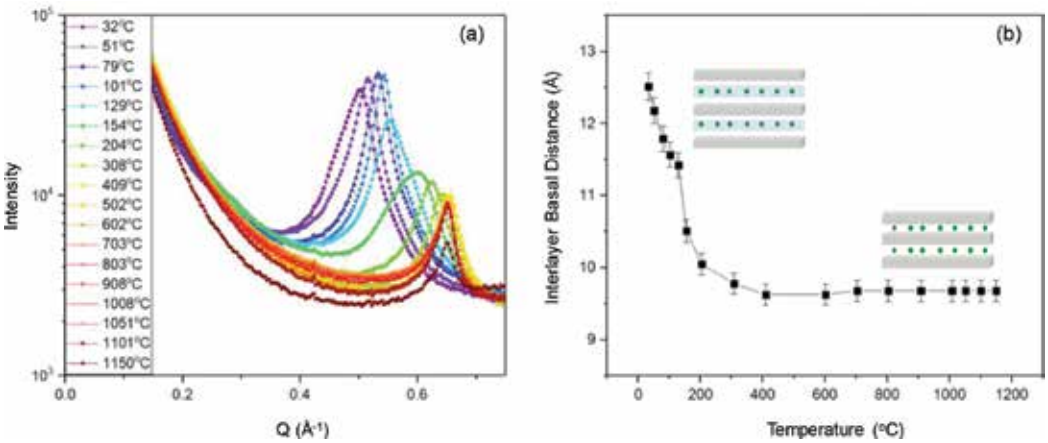

Figure 2. Changes in the characteristic peak corresponding to the interlayer basal distance (d(001) peak) in beidellite (a) and the corresponding d-spacing (b) on heating from 30 to 1150°C. Vertical bars are standard deviation uncertainties obtained from the peak profile fitting.

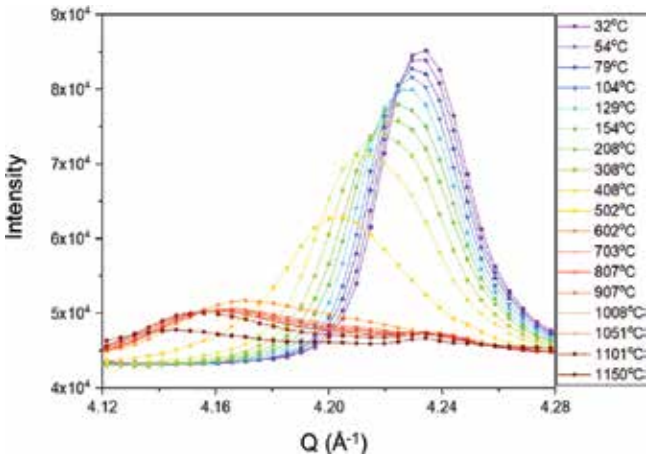

Figure 3. Changes in the characteristic beidellite peak (q = 4.22 Å^{-1}, d = 1.49 Å, *hkl*: 060, 330) [21] on heating to 1150°C.

4.3. Morphological changes in beidellite on heating

The USAXS and SAXS data are collected in the range (10^{-4} to 1.5) Å^{-1} (**Figure 4(a)**). As the temperature is increased from 32 to 1150°C, the scattering intensity increased 43, 58, and 25% at Q = 0.1, 0.001, and 0.0001 Å^{-1}, respectively. While changes in the scattering contrast are noted, significant changes in the shape of the scattering curve are not evident. Another consideration is the extent of reversibility in the morphological changes in beidellite. As discussed in the previous section, the changes in the interlayer basal distance coupled with the structural changes in beidellite produce irreversible morphological changes in beidellite.

To quantify the morphologies in beidellite on heating, the scattering contrast factor, $|\Delta\rho|^2$ is applied. The scattering contrast factor is the square of the difference in the scattering length

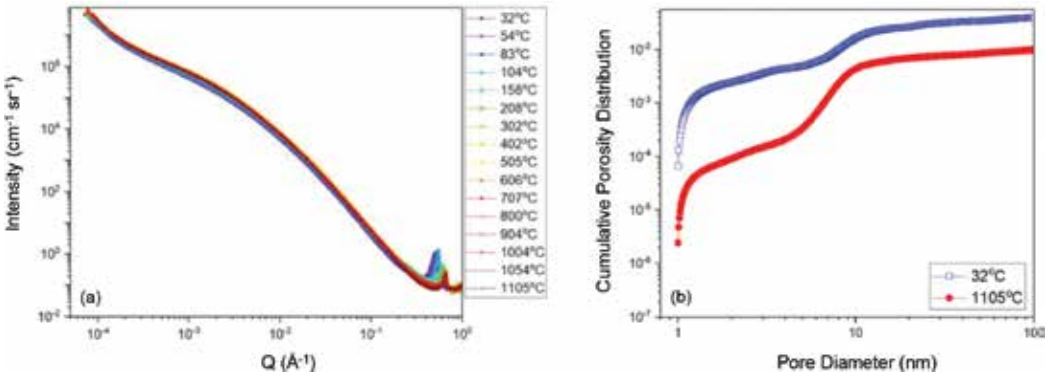

Figure 4. Changes in the combined slit-smeared USAXS/SAXS data for beidellite on heating in temperature ranges of 32–1105°C (a) and the cumulative pore volume distributions at 32°C and 1105°C (b).

density (SLD or ρ) between the two phases. The scattering length density is a function of the chemical composition and density of the phase. In case of beidellite, the scattering contrast factor at the beginning of the experiment emerges from the contrast between the solid and interlayer water. This scattering contrast factor is determined to be 100×10^{28} m^{-4}. On heating to 1105°C, the beidellite structure undergoes significant structural changes as evident in **Figure 3**. The loss of water and densification of the material increase the scattering contrast factor to 500×10^{28} m^{-4}.

To quantify the changes in the morphology of beidellite, the void size distributions are modeled as spheroids with an aspect ratio of 0.2, which allows us to account for the layered morphology of clays. The size distributions are determined using the entropy maximization routine, *MaxEnt* [28, 30]. These results are shown in **Figure 4(b)**. On heating to 1105°C, the porosity in the range of 1–10 nm is reduced by nearly two orders of magnitude. These results are consistent with the reduction in the intensity of the interlayer basal distance corresponding to the porosity between the clay nanosheets as shown in **Figure 2**. This example illustrates one approach to quantify the changes in the nanoscale porosity corresponding to the interlayer basal spacing using USAXS measurements, the interlayer basal spacing in the SAXS regime, and the structure in the beidellite nanosheet in the WAXS regime in a single measurement.

5. Morphological and structural changes in heat-treated serpentine on carbon mineralization

One of the approaches for permanent carbon storage is to use highly reactive Ca- and Mg-bearing substrates that can react with CO_2 to form thermodynamically stable and environmentally benign calcium or magnesium carbonates [33–37]. Examples of reactive Ca- and Mg-bearing materials include wollastonite ($CaSiO_3$), olivine (Mg_2SiO_4), and serpentine ($Mg_3Si_2O_5(OH)_4$). Serpentine is widely mined for extracting nickel and the use of serpentine mine tailings for accelerated carbon mineralization has been proposed [38]. However, the kinetics of CO_2 interactions with serpentine are slow. To accelerate these kinetic interactions, the heat treatment of serpentine is proposed. Heat treating serpentine to temperatures of 625°C dehydroxylates the lattice enabling its conversion to an amorphous state [39]. This amorphous material has a higher reactivity with CO_2 compared to the unreacted material. Recent studies have shown that heat-treated serpentine is effective in capturing and converting CO_2 from flue gas streams to magnesium carbonate [40]. However, the change in the pore size as the heat-treated serpentine is converted to magnesite is not well understood.

A reduction in the porosity of heat-treated serpentine as it is converted to magnesite may potentially limit the reactivity of the material by preventing the migration of Mg. In this context, quantification of the extent of reduction in the porosity of heat-treated serpentine on conversion to magnesium carbonate is useful. Combined ultrasmall, small, and wide angle X-ray scattering (USAXS/SAXS/WAXS) is particularly useful in linking changes in the porosity of heat-treated serpentine to the formation of magnesite. In this study, serpentine was heat-treated to 625°C and the resulting material was reacted at 185°C, P_{CO2} = 139 bar in 1.0 M NaCl and 0.64 M $NaHCO_3$

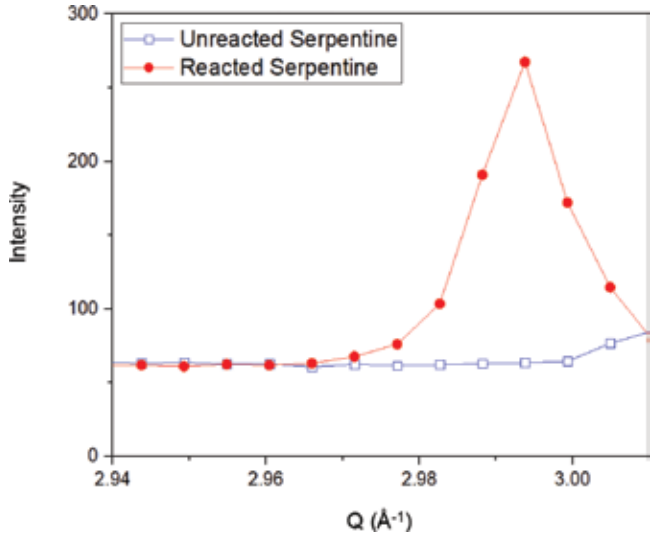

Figure 5. Evidence of the formation of magnesite on the carbon mineralization of heat-treated serpentine (q = 2.99 Å^{-1}, d = 2.10 Å, *hkl*: 113) [41] on heating to 1150°C.

for 3 h while stirring at 300 rpm in a pressurized batch process. The extent of carbonation of heat-treated serpentine to magnesium carbonate is 48%. The particle sizes of these materials before and after carbon mineralization were determined to be in the range of 3–100 μm.

WAXS measurements of the heat-treated serpentine before and after the carbonation reaction showed the formation of magnesite. The characteristic magnesite peak corresponding to q = 2.99 Å^{-1}, d = 2.10 Å and *hkl:* 113 is shown in **Figure 5**. At the lower Q regions, a reduction in the scattering intensity is noted (**Figure 6(a)**). The scattering contrast factors are applied to determine changes in the morphology of the materials. The scattering contrast factor of the

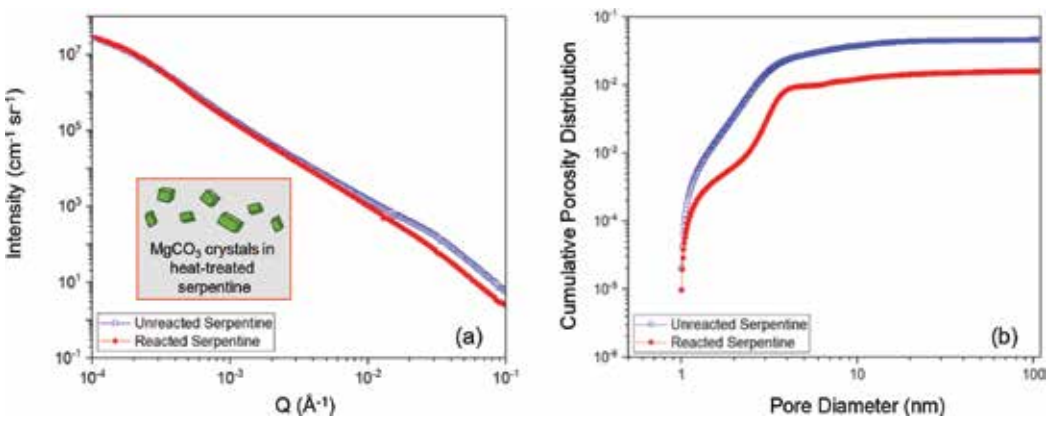

Figure 6. Changes in combined slit-smeared USAXS/SAXS data of heat treated serpentine to form magnesium carbonate (a) and the reduction in the porosity as determined from the scattering data (b).

unreacted and reacted heat-treated serpentine are 446 × 10^{28} m^{-4} and 574 × 10^{28} m^{-4}, respectively. The scattering contrast factors and the void size distributions with an aspect ratio of 1 are the important inputs to determine the morphological changes in these materials using the entropy maximization routine, *MaxEnt* [28, 30]. The changes in the cumulative pore volume distributions of heat-treated serpentine before and after carbon mineralization are shown in **Figure 6(b)**. A significant reduction in the void spaces corresponding to sizes in the range of 2–6 nm is noted. These findings are consistent with the previous observations of reduced porosity due to magnesite growth on olivine grains [35].

6. Conclusions

In this chapter, we have illustrated the use of combined USAXS, SAXS, and WAXS measurements to quantify reaction-driven microstructural and structural changes involving complex architected and natural materials. These materials include beidellite, a swelling clay from the smectite family of minerals, and serpentine, a layered sheet silicate that belongs to the family of phyllosilicates. The combined USAXS, SAXS, and WAXS techniques available at Sector 9-ID at the Advanced Photon Source in Argonne National Laboratory allows for measurements that span nearly four decades in spatial scale. This chapter also illustrates the need for prior knowledge about the morphological arrangement in materials to quantify the key features such as the changes in the porosity or surface area of porous materials on reaction. In this context, recent advancements in electron microscopy and X-ray tomography have aided the quantitative interpretation of the X-ray scattering measurements discussed in this chapter.

Acknowledgements

The author gratefully acknowledges the Wisconsin Alumni Research Foundation and the College of Engineering at the University of Wisconsin, Madison. A special thanks to Dr. Jan Ilavsky and Dr. Ivan Kuzmenko, X-ray Science Division, Argonne National Laboratory, for providing experimental support for the combined USAXS/SAXS/WAXS measurements at the Advanced Photon Source. The use of the Advanced Photon Source, an Office of Science User Facility operated for the U.S. Department of Energy (DOE) Office of Science by Argonne National Laboratory, is supported by the U.S. DOE under Contract DE-AC02-06CH11357.

Author details

Greeshma Gadikota

Address all correspondence to: gadikota@wisc.edu

Department of Civil and Environmental Engineering, Environmental Chemistry and Technology Program, Geological Engineering Program, Grainger Institute for Engineering, University of Wisconsin, Madison, USA

References

[1] Freelon B, Suthar K, Ilavsky J. A multi-length-scale USAXS/SAXS facility: 10-50 keV small-angle X-ray scattering instrument. Journal of Applied Crystallography. 2013; **46**(5):1508-1512

[2] Reich MH, Russo SP, Snook IK, Wagenfeld HK. The application of SAXS to determine the fractal properties of porous carbon-based materials. Journal of Colloid and Interface Science. 1990;**135**(2):353-362

[3] Radlinski AP, Radlinska EZ. The microstructure of pore space in coals of different rank. In: Coalbed Methane: Scientific, Environmental and Economic Evaluation. Springer Netherlands; 1999. pp. 329-365

[4] Radlinski AP, Mastalerz M, Hinde AL, Hainbuchner M, Rauch H, Baron M, Lin JS, Fan L, Thiyagarajan P. Application of SAXS and SANS in evaluation of porosity, pore size distribution and surface area of coal. International Journal of Coal Geology. 2004;**59**(3):245-271

[5] McMahon PJ, Snook IK, Treimer W. The pore structure in processed Victorian brown coal. Journal of Colloid and Interface Science. 2002;**252**(1):177-183

[6] Prinz D, Pyckhout-Hintzen W, Littke R. Development of the meso-and macroporous structure of coals with rank as analysed with small angle neutron scattering and adsorption experiments. Fuel. 2004;**83**(4):547-556

[7] Bale HD, Schmidt PW. Small-angle X-ray-scattering investigation of submicroscopic porosity with fractal properties. Physical Review Letters. 1984;**53**(6):596

[8] Cohen MH. The morphology of porous sedimentary rocks. Physics and Chemistry of Porous Media-II. 1987;**154**(1):3-16

[9] Lucido G, Triolo R, Caponetti E. Fractal approach in petrology: Small-angle neutron scattering experiments with volcanic rocks. Physical Review B. 1988;**38**(13):9031

[10] Floriano MA, Venezia AM, Deganello G, Svensson EC, Root JH. The structure of pumice by neutron diffraction. Journal of Applied Crystallography. 1994;**27**(3):271-277

[11] Kahle A, Winkler B, Radulescu A, Schreuer J. Small-angle neutron scattering study of volcanic rocks. European Journal of Mineralogy. 2004;**16**(3):407-417

[12] Anovitz LM, Lynn GW, Cole DR, Rother G, Allard LF, Hamilton WA, Porcar L, Kim MH. A new approach to quantification of metamorphism using ultra-small and small angle neutron scattering. Geochimica et Cosmochimica Acta. 2009;**73**(24):7303-7324

[13] Anovitz LM, Cole DR, Rother G, Allard LF, Jackson AJ, Littrell KC. Diagenetic changes in macro-to nano-scale porosity in the St. Peter sandstone: An (ultra) small angle neutron scattering and backscattered electron imaging analysis. Geochimica et Cosmochimica Acta. 2013;**102**:280-305

[14] Gu X, Cole DR, Rother G, Mildner DF, Brantley SL. Pores in marcellus shale: A neutron scattering and FIB-SEM study. Energy & Fuels. 2015;**29**(3):1295-1308

[15] Bahadur J, Radlinski AP, Melnichenko YB, Mastalerz M, Schimmelmann A. Small-angle and ultrasmall-angle neutron scattering (SANS/USANS) study of New Albany shale: A treatise on microporosity. Energy & Fuels. 2015;**29**(2):567-576

[16] Lee S, Fischer TB, Stokes MR, Klingler RJ, Ilavsky J, McCarty DK, Wigand MO, Derkowski A, Winans RE. Dehydration effect on the pore size, porosity, and fractal parameters of shale rocks: Ultrasmall-angle X-ray scattering study. Energy & Fuels. 2014; **28**(11):6772-6779

[17] Gadikota G, Zhang F, Allen AJ. Towards understanding the microstructural and structural changes in natural hierarchical materials for energy recovery: In-operando multi-scale X-ray scattering characterization of Na- and Ca-montmorillonite on heating to 1150 °C. Fuel. 2017;**196**:195-209

[18] Gadikota G, Zhang F, Allen A. In-situ angstrom-to-micrometer characterization of the structural and microstructural changes in kaolinite on heating using ultrasmall-angle, small-angle, and wide-angle X-ray scattering (USAXS/SAXS/WAXS). Industrial & Engineering Chemistry Research. 2017;**56**(41):11791-11801

[19] Gadikota G, Allen AJ. Microstructural and structural characterization of materials for CO_2 storage using multi-scale scattering methods. In: Li L, Wong-Ng W, editors. Materials and Processes for CO_2 Capture, Conversion, and Sequestration. Hoboken, NJ: Wiley Books; 2018

[20] De Stefanis A, Tomlinson AAG. Towards designing pillared clays for catalysis. Catalysis Today. 2006;**114**(2-3):126-141

[21] Weir AH, Greene-Kelly R. Beidellite. American Mineralogist. 1962;**47**:137-146

[22] Fournet G, Guinier A. Small Angle Scattering of X-Rays. New York: John Wiley & Sons; 1955

[23] Glatter O, Kratky O. Small angle scattering. New York: Academic; 1982

[24] Warren BE. X-Ray Diffraction. New York: Dover; 1990

[25] Porod G. X-ray low angle scattering of dense colloid systems, part II. Kolloid Zeitschrift. 1952;**125**:108-122

[26] Roess LC, Shull CG. X-ray scattering at small angles by finely-divided solids. II. Exact theory for random distributions of spheroidal particles. Journal of Applied Physics. 1947;**18**(3):308-313

[27] Shull CG, Roess LC. X-ray scattering at small angles by finely-divided solids. I. General approximate theory and applications. Journal of Applied Physics. 1947;**18**(3):295-307

[28] Potton JA, Daniell GJ, Rainford BD. Particle size distributions from SANS data using the maximum entropy method. Journal of Applied Crystallography. 1988;**21**(6):663-668

[29] Morrison JD, Corcoran JD, Lewis KE. The determination of particle size distributions in small-angle scattering using the maximum-entropy method. Journal of Applied Crystallography. 1992;**25**(4):504-513

[30] Potton JA, Daniell GJ, Eastop AD, Kitching M, Melville D, Poslad S, Rainford BD, Stanley H. Ferrofluid particle size distributions from magnetisation and small angle neutron scattering data. Journal of Magnetism and Magnetic Materials. 1983;**39**:95-98

[31] Ilavsky J, Jemian PR. Irena: Tool suite for modeling and analysis of small-angle scattering. Journal of Applied Crystallography. 2009;**42**(2):347-353

[32] Ilavsky J. Nika: Software for two-dimensional data reduction. Journal of Applied Crystallography. 2012;**45**(2):324-328

[33] Gadikota G, Natali C, Boschi C, Park AHA. Morphological changes during enhanced carbonation of asbestos containing material and its comparison to magnesium silicate minerals. Journal of Hazardous Materials. 2014;**264**:42-52

[34] Gadikota G, Swanson EJ, Zhao H, Park A-HA. Experimental design and data analysis for accurate estimation of reaction kinetics and conversion for carbon mineralization. Industrial and Engineering Chemistry Research. 2014;**53**(16):6664-6676

[35] Gadikota G, Matter J, Kelemen P, Park A-HA. Chemical and morphological changes during olivine carbonation for CO_2 storage in the presence of NaCl and $NaHCO_3$. Physical Chemistry Chemical Physics. 2014;**16**(10):4679-4693

[36] Gadikota G, Fricker K, Jang S-H, Park A-HA. Carbonated silicate minerals and industrial wastes as construction materials. In: Advances in CO_2 Capture, Sequestration, and Conversion. Washington, DC: American Chemical Society; 2015. pp. 295-322

[37] Lackner KS. Carbonate chemistry for sequestering fossil carbon. Annual Review of Energy and the Environment. 2002;**27**(1):193-232

[38] Wilson SA, Raudsepp M, Dipple GM. Verifying and quantifying carbon fixation in minerals from serpentine-rich mine tailings using the Rietveld method with X-ray powder diffraction data. American Mineralogist. 2006;**91**(8-9):1331-1341

[39] McKelvy MJ, Chizmeshya AVG, Diefenbacher J, Béarat H, Wolf G. Exploration of the role of heat activation in enhancing serpentine carbon sequestration reactions. Environmental Science & Technology. 2004;**38**(24):6897-6903

[40] Werner M, Hariharan S, Mazzotti M. Flue gas CO_2 mineralization using thermally activated serpentine: From single-to double-step carbonation. Physical Chemistry Chemical Physics. 2014;**16**(45):24978-24993

[41] Brown G, Brindley GW. Crystal Structures of Clay Minerals and their X-Ray Identification. London: Mineralogical Society; 1980

Section 5

Small-Angle Scattering Analysis of Fractals

Chapter 5

Small-Angle Scattering Analysis of Fractals Generated by Additive Cellular Automata

Azat Mukhiddinuly Slyamov and
Eugen Mircea Anitas

Additional information is available at the end of the chapter

http://dx.doi.org/10.5772/intechopen.74498

Abstract

Structural analysis of fractals generated using one-dimensional additive cellular automata (ACA) is presented in this chapter. ACA is a dynamical system that evolves in discrete steps and generates two-dimensional self-similar structures. We investigate the structure of M-state ACA Rule 90 and Rule 150 using small-angle scattering (SAS; X-rays, neutrons, light) technique and multi-fractal analysis. We show how the scattering data from ACA can provide information about the overall size of the system, the number of total units, the number of rows, the size of the basic fractal units, the scaling factor, and the fractal dimension. In this case, when a particular row number reproduces a complete structure of the fractals, we can also obtain the fractal iteration number. We show that subsets of different states of M-state ACA can manifest both mono- and multi-fractal properties. We provide some useful relations between structural parameters of ACA that can be obtained experimentally from SAS.

Keywords: small-angle scattering, multi-fractals, fractals, cellular automata

1. Introduction

Morphology of many systems at nano- and microscales appears to exhibit properties of scaling and self-similarity [1], meaning that they completely or partially preserve their structure on different scales of observation. Such structures are referred as fractals and are the objects of the fractal geometry [2]. The main parameter of the fractal is the fractal (Hausdorff) dimension D that is defined by the minimal number of spheres $N(r)$ of the size r that can penetrate each other and are needed to cover all points containing the object, as [3]

$$N(r) = N_0 r^{-D}, \tag{1}$$

where N_0 is a constant. Usually, fractal objects have non-integer value of D, whereas regular shapes have fractal dimension equal to the dimension of the space into which they are embedded. Thus, fractal dimensions of point, line, and regular surface are 0, 1, and 2, respectively.

One of the most efficient ways to investigate structures at nanoscale that exhibit fractal properties is a small-angle scattering (SAS) of X-ray (SAXS), neutron (SANS), and light (SALS) [4]. SAS gives an information about the structure of the sample from the spatial variations of its electron density, providing the differential cross section as a function of transferred momentum. When neutrons are used, the scattering is given by the interaction of the incident beam with the atomic nuclei and with the magnetic moments [5]. For X-rays, the scattering is mainly determined by their interaction with the electrons. Then, the obtained cross section represents the spatial density-density correlations in the investigated volume. Generally, data analysis and model development procedures can be interchanged between SANS and SAXS since the wavelength of X-rays is of the same order of magnitude as those of thermal neutrons [6]. The SAS technique has the net advantage that is noninvasive, the investigated samples do not require additional preparation, and physical quantities are averaged over a macroscopic volume.

The main advantage of the SAS in the investigations of the fractals is the power-law behavior of the scattering exponent of the scattering intensity $I(q)$ that reveals one of the main features of the fractal, the fractal dimension, as [7]

$$I(q) \sim q^{-D}, \tag{2}$$

where $q = (4\pi \sin 2\theta)/\lambda$, θ is the scattering angle, and λ is the wavelength of incident radiation. The exponent D is the fractal dimension. For fractal structures, SAS can also differentiate between mass [4] and surface fractals [8, 9]. It was shown, recently, that SAS can be applied in structural investigations of various types of fractals [10], as fat fractals [11, 12] and chaos-game representation of fractals [13].

Many algorithms of the fractal construction exist, and most of them require either contraction or expansion mappings of the object onto itself, in order to obtain scaled and self-similar pattern [2, 14]. In the case of deterministic fractals, self-similarity is exact, meaning that the fractal is identical at all scales. Usually, natural systems do not have deterministic structure, and self-similarity they exhibit is stochastic. One can model them by introducing some randomness, assigning probabilities to generating rules. In addition, some systems can be multifractals, so they have more than one fractal dimension or scaling rule. The processes of generating all these fractals are performed separately, depending on which of particular type of fractal is needed to model and investigate. However, there is a mathematical model called cellular automata (CA) that can show a very diverse and complex behavior and manifests the properties of all different types of fractals [15–17].

Cellular automaton (CA) is a simple model of locally interacting dynamical systems that evolve in discrete steps. Single cellular automaton represents the site that has a finite number

of states and changes each step, depending on the states of the neighboring sites. Although each site of the CA evolves according to the same rule, interactions between neighboring sites can lead to fairly complex patterns. CA can generate a large diversity of structures using simple initial conditions and their transition rules. CAs are often used as a model of physical systems with many degrees of freedom as biological systems, percolation clusters, diffusion-limited aggregates, and others. A particular type of CA, called additive cellular automata, can generate self-similar fractals [18, 19, 22].

In the case of CA consisting of a line of sites (one-dimensional CA), it is known that they fall into four distinct universality classes [15, 16]:

a. Spatially homogeneous state, yielding behavior similar to limit points.

b. Sequence of simple stable or periodic structures, yielding behavior similar to limit cycles.

c. Chaotic aperiodic behavior, similar to "strange" attractors.

d. Complicated localized structures, where properties are undecidable.

In the approach used here, we view additive cellular automata (ACA) as discrete dynamical systems, in which the set of possible configurations ACA forms a fractal set [18, 19]. We provide characterization of structural properties of the fractals generated by additive cellular automata using small-angle scattering technique and multi-fractal analysis. We consider each site as a scattering unit. Scattering structure factors are calculated using efficient optimization of Debye formula [20, 21]. We show here how to extract structural information and fractal properties of ACA from SAS data, such as the fractal dimension, the overall size of the sample, the sizes of basic units, the scaling factor, and the number of generated steps.

2. Theoretical background

The following section presents the theoretical basics of used models and methods. We briefly explain the mathematical description of the cellular automata and the theoretical foundations of the small-angle scattering technique. We also discuss the transition matrix method as an algorithm for calculating the fractal dimension of ACA.

2.1. Cellular automata

In general, an arbitrary site of the $M = p^t$-state CA, where p is a prime and t is a natural number, with the value a_i^k at position i and step k is determined by a transition rule and depends on the state of the site itself and states of its neighbors $i + r_1, i + r_2, \cdots i + r_l$ at step $k - 1$; thus

$$a_i^k = \phi\left(a_{i+r_1}^{k-1}, a_{i+r_2}^{k-1}, \cdots, a_{i+r_l}^{k-1}\right), \tag{3}$$

where $(r_1, r_2, \cdots, r_l) \in \left(\mathbb{Z}^d\right)^l$ is called a neighborhood index and $d \in \mathbb{N}$ is the dimensionality of the lattice. A particular type of CA called additive cellular automata is described by an additive (linear) rule of the type:

$$a_i^k = c_1 a_{i+r_1}^{k-1} + c_2 a_{i+r_2}^{k-1} + \cdots + c_m a_{i+r_l}^{k-1} \mod M, \tag{4}$$

where $c_i \in \mathbb{N}$ are coefficients with $i = 1, \cdots, l$. The initial state contains a single element that is considered as a non-zero site. For other initial conditions with multiple non-zero sites, due to linearity property, we shall obtain a superposition of structures generated from a single site [22].

There are two unique and distinct nontrivial one-dimensional ACA rules that can be obtained by using Eq. (4). In the first case, we have $r_1 = -1$, $r_2 = 1$, and all other terms equal to zero; the obtained relation will be given by

$$a_i^k = c_1 a_{i-1}^{k-1} + c_2 a_{i+1}^{k-1} \mod M. \tag{5}$$

The structure generated by such rule for 2-state ACA when $c_i = 1$ is shown in **Figure 1** (left part). In the limit of the high number of generated steps, this structure will be nothing but the well-known Sierpinski triangle fractal. In the second case, we choose $r_1 = -1$, $r_2 = 0$, $r_3 = 1$, and all other terms equal to zero. Therefore, the recurrence relation becomes

$$a_i^k = c_1 a_{i-1}^{k-1} + c_2 a_i^{k-1} + c_3 a_{i+1}^{k-1} \mod M. \tag{6}$$

The structure generated by this rule for $M = 2$ and $c_i = 1$ is shown in **Figure 1** (right part). Unlike the previous case, when the whole structure is self-similar, this structure has self-similar parts [22]. Since the structure generated by ACA is self-similar, then one can determine its fractal dimension [23]. It was shown that the growth rate dimension of ACA is equal to the fractal dimension [18, 19] and given by

$$D = \lim_{k \to \infty} \frac{\log N_k}{\log k}, \tag{7}$$

where N_k is the total number of non-zero state sites.

$$\begin{pmatrix}
0&0&0&0&0&0&0&1&0&0&0&0&0&0&0\\
0&0&0&0&0&0&1&0&1&0&0&0&0&0&0\\
0&0&0&0&0&1&0&0&0&1&0&0&0&0&0\\
0&0&0&0&1&0&1&0&1&0&1&0&0&0&0\\
0&0&0&1&0&0&0&0&0&0&0&1&0&0&0\\
0&0&1&0&1&0&0&0&0&0&1&0&1&0&0\\
0&1&0&0&0&1&0&0&0&1&0&0&0&1&0\\
1&0&1&0&1&0&1&0&1&0&1&0&1&0&1
\end{pmatrix}
\qquad
\begin{pmatrix}
0&0&0&0&0&0&0&1&0&0&0&0&0&0&0\\
0&0&0&0&0&0&1&1&1&0&0&0&0&0&0\\
0&0&0&0&0&1&0&1&0&1&0&0&0&0&0\\
0&0&0&0&1&1&0&1&0&1&1&0&0&0&0\\
0&0&0&1&0&0&0&1&0&0&0&1&0&0&0\\
0&0&1&1&1&0&1&1&1&0&1&1&1&0&0\\
0&1&0&1&0&0&0&1&0&0&0&1&0&1&0\\
1&1&0&1&1&0&1&1&1&0&1&1&0&1&1
\end{pmatrix}$$

Figure 1. Cellular automata generated by Rule 90 (left part) and Rule 150 (right part).

A more general case of fractal structure can be obtained by considering that the states M and coefficients c_i of each site can take arbitrary values. For arbitrary M, we name these patterns "M-state Rule 90" and "M-state Rule 150" in order to underline that the recurrence relations are the same for each number of possible states. For $M = 2$ and $c_i = 1$, Eqs. (5) and (6) give the well-known ACA Rule 90 and Rule 150, respectively.

2.2. Transition matrix method

One additional effective approach to compute the fractal dimension of ACA is the TM method [18] which analyzes only the transition rule. Let us suppose a set of one-dimensional blocks of length m with all possible configurations of M states. The length of the blocks should not be less than the difference in positions of the first and the last terms (neighbors) in Eq. (4), i.e., $r_l - r_1 \leq m$. Omitting the trivial block with all zero elements, there are $u = 2^m - 1$ of *nontrivial* blocks left. We can define a configuration of u th block of length m by inserting zeros, as $\left[0\ a_i^k\ 0\ a_{i+1}^k\ 0 \cdots 0\ a_m^k\ 0\right]$. Then, applying an ACA transition function (see Eq. (4)) on this configuration, we obtain $\left[a_i^{k+1}\ a_{i+1}^{k+1} \cdots a_m^{k+1}\right]$. The transition matrix shows how many blocks of a certain type are generated by the transition function from the configuration of uth block. The largest eigenvalue λ of the transition matrix gives the fractal dimension D of the ACA by using the relation [18]

$$D = \log_M \lambda. \tag{8}$$

For Rule 90 the length of the block $m = 2$ and the number of states $M = 2$, so the number of distinct nontrivial blocks $u = 3$, and they are [0 1], [1 0], and [1 1]. Now, inserting zeros between elements of the blocks and applying Eq. (5), we obtain

$$\frac{[0\,0\,0\,1\,0]}{[0\,0\,1\,0\,1]}\ \frac{[0\,1\,0\,0\,0]}{[1\,0\,1\,0\,0]}\ \frac{[0\,1\,0\,1\,0]}{[1\,0\,0\,0\,1]},$$

for the purpose of finding the transition matrix, we reduce upper configurations to three middle elements in the row [18]:

$$\frac{[0\,0\,1]}{[0\,1\,0]}\ \frac{[1\,0\,0]}{[0\,1\,0]}\ \frac{[1\,0\,1]}{[0\,0\,0]}.$$

Calculating the number of different blocks in each obtained reduced two-row configurations, the transition matrix can be derived. In the first configuration, block [0 1] appears twice and [1 0] once; in the second [1 0] once and [0 1] twice; and in the third both [1 0] and [0 1] once. In all configurations block [1 1] does not occur. The final form of the transition matrix for Rule 90 is

$$\begin{bmatrix} 2 & 1 & 1 \\ 1 & 2 & 1 \\ 0 & 0 & 0 \end{bmatrix}.$$

	M = 2	M = 3	M = 4	M = 5	M = 6	M = 7	M = 8	M = 9
Rule 90	1.58496	1.63093	1.58496	1.68261	1.61315	1.71241	1.58496	1.63093
Rule 150	1.69424	1.63093	1.69424	1.82948	1.70622	1.84558	1.69424	1.63093

Table 1. Fractal dimension D of M-state Rule 90 and Rule 150.

From **Table 1** one can see that at $M = 2,\ 4,\ 8$ and $M = 3,\ 9$ all the fractal dimensions are equal both for M-state Rule 90 and Rule 150. The same results hold for any $M = p^t$-state ACA at constant p and arbitrary t. It is known that if a fractal consists of two or more different sub-fractals, then the fractal dimension of the fractal is equal to the biggest value among fractal dimensions of the sub-fractals [24].

The most natural way is to consider an M-state ACA as a composition of sub-fractals formed by different values of the ACA sites. Since an M-state ACA has $M - 1$ non-zero distinct states, 4-state ACA can be presented as a decomposition into three subsets of different states. **Figure 2** shows the decomposition of 4-state Rule 90 and Rule 150 into the corresponding sets of state-1, state-2, and state-3. Thereafter, we refer to "set of state-i" simply as "state-i." All three subsets have nonuniform distribution of points and, thus, may have properties of multi-fractals.

To characterize such nonuniform fractals, one needs to weight the well-known box-counting method according to the number of points inside a box. Then, one can define a generalized dimension spectrum as

$$D_s = \frac{1}{s-1} \lim_{r \to 0} \frac{\log \sum_i P_i^s}{\log r}, \tag{9}$$

where $P_i \equiv \mu(\mathcal{B}_i)/\mu((A))$ is the normalized measure of the ith box $\mathcal{B}_i$. We use here the barycentric fixed-mass (BFM) method to estimate the dimension spectra, both for ACA and their subsets [25]. In order to perform such analysis, as for the SAS, we consider occupied sites of ACA as points. In the BFM method, the boxes grow by reaching their nearest neighbor that covers the same mass. At large scales when leveling effect occurs, an effective way to reduce it can be accomplished by a pivot point selection and usage of a non-overlapping criteria for reduction of the edge effects, for computational time and for precision improvements [25].

2.3. Small-angle scattering

In this chapter we provide a structural analysis of 2-state ACA and 4-state ACA. The latter ones presented in **Figure 2** is considered as a 2-state system, regardless of the value of each occupied site, meaning that there are only two possible values of the site, "*occupied*" and "*not occupied*," as shown in **Figure 3**. In the similar manner, all subsets of different states in 4-state ACA are also considered as 2-state system.

Generally, a typical small-angle scattering experiment performed using beams of neutrons, X-rays, or light. Experimental setup consists of a source of monochromatic beam of particles, an irradiated sample, and a detector. The incident beam with wave vector $\mathbf{k}_i$ scatters the

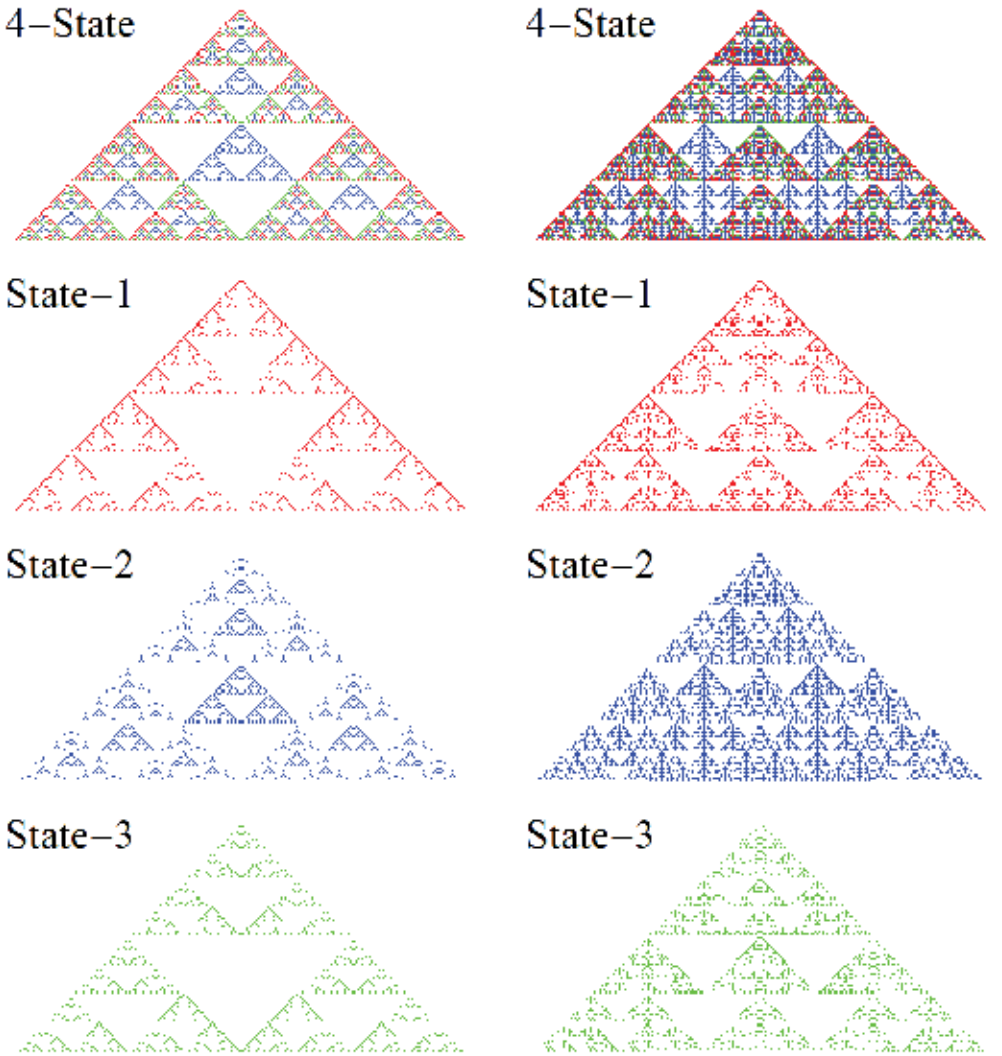

Figure 2. Decomposition of 4-state CA into subsets of state-1, state-2, and state-3. Upper part: Rule 90; lower part: Rule 150.

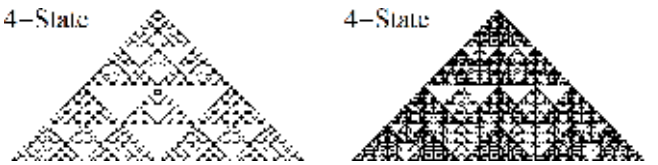

Figure 3. Representation of 4-state ACA as 2-state system. Left part: Rule 90; right part: Rule 150.

sample with the wave vector $\mathbf{k}_f$ at the angle 2θ. The quantity measured is the differential cross section per unit volume as a function of the scattering vector $\mathbf{q} = \mathbf{k}_i - \mathbf{k}_f$.

Let us suppose an ensemble of objects with scattering length b_j and the scattering length density *SLD* $\rho(\boldsymbol{r}) = \sum_j b_j(\boldsymbol{r} - \boldsymbol{r}_j)$ [5], where $\boldsymbol{r}_j$ is the position of the scattering units. The total scattering amplitude is defined by the Fourier transform of $\rho(\boldsymbol{r})$ by $A(\boldsymbol{q}) \equiv \int_v \rho(\boldsymbol{r}) e^{-i\boldsymbol{q}\cdot\boldsymbol{r}} \mathrm{d}^3 r$, where v is the total irradiated volume. If we consider scattering from the system where particles of density ρ_m are immersed in a uniform solid matrix of density ρ_p, then the scattering contrast will be given as $\Delta\rho = \rho - \rho_0$, and the intensity from the entire sample can be obtained according to

$$I(q) = c|\Delta\rho|^2 V^2 \left\langle |F(\boldsymbol{q})|^2 \right\rangle, \tag{10}$$

where c is the concentration of objects, V is the volume of each object, and $F(\boldsymbol{q}) = \frac{1}{V}\int_V e^{-i\boldsymbol{q}\cdot\boldsymbol{r}} \mathrm{d}^3 r$ is the normalized form factor with $F(0) = 1$. The symbol $\langle \cdots \rangle$ stands for ensemble averaging over all orientations.

Real fractal samples usually have polydisperse distribution of the sizes of composing units. Thus, the corresponding scattering intensity from polydisperse fractals can be regarded as the sum of each individual form factor weighted with the corresponding volume V and contrast $\Delta\rho$. We choose here a continuous distribution $D_{N_k}(l)$ of fractals with different sizes l that gives the probability of finding a fractal of the size l lying in the range $(l, l + dl)$. We consider here a lognormal distribution of fractal sizes, such as

$$D_{N_k}(l) = \frac{1}{\sigma l (2\pi)^{1/2}} e^{-\frac{\left(\log(l/\mu_0) + \sigma^2/2\right)^2}{2\sigma^2}}, \tag{11}$$

where $\sigma = \left(\log\left(1 + \sigma_{\mathrm{r}}^2\right)\right)^{1/2}$, $\mu_0 = \langle l \rangle_D$ is the mean length, $\sigma_{\mathrm{r}} = \left(\langle l^2 \rangle - \mu_0^2\right)^{1/2}/\mu_0$ is the relative variance, and $\langle \cdots \rangle_D = \int_0^\infty \cdots D_{N_k}(l)\mathrm{d}l$. Since for a polydisperse fractal dispersion the volume of each fractal has a continuous variation with its size, we have

$$I(q) = c|\Delta\rho|^2 \int_0^\infty \left\langle \left| F\left(\vec{q}\right) \right|^2 \right\rangle V^2(l) D_{N_k}(l) \mathrm{d}l, \tag{12}$$

where $F(\boldsymbol{q})$ is the normalized form factor. Since in our investigations we use cellular automata (CA) to generate the N_k sites that are considered as scattering points, we shall compute the scattering intensity using the Debye formula [20]:

$$I(q) = N_k I_{\mathrm{s}}(q) + 2F_{\mathrm{s}}(q)^2 \sum_{i=1}^{N_k - 1} \sum_{j=i+1}^{N_k} \frac{\sin qr_{ij}}{qr_{ij}}, \tag{13}$$

where $I_{\mathrm{s}}(q)$ is the intensity scattered by each fractal unit and r_{ij} is the distance between units i and j. When the number of units exceeds few thousands, the computation of the term $\sin\left(qr_{ij}\right)/\left(qr_{ij}\right)$ is very time-consuming and can be handled via a pair-distance histogram $g(r)$, with a bin-width commensurate with the experimental resolution [21]. Thus, Eq. (13) becomes

$$I(q) = N_k I_s(q) + 2F_s^2(q) \sum_{i=1}^{N_{bins}} g(r_i) \frac{\sin qr_i}{qr_i}, \tag{14}$$

where $g(r_i)$ is the pair-distance histogram at pair distance r_i. For determining fractal properties, we can neglect the form factor and consider $I_s(q) = F_s^2(q) = 1$. Thus, Eq. (14) gives the structure factor:

$$S(q) = N_k + 2 \sum_{i=1}^{N_{bins}} g(r_i) \frac{\sin qr_i}{qr_i}. \tag{15}$$

3. Results and discussion

3.1. 2-state ACA

Results of numerical calculations for mono- and polydisperse scattering structure factors of 2-state ACA Rule 90 and Rule 150 with $c_i = 1$ at different steps k are shown in **Figure 4**.

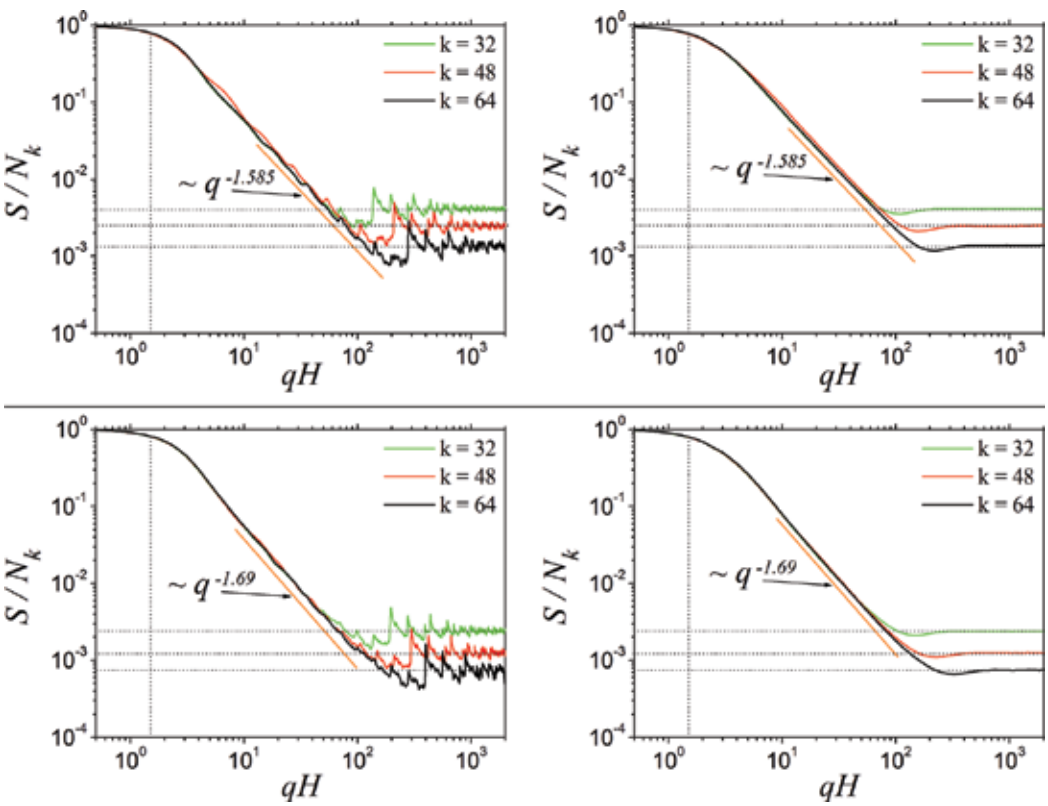

Figure 4. Monodisperse (left part) and polydisperse (right part) structure factors of 2-state ACA. Upper part: Rule 90; lower part: Rule 150.

Usually, scattering structure factor spectra consist of three main regions. The first one, Guinier region, is characterized by constant intensity at low q range and indicates the overall size of the irradiated sample by the rightmost part of the plateau as $q \approx 2\pi/H$, where H is the height of the ACA. The following region is called fractal and provides information about fractal properties of the sample from the power-law behavior of the scattering curve. The slope of the curve reveals the fractal dimension of the sample, and the rightmost part of the fractal region is related with the sizes of basic units, as $q \approx 2\pi/l$, where l is the side length of the basic unit. The presence of the most pronounced minima and their periodicity in this region can say about the fractal iteration number and the scaling factor. The third characteristic region is asymptote at high values of q that gives the number of units composing the fractal sample. Note that for the purposes of our investigations we normalized the size of all ACA at different steps k, in order to compare only their structural and fractal properties; thus, at low q all scattering curves are approximately equal.

From monodisperse scattering data (**Figure 4**, left part), one can find that at steps $k = 32$ and $k = 64$ curves almost completely overlap each other in Guinier and fractal regions, except the asymptotic region due to different numbers of composing units. While behavior of the curve at $k = 48$ is different, which arises from the fact that for $M = p^t$-state ($t \in \mathbb{N}$) ACA the number of steps which generates a complete fractal structure is $k = p^n$ [18, 22], where $n \in \mathbb{N}$ is the fractal iteration number. In the case of 2-state ACA, the only possible prime $p = 2$ and complete fractal structures appear when $k = 2^n$. At steps $k = 32$ and $k = 64$, the structure is a complete fractal at two consecutive iterations $n = 5, 6$ as shown in **Figure 5**.

The fractal iteration number n can be obtained from SAS data as the number of the most pronounced minima in fractal region. Fractal dimension can be better determined from polydisperse scattering structure factor and coincide with theoretical results from **Table 1**. In polydisperse case minima in fractal regions are smoothened due to different distributions of the sizes of basic units; thus, the iteration number and the scaling factor can no longer be determined.

The normalization we used in our calculations is performed in such a way that asymptotes of scattering curves tend to the value $1/N_k$, where N_k is the number of units composing the

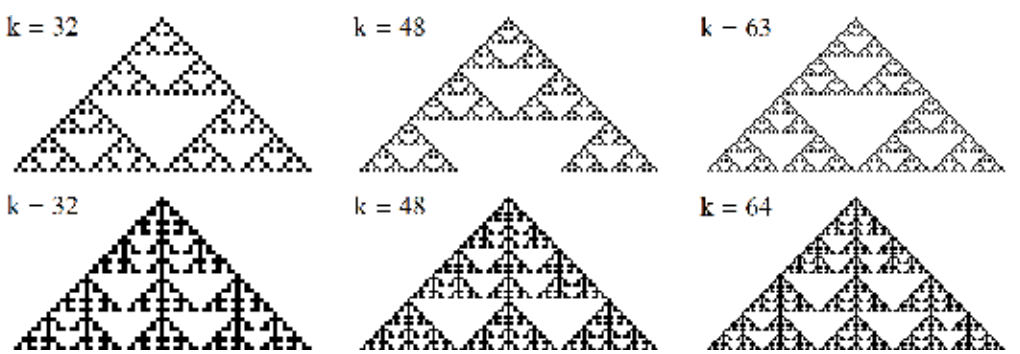

Figure 5. Structure of 2-state ACA at steps $k = 32, 48, 64$. Left part: Rule 90; Right part: Rule 150.

fractal; in the case of ACA, it is the number of occupied sites at step k. For 2-state ACA Rule 90 and Rule 150, one can find analytical relations between the number of occupied sites and the fractal iteration number:

$$N_k = \begin{cases} 3^n, & \text{for 2-state Rule 90} \\ F_{n+2} \cdot 2^n, & \text{for 2-state Rule 150} \end{cases}, \tag{16}$$

where $n = \log_2 k$ is the fractal iteration number and F_j is the jth element of the Fibonacci series.

3.2. 4-state ACA

Results of numerical calculations for mono- and polydisperse scattering structure factors of 4-state ACA Rule 90 and Rule 150 with $c_i = 1$ and their subsets of different states are shown in **Figure 6**.

One can see that the scattering curves of both Rule 90 and Rule 150 in the Guinier region do not coincide. This is due to different distributions of sites in total 4-state and subsets of different states. To analyze this difference, we can compare a radius of gyration of these four structures.

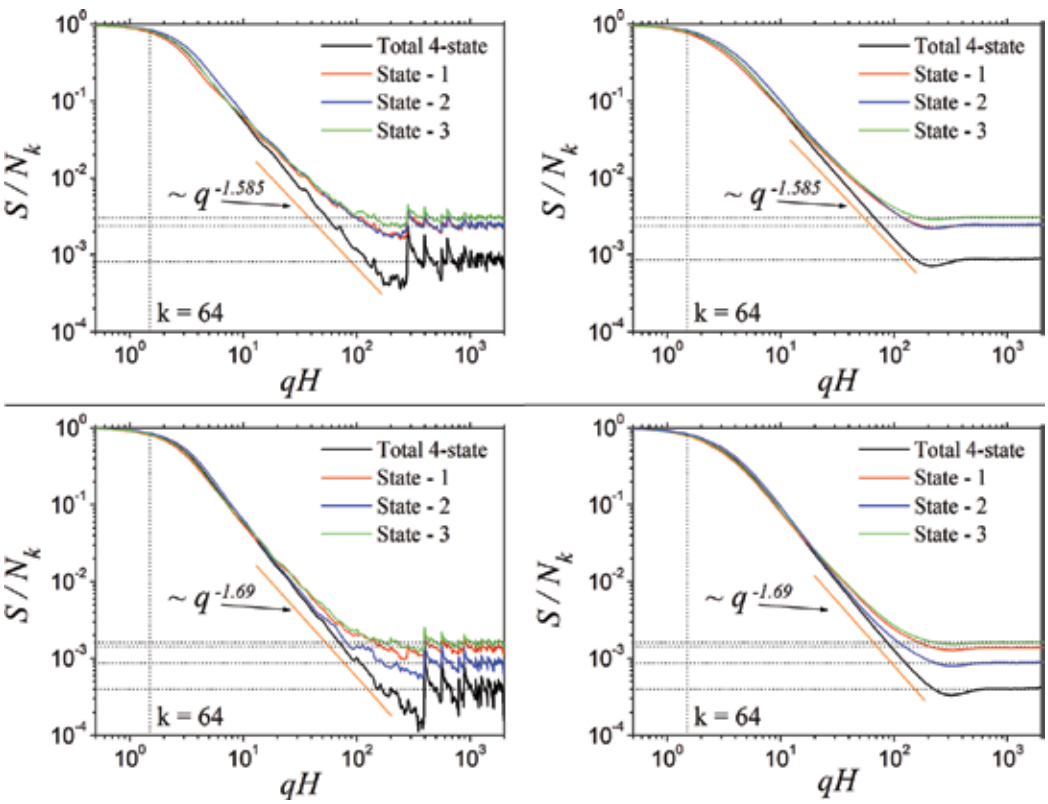

Figure 6. Monodisperse (left part) and polydisperse (right part) structure factors of 4-state ACA. Upper part: Rule 90; lower part: Rule 150.

The radius of gyration R_g of ACA can be obtained from Guinier region by performing a series expansion of the scattering intensity (Eq. (15)):

$$I(q) = I(0)\left(1 - q^2 R_g^2/3 + \cdots\right). \tag{17}$$

Thus, by representing the data from **Figure 6** (left part) in a Guinier plot $\left(\log S \text{vs.}(qH)^2\right)$, the previous expansion gives a linear region of slope, from which the radius of gyration can be obtained through $R_g = \sqrt{3|slope|}$.

Numerical values for the slopes of scattering data for 4-state Rule 90 and Rule 150 for the corresponding state-i, $i = 1, 2, 3$, are shown in **Figure 7**. For both rules one can see that state-1 has the biggest radius of gyration. As shown in **Figure 2**, this can be explained by the fact that in state-1 a higher density of sites is found at the edges of ACA, for state-2 regions of higher density are spread inside, and for state-3 and total 4-state, there are little differences between regions of different densities.

Nonuniform distribution of sites of the subsets is the reason of their multi-fractal properties. To proof this fact, we provide a multi-fractal analysis using barycentric fixed-mass method according to Eq. (9) to the subset states of total 4-state ACA Rule 90 and Rule 150. **Figure 8** shows the dimension spectra of the subsets, and the value D_s is changing along s range, meaning that they are multi-fractals. By definition of generalized dimensions, $s = 0$ gives the box-counting dimension, which is obtained from SAS simulations.

SAS spectra from **Figure 6** show that the fractal dimension of the subsets of different states does not coincide with the fractal dimension of total 4-state. In fact, that occurs due to inappropriate choice of the decomposition, presented in **Figure 2**. From **Table 1** we know that 2-state and 4-state ACA have the same value of fractal dimension; thus, it is expected to have one structure being the part of other. In fact, such pattern appears when state-1 and state-3 of total 4-state ACA are superimposed and form 2-state ACA, as shown in **Figure 9**. 2-State ACA has a bigger value of the fractal dimension than state-2; thus, it equals to the fractal dimension of the total 4-state.

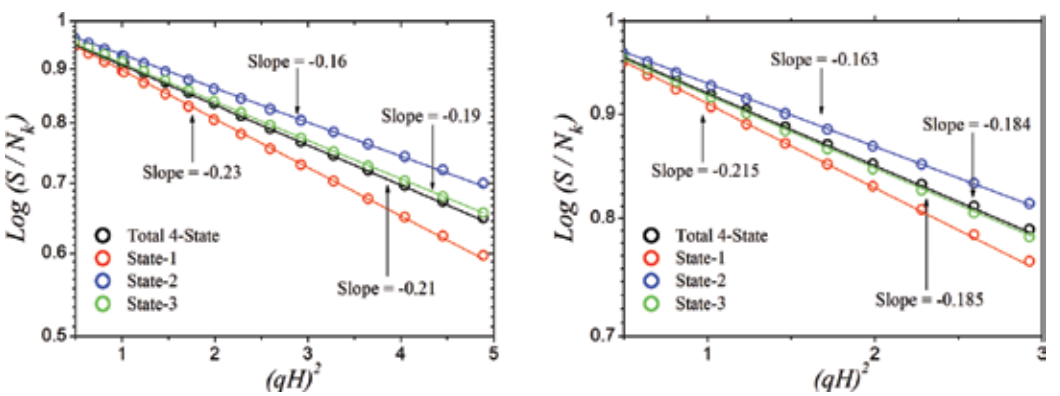

Figure 7. Guinier plot of 4-state ACA. Left part: Rule 90; right part: Rule 150.

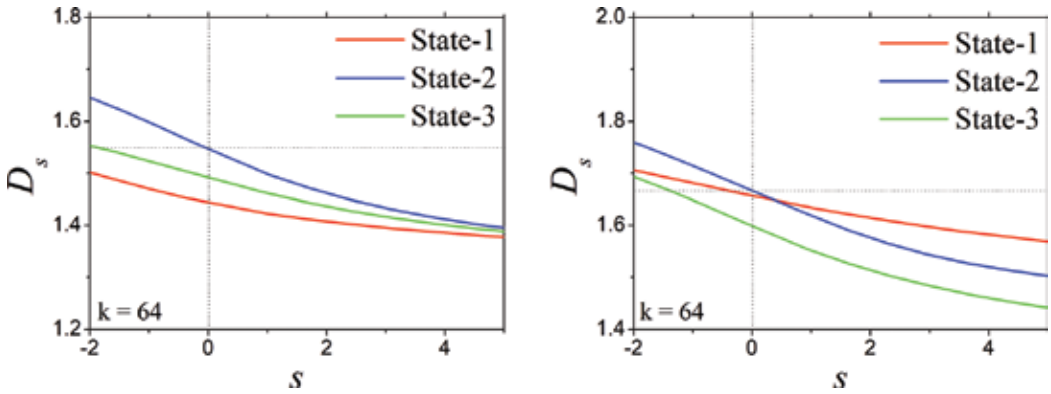

Figure 8. Multi-fractal spectra of the subsets of 4-state ACA. Left part: Rule 90; right part: Rule 150.

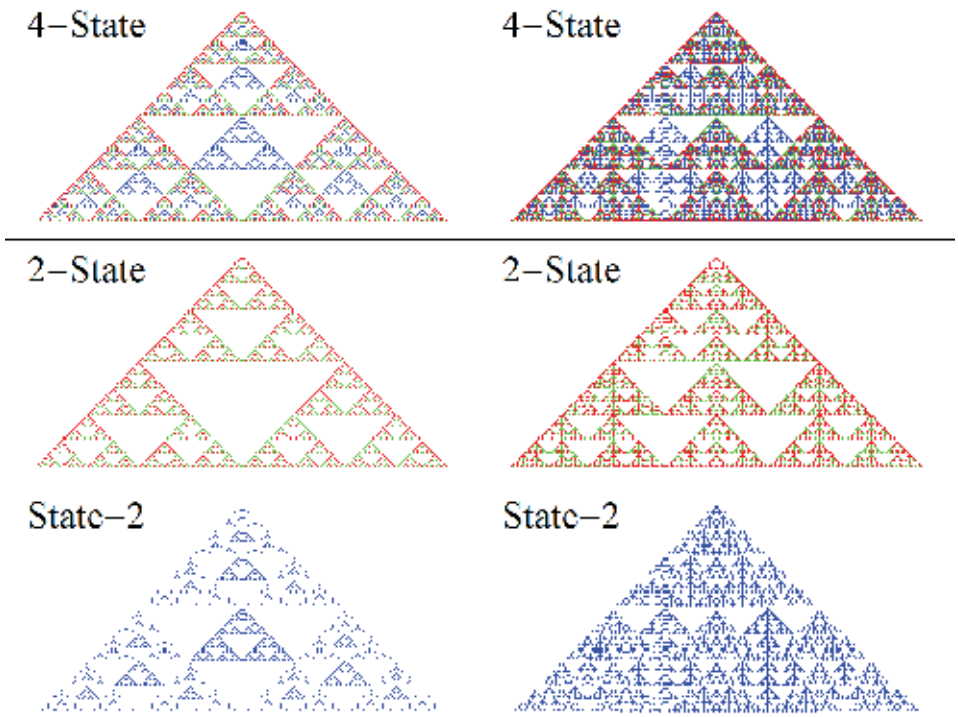

Figure 9. Decomposition of 4-state ACA into 2-state ACA and subset state-2. Left part: Rule 90; right part: Rule 150.

3.3. ACA with different coefficients in transition rule

In previous sections we dealt only with ACA transition rules where all coefficients $c_i = 1$. More general cases of ACA may be obtained varying these coefficients. For an M-state ACA, there are M^i different distinct combinations of c_i exist, where i is the number of terms in transition rule (neighborhood). Most of these combinations generate structures that are trivial and/or are

mirror reflection of each other. However, some of them give quite intricate patterns with the same overall structure as if $c_i = 1$ but with different arrangements of the subsets, presented in **Figure 10**.

In the case of 4-state ACA, we set $c_i = 3$ and calculated corresponding SAS and multi-fractal spectra. Unlike the arrangement presented in **Figure 2**, in this case subsets state-1 and state-3 have more uniform and similar arrangement of the sites. From SAS data (**Figure 11**, left part), one can find that scattering curves of state-1 and state-3 almost completely overlap. The difference appears only in transition between fractal and asymptotic regions. The dimension spectrum (**Figure 11**, right part) shows that there is a little difference in the fractal dimensions of state-1 and state-2, and due to uniform distribution of the sites, the spectra are almost constant along s range, meaning that state-1 and state-2 are mono-fractals. The arrangement of the sites of state-2 is the same as in **Figure 2**, meaning that superposition of

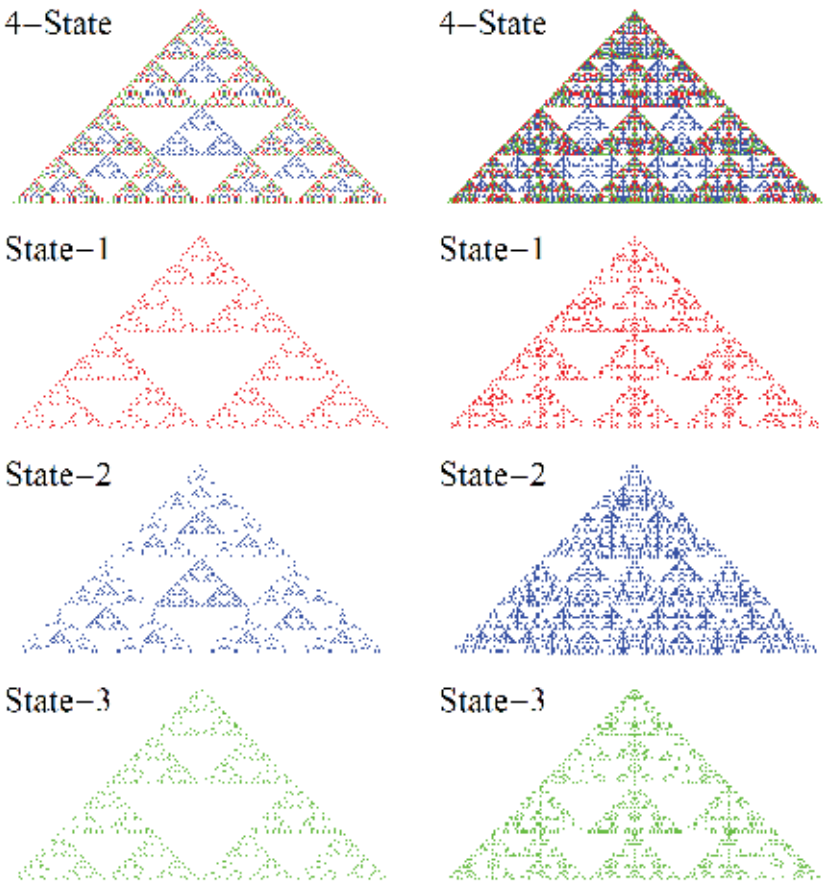

Figure 10. Decomposition of 4-state ACA with $c_i = 3$ into subsets of state-1, state-2, and state-3. Left part: Rule 90; right part: Rule 150.

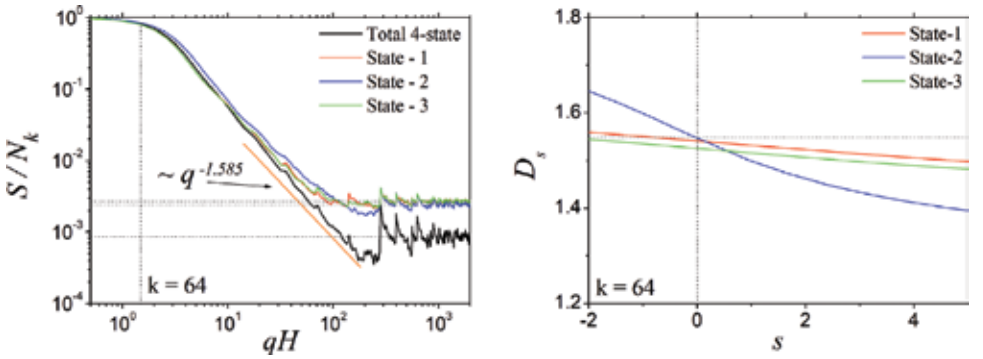

Figure 11. (Left part) Monodisperse structure factor of 4-state ACA Rule 90 with $c_i = 3$. (Right part) Dimension spectra of subset states of 4-state ACA Rule 90 with $c_i = 3$.

the state-1 and state-2 gives the 2-state ACA. It is confirmed by the slope of the scattering curve in fractal region.

For large values of k, Eq. (7) can be approximated by

$$k = N_k^{-D}. \tag{18}$$

Thus, using the value of the fractal dimension obtained from SAS data (**Figure 4**) and the asymptotic values, we can find a good approximation of the number of rows k generated by ACA. Using Eq. (18) one can find connection between the number of rows generated by ACA, the fractal iteration number, and the scaling factor of the corresponding fractal structure:

$$k = \beta_s^{-n}. \tag{19}$$

For self-similar fractals, the total number of scattering units at nth iteration is given by [26]

$$N_n = \left(1/\beta_s\right)^{nD}. \tag{20}$$

From Eqs. (8) and (7), one can find that $N_k = p^{n \cdot D}$. The last expression shows that Eq. (20) can be extended for fractals generated by $M = p^t$-state cellular automata. Thus, the scaling factor of such fractals is the inverse of this prime p:

$$\beta_s = p^{-1}. \tag{21}$$

4. Conclusions

In this chapter we investigated the structural properties of the fractals generated by additive cellular automata. The small-angle scattering technique and multi-fractal analysis are considered to characterize the structure of the nano- and microscale models of ACA fractals. We

present the theoretical foundations of the methods of ACA characterization, such as the transition matrix method, the small-angle scattering, and the multi-fractal analysis. We show how they can be implemented in the structural investigations of the fractals generated by ACA. The analysis is performed using an efficient and optimized version of Pantos and barycentric fixed-mass method for calculating the small-angle scattering and the dimension spectra, respectively.

The mathematical description of the general algorithm for the construction of the fractals using additive cellular automata (ACA) is explained. We show how to obtain the well-known Rule 90 and Rule 150 that generate self-similar fractals using deterministic algorithm. We explain how to construct generalization of these rules for arbitrary M state. The comparison of the structural characteristics of the 2-state and 4-state ACA is presented. We showed cases when subsets of different states of 4-state ACA are mono- and multi-fractals.

For each introduced M-state ACA, we calculate the scattering and the multi-fractal spectrum, and we explain how to extract the main fractal and structural properties such as the fractal dimension, the number of steps generated by ACA, the fractal iteration number, the scaling factor, the overall size, the sizes of the basic units, and the number of units in the system.

The obtained results can be applied for structural investigations of the nano-/microscale systems, modeled by cellular automata.

Author details

Azat Mukhiddinuly Slyamov[1,2] and Eugen Mircea Anitas[1,3]*

*Address all correspondence to: eanitasro@yahoo.com

1 Joint Institute for Nuclear Research, Dubna, Russian Federation

2 Institute of Nuclear Physics, Almaty, Kazakhstan

3 Horia Hulubei National Institute of Physics and Nuclear Engineering, Bucharest-Magurele, Romania

References

[1] Gouyet J-F, Mandelbrot B. Physics and Fractal Structures. Paris: Masson; 1996

[2] Mandelbrot BB, Pignoni R. The Fractal Geometry of Nature. Vol. 173. New York: WH freeman; 1983

[3] Falconer K. Fractal Geometry: Mathematical Foundations and Applications. Chichester, England: Wiley; 2004

[4] Teixeira J. Small-angle scattering by fractal systems. Journal of Applied Crystallography. 1988;**21**(6):781-785. DOI: 10.1107/S0021889888000263

[5] Feigin LA, Svergun DI. Structure Analysis by Small-Angle X-Ray and Neutron Scattering. New York: Plenum Press; 1987

[6] Franke D, Petoukhov MV, Konarev PV, Panjkovich A, Tuukkanen A, Mertens HDT, Kikhney AG, Hajizadeh NR, Franklin JM, Jeffries CM, Svergun DI. ATSAS 2.8: A comprehensive data analysis suite for small-angle scattering from macromolecular solutions. Journal of Applied Crystallography. 2017;**50**:1. DOI: 10.1107/S1600576717007786

[7] Martin JE. Scattering exponents for polydisperse surface and mass fractals. Journal of Applied Crystallography. 1988;**19**(1):25-27. DOI: 10.1107/S0021889886090052

[8] Bale HD, Schmidt PW. Small-angle X-ray-scattering investigation of submicroscopic porosity with fractal properties. Physical Review Letters. 1984;**53**:596

[9] Cherny AY, Anitas EM, Osipov VA, Kuklin AI. Scattering from surface fractals in terms of composing mass fractals. Journal of Applied Crystallography. 2017;**50**:919. DOI: 10.1107/S1600576717005696

[10] Cherny AY, Anitas EM, Osipov VA, Kuklin AI. Small-angle scattering from the cantor surface fractal on the plane and the Koch snowflake. Physical Chemistry Chemical Physics. 2017;**19**:2261-2268

[11] Anitas EM. Small-angle scattering from fat fractals. European Physical Journal B. 2014;**87**:139

[12] Anitas EM, Slyamov A, Todoran R, Szakacs Z. Small-Angle scattering from nanoscale fat fractals. Nanoscale Research Letters. 2017;**12**:389. DOI: 10.1186/s11671-017-2147-0

[13] Anitas EM, Slyamov A. Structural characterization of chaos game fractals using small-angle scattering analysis. PLoS One. 2017;**12**(7):e0181385

[14] Barnsley MF. Fractals Everywhere. London: Academic Press; 2014

[15] Wolfram S. Statistical mechanics of cellular automata. Reviews of Modern Physics. 1983; **55**:601. DOI: 10.1103/RevModPhys.55.601

[16] Wolfram S. Universality and complexity in cellular automata. Physica D: Nonlinear Phenomena. 1984;**10**:1. DOI: 10.1016/0167-2789(84)90245-8

[17] Wolfram S. A New Kind of Science. USA: Wolfram Media; 2002

[18] Wilson SJ. Computing fractal dimensions for additive cellular automata. Physica D: Nonlinear Phenomena. 1987;**24**:190. DOI: 10.1016/0167-2789(87)90074-1

[19] Wilson SJ. The equality of fractional dimensions for certain cellular automata. Physica D: Nonlinear Phenomena. 1987;**24**:179-189

[20] Debye P. Zerstreuung von röntgenstrahlen. Annalen der Physik. 1915;**351**(6):809-823

[21] Pantos E, van Garderen HF, Hilbers PAJ, Beelen TPM, van Santen RA. Simulation of small-angle scattering from large assemblies of multi-type scatterer particles. Journal of Molecular Structure. 1996;**383**:303-308

[22] Takahashi S. Self-similarity of linear cellular automata. Journal of Computer and System Sciences. 1992;**44**:114. DOI: 10.1016/0022-0000(92)90007-6

[23] Hausdorff F. Dimension und äußeres Maß. Matematische Annalen. 1918;**79**:157

[24] Vicsek T. Fractal Growth Phenomena. Singapore: World Scientific Pub Co Inc; 1992

[25] Kamer Y, Ouillon G, Sornette D. Barycentric fixed-mass method for multifractal analysis. Physical Review E. 2013;**88**:022922. DOI: 10.1103/PhysRevE.88.022922

[26] Cherny AY, Anitas EM, Osipov VA, Kuklin AI. Small-angle scattering from multiphase fractals. Journal of Applied Crystallography. 2014;**47**:198-206. DOI: 10.1107/S1600576713029956

Edited by Margareth K. K. D. Franco and Fabiano Yokaichiya

Reasoned and based on the difference between discovery and invention, according to the traditional conception, science can be distinguished between basic science and applied science. Nevertheless, we know that the sciences are inseparable. A century or more ago, Louis Pasteur said "there is no applied science, there are applications of science." With this assertion, he establishes the logic of complementarity between them. Science certainly goes beyond its own material application and brings us to issues that have intrigued humanity for a long time. During the many years that we have been working with techniques of material characterization, we observed that this complementarity was not always understood by the researchers. In line with the reasoning that the technique joined with science generates technology, the application of techniques that use x-ray and neutron sources seems to us of fundamental importance for the development of technology. In this way, we present in this book how the existing technology of material characterization can contribute to science and applied technology. The authors who contributed with this book sought to show the importance of applying the existing techniques in the development of their works.

Published in London, UK

IntechOpen

ISBN 978-1-83881-581-3
9 781838 815813